Position Sensorless Control of a Transverse-Laminated Reluctance Synchronous Machine

by

Francois Jacobus Wessels Barnard

Thesis presented in partial fulfilment of the requirements for the degree Master of Science in Electrical and Electronic Engineering at Stellenbosch University

Department of Electrical and Electronic Engineering,
Stellenbosch University,
Matieland, South Africa.

Supervisor: Prof. Maarten J. Kamper

December 2014

Declaration

By submitting this thesis electronically, I declare that the entirety of the work contained therein is my own, original work, that I am the sole author thereof (save to the extent explicitly otherwise stated), that reproduction and publication thereof by Stellenbosch University will not infringe any third party rights and that I have not previously in its entirety or in part submitted it for obtaining any qualification.

Signed: F.J.W. Barnard

Date: September 2014

Abstract

Position Sensorless Control of a Transverse-Laminated Reluctance Synchronous Machine

The focus of this thesis is position sensorless control of a transverse-laminated reluctance synchronous machine. Rotor position information is required for high-performance closed-loop control of the reluctance synchronous machine and is conventionally supplied by unreliable hardware position resolvers. In addition a FPGA-based rapid prototyping system is completed as part of the research term for control of the machine drive system.

For the first time the unified active-flux (AF) method is investigated and implemented for position sensorless control of the transverse-laminated reluctance synchronous machine in this study. The method is based on the torque equation of the machine and is basically the same for any AC machine. The estimation scheme is implemented for closed-loop position sensorless control from low- to rated speed in the entire rated load range with simulation and measured results confirming its capabilities. A number of characteristics of the machine (including generator operation) have implications for implementation of the active-flux (AF) method and are therefore investigated.

Another position estimation method investigated is the arbitrary injection (AI) scheme which is derived to be completely machine parameter independent. The method simply requires a current progression at each calculation step allowing use of a smaller injection voltage. This method is implemented again on the reluctance synchronous machine and is shown to be capable of position sensorless current and speed control of the drive from standstill to rated speed with simulation and measured results. However, when the machine is operating above low speeds it is shown that this technique is only capable of position sensorless control at low loads.

To deliver position sensorless control in the entire rated speed and load range a new hybrid controller scheme is designed and implemented. The hybrid scheme is speed and load dependent with hysteresis regions for stability at specific working points. The active-flux (AF) method is implemented in the low to rated speed range at medium to rated loads while the arbitrary injection (AI) method is implemented elsewhere. Measured results show that the scheme is capable of position sensorless control in the entire rated speed and load range with some limitations on dynamics.

Because of the limitations on dynamics of the hybrid scheme an assisted fundamental model position estimation scheme was investigated. Simulation results show that this controller requires further investigation.

Opsomming

Posisie Sensorlose Beheer van ‘n Transvers-Gelamineerde Reluktansie Sinchroonmasjien

Die fokus in hierdie tesis is die posisie-sensorlose beheer van ’n transvers-gelamineerde reluktansie sinchroonmasjien. Rotor posisie inligting word benodig vir geslote-lus beheer van die reluktansie sinchroonmasjien met hoë-werkverrigting, en word normaalweg deur onbetroubare hardeware sensors verskaf. As deel van die navorsings-termyn is ’n FPGA-gebaseerde beheerstelsel vir die masjien stelsel voltooi.

Die “aktiewe-vloed” posisie-afskattings metode is ondersoek en vir die eerste keer geïmplementeer vir posisie-sensorlose beheer van die transvers-gelamineerde reluktansie sinchroonmasjien. Die metode is dieselfde in konsep vir alle WS masjiene en word basseer op die vergelyking vir wringkrag van die masjien. Vollas geslote-lus posisie-sensorlose beheer van die masjien in die lae tot hoë spoedbereik is suksesvol geïmplementeer met simulasie en gemete resultate. Verkskeie inherente eienskappe van die masjien het implikasies vir gebruik van die “aktiewe-vloed” metode (insluitend generator werking) en is dus ondersoek.

Die “arbitrêre injeksie” metode wat afgelei is om onafhanklik van masjien parameters te wees is ook odersoek. Hierdie metode verlang slegs ’n stroom-afgeleide by elke tydstip en benodig dus ’n kleiner injeksie-spanning. Hierdie metode is weer geïmplementeer op die reluktansie sinchroon masjien met suksesvolle posisie-sensorlose beheer in die hele spoed bereik getoon in simulasie en praktiese resultate. Dit word egter getoon dat hierdie metode slegs onder lae-las toestande posisie sensorlose beheer bo lae-spoed kan bewerkstellig.

Ten einde posisie-sensorlose beheer in die hele spoed en wringkrag bereik te verkry is ’n nuwe hibriede beheerskema ontwerp en geïmplementeer. Die skema is spoed en las afhanklik met histerese vir stabiliteit by ’n spesifieke werkpunt. Die “aktiewe-vloed” metode word gebruik bo lae spoed teen ’n minimum las terwyl die “arbitrêre injeksie” andersins geïmplementeer word. Gemete resultate toon dat die skema posisie-sensorlose beheer van die masjien in die hele spoed en las bereik toelaat met sommige beperkings op dinamika.

Met inagneming van die beperkings op die hibriede metode is ’n ondersteunde fundamentele model afskattingskema ondersoek. Simulasie resulate toon dat hierdie beheerder verdere ondersoek benodig.

Acknowledgements

I would like to give thanks to the following people for their contribution to making this project a success:

- My supervisor Prof. Maarten Kamper for his suggestions, support and motivation throughout the last two years.
- Dr. Wikus Villet for giving me the idea of pursuing these postgraduate studies in the first place and for his immeasurable amount of help and guidance during the first year of this project. Without him, this project would definitely not have been possible.
- Dr. Peter Stolze from the Technical University of Munich in Germany for all of his time giving suggestions and support via email conversations for getting the Pentium System running during the finishing stages of his PhD and the arrival of his first child.
- Mr. Tino Müller from Germany for his technical support getting the Pentium System running.
- Prof. Ion Boldea from Romania for his suggestions regarding the implementation of his active flux concept.
- Mr. JP du Plooy for his flux-mapping script.
- The National Research Foundation (NRF) for their financial support.[1]
- My family and friends for their continuous support during the past two years.
- My father Hendrik Barnard for his love, motivation, and interest in my work.
- Janke Den Heijer, my darling, my love, my best friend.
- And above all, my Lord God, for being the ultimate source of hope and spiritual guidance during my 6 years of engineering studies.

[1]The financial assistance of the National Research Foundation (NRF) towards this research is hereby acknowledged. Opinions expressed and conclusions arrived at, are those of the author and are not necessarily to be attributed to the NRF.

Publications

A part of my research work on position sensorless control of reluctance synchronous machines was presented at an international conference (SPEEDAM 2014 in Ischia, Italy) and published. The paper is titled:

- F. J. Barnard, W. T. Villet, and M. J. Kamper, "Hybrid active-flux and arbitrary injection position sensorless control of reluctance synchronous machines," in 2014 International Symposium on Power Electronics, Electrical Drives, Automation and Motion (SPEEDAM), June 2014, pp. 1146-1151.

The paper was selected by the SPEEDAM 2014 Program Committee as one of the best of those presented and deemed eligible for review for publication in the IEEE Transactions on Industry Applications journal. This review process is currently under way.

Contents

List of Figures

List of Tables

Nomenclature

Variables

v	Voltage	[V]
i	Current	[A]
ψ	Flux-Linkage	[Wb − turns]
R	Resistance	[Ω]
L	Linearised Inductance	[H]
$\tilde{L}$	Tangential Inductance	[H]
M	Mutual Inductance	[H]
θ	Rotor angle	[rad]
ω	Angular velocity	[rad/s]
n	Rotational speed	[r/min]
τ	Torque	[Nm]
B_{eq}	Equivalent friction coefficient	[Nm.s/rad]
J_{eq}	Equivalent moment of inertia	[kg.m^2]
t	Time	[s]
T	Sampling Period	[s]
γ	Current angle	[deg]
p	Pole pairs	

Abbreviations

AC	Alternating Current
ADC	Analog-to-Digital Converter
AF	Active-Flux
AFM	Assisted Fundamental Model
AI	Arbitrary Injection
ALA	Axially-Laminated Anisotropic
CCAC	Constant Current Angle Control
CFCC	Constant Field Current Control
CPLD	Complex Programmable Logic Device
DAC	Digital-to-Analog Converter
DC	Direct Current
EM	Electrical Machine

FE	Finite Element
FOC	Field Oriented Control
FPGA	Field Programmable Gate Array
FS	Fundamental Saliency
HFI	High-Frequency Injection
HPF	High-Pass Filter
IM	Induction Machine
ISA	Industry Standard Architecture
LUT	Look-Up Table
MMF	MagnetoMotive Force
MTPA	Maximum Torque Per Ampere
PI	Proportional Integral
PLL	Phase-Locked Loop
PMA	Permanent Magnet Assisted
PMSM	Permanent Magnet Synchronous Machine
PSC	Position Sensorless Control
RPS	Rapid Prototyping System
RSM	Reluctance Synchronous Machine
RTAI	Real Time Application Interface
SVPWM	Space Vector Pulse Width Modulation
TF	Transfer Function
TL	Transverse-Laminated
VA	Volt-Amperes
VSI	Voltage Source Inverter
VVC	Vector Voltage Control
ZOH	Zero-Order Hold

Sub- and superscripts

d, q	Direct and quadrature axis (rotor fixed reference frame)
α, β	Alpha and beta axis (stator fixed reference frame)
a, b, c	Stator phase axis
s	Stator fixed reference frame (stationary)
r	Rotor fixed reference frame (synchronously rotating)
e	Electrical
m	Mechanical

Chapter 1

Introduction

Electrical machines (EM) is a mature field of research with multiple applications in various industries. With the focus on humanity's environmental impact in recent years - especially as a result of the use of electricity - EMs have received renewed interest due to the search for renewable energy sources and lower energy usage.

The reference AC machine for industrial motor applications requiring constant-torque is the induction machine (IM). The IM has a simple to construct rotor and requires only AC supply on its stator, resulting in a cost effective solution. Flux-weakening can be usefully implemented on IMs, reducing kVA requirements from the inverter at extended speeds. It is also possible to use the IM for generator applications, but it has various disadvantages when operated in this mode and is consequently rarely implemented as such [1]. Constant-torque applications see surface-mounted permanent magnet synchronous machines (PMSM) as the regular solution, because they provide high torque-per-volume. Unfortunately these solutions are expensive, because of the use of rare-earth magnets. Subsequently, the search for higher efficiency permanent magnet-less motor drive systems has led to considerable attention being paid to the reluctance synchronous machine (RSM) [2].

1.1 The Reluctance Synchronous Machine

The concept of reluctance synchronous machines is very old as introduced in [3], but it has not been adopted in industry on a large scale, because of low performance under open-loop control. With the decrease in cost of digital solutions in recent times, closed loop control of machines has become a viable solution for large scale implementation. This has paved the way for the RSM, since it has been shown by [4] - [7] to be more efficient and to be capable of producing much higher torque for the same frame size (torque-per-volume) than the IM under closed loop control. Commercially RSM motors are known as the synchronous reluctance motor (SynRM) and lately companies such as ABB® offer these motors as very high efficiency alternatives for variable speed applications.

The RSM has a standard 3-phase slotted stator with spatially separated sinusoidal excitation. The rotor requires only magnetically conductive material, eliminating the costs of electrically conductive materials such as aluminium and copper. Since it does not use magnets the RSM also has significantly lower costs than PMSMs and can be used as a more cost-effective solution for servo drive applications, even though the latter may have higher torque-per-volume characteristics [4]. RSM rotors are magnetically asymmetrical (anisotropic) so that torque can be produced by the reluctance effect. The transverse-

laminated (TL) RSM has a simple rotor structure, typically using only magnetically insulated steel laminations, making it cost effective to manufacture as well. This results in a very robust machine that is not susceptible to demagnetization or arching.

Additional to the aforementioned points the RSM has the following advantages as pointed out in [8] justifying its attention:

- Field oriented control (FOC) appears to be more simple for RSMs than IMs.
- Synchronous machines have advantages in some applications.
- In contrast with IMs the RSM has no core and copper losses in its rotor, giving it "cold rotor" status with some niche applications.

Practically, RSMs have notable application possibilities in the fields of multi-gear electrical drives [9, 10], high speed geared wind generator systems [11, 12] and, as mentioned, variable speed industrial drives [6].

Efficient control of the RSM requires rotor position information when implementing FOC such as [13]. Conventionally this information is supplied by a hardware sensor attached to the shaft, e.g. rotary encoder. These sensors are typically unreliable (and expensive for low power drives) compared to the motor and inverter system, increasing overall cost and compromising robustness of the RSM drive. To be a completely competitive alternative to IM drives, the RSM drive needs to be cost effective and robust. The motivation for position information estimation is now apparent.

1.2 Position Sensorless Control

The last two decades have seen speed- and position-sensorless (further referred to simply as sensorless) control of AC machines becoming a commercial alternative for IM and PMSM drives. These solutions enable the high performance of closed loop control without dependence on unreliable hardware position sensors. Position estimation schemes for AC machines fall mainly into two fields: fundamental excitation and saliency based/signal injection techniques [14]. Fundamental excitation methods make use of stator voltage and current measurements to determine rotor position information using the characteristic model of the machine. These methods generally work from medium to rated and extended speeds of operation. Saliency based/signal injection methods work for rotors that have an angular-separated difference in inductance, typically exploited by means of an additional signal injection. These methods are capable of rotor tracking from standstill to higher speeds.

Position estimation for RSMs (or applicable to RSMs) is a relatively well studied subject, with multiple methods based on the two fields of position estimation. The fundamental excitation methods investigated include [15]-[20], while [21]-[24] describe saliency based techniques implementing signal injection for position estimation.

In [15] an extended electromotive force (EEMF) model is used for position estimation in the low- to high-speed range with d-axis chosen in the direction of minimum rotor inductance for less vulnerability to inductance changes in the estimation. At standstill a system identification method is used to estimate the initial rotor position and the machine is sped up using a feed-forward method. Results indicate stable sensorless constant speed control under load conditions.

A RSM is implemented for control of a precise moving table (servo drive systems) in [16] using a sensorless position control scheme based on a relatively complex switching

mode model of the machine with a state space velocity estimator. The control scheme implements a constant d-axis current and is shown to be accurate enough for general servo drive industry applications, however only standstill and low speed results are proven. The current control method constitutes lower efficiency and the low speeds are unsuitable for variable speed drive applications.

A novel position sensorless control method for a low-power RSM is presented in [17]. Current zero-cross detection is implemented to realise a very low cost drive system without ADC and precise current measurement requirements. The control scheme operates at maximum torque/ampere in all operating conditions and implements an open loop starting procedure up to medium speed. Therefore, sensorless variable speed control is only achieved above a minimum speed.

A reduced-order position observer with stator-resistance adaptation is proposed in [18] for a salient PMSM and analysed for a RSM in [25]. The scheme is designed to be stable even with errors in parameter estimates and is shown to be capable of sensorless control at low speeds under various load conditions. Position estimation schemes are usually parameter dependent and uncertainties are accounted for in the stability analysis of this scheme. In this paper the derivation of analytical equations for stability conditions and the effect of observer gain magnitude is investigated. This scheme also implements constant d-axis current to enable position estimation.

Introduced in [19] is the generalization concept of active-flux (or torque-producing flux) that turns all salient-pole travelling-field machines into virtual nonsalient-pole representations. The method relies on observing the active-flux aligned with the d-axis of the machine in order to estimate the rotor position. A constant direct axis current is employed to result in constant active-flux - which results in less efficient control. The sensorless control scheme is shown to be stable in a wide speed range, from low to high speed.

A relatively new fundamental saliency based position estimation scheme is presented in [20]. Current control approaches maximum torque per ampere in this scheme for high efficiency and the method is dependent on an accurate isotropic flux lookup table as well as a position estimation error compensation for closed loop control using the estimated rotor angle. The scheme is shown to be stable from low to high speed.

Various high-frequency signal injection (HFI) techniques for saliency-based position estimation of PMSMs which are applicable to RSMs are compared in [21] and [22]. The sensitivity of pulsating- and rotating-vector carrier signal injection-based methods to non-ideal physical machine attributes are investigated in [21], and it is found that both methods are similarly accurate. Continuous- and transient-signal injection methods as well as PWM excitation methods are compared in terms of hardware configuration complexity, torque ripple and acoustic noise, operating speed range, estimation bandwidth, and cost of current measurement system in [22]. It is shown that continuous signal injection methods result in the simplest and most cost effective solution, but have the highest torque ripple and lowest estimation bandwidth.

In [23] a relatively new saliency based sensorless field-oriented control method is proposed for a PMSM. This method is built on the idea of comparing the predicted current progression of an isotropic machine model with that of the measured anisotropic machine current progression to deliver rotor position information. The work is a culmination of that presented in [26] and [27] (among others), where [26] is the application of the initial concept with predictive torque control on a RSM while [27] shows how the method can be made completely parameter independent. Subsequently the method proposed in [23] allows parameter estimation when choosing an injection scheme with equal spacial distri-

bution. The name arbitrary injection results from the fact that no predetermined injection signal shape is required for this position estimation scheme, only a current progression for every estimation step. This method has high torque capabilities at standstill and very low speeds, but at higher speeds the torque capabilities fail.

A simplified HFI position estimation method for RSMs is shown in [24], based on the work presented in [28] for a PMSM at very low speeds and standstill. The method proposes the removal of a common bandpass filter used in the signal processing loop in order to avoid its phase shift and magnitude decrease. It is shown that the method is capable of stable sensorless operation from standstill up to rated speed for the RSM, with some torque limitations at higher speeds.

From these articles it can be seen that no single position estimation technique is sufficiently capable of position sensorless control (PSC) of the RSM in all operating conditions. The fundamental excitation methods are stable, dynamic, and capable at extended load applications, but fail at lower speeds. The signal injection methods are capable of control at full load even at standstill, but have limited load capabilities at higher speeds, because of saliency shift with load. Signal injection techniques use a part of the DC bus supply for the injection voltage and therefore also increase DC bus requirements for higher loads at high speeds.

When considering the strengths and drawbacks of the different estimation fields, it is evident that the combination of these techniques enable full load position sensorless control capabilities in all practical speed regions. Hybrid control schemes of this nature have been presented in [29]-[32].

A hybrid position observer for PM motor drives is presented in [29], implementing a HFI method at low speed while incorporating the HFI-estimate into the flux observer used at higher speeds. The combination strategy provides smooth transition between estimation techniques and sensorless control capabilities from zero to extended speed under any load condition.

In [30] a HFI-assisted active-flux-based position sensorless control scheme for an axially-laminated anisotropic (ALA) RSM is proposed. Both schemes are active in the speed transition region with a smooth filtering to combine the estimated angles. Use of the ALA RSM allows implementation of the HFI method without the presence of q-axis current, since it has inherent magnetic saliency, while constant d-axis current control is implemented for the presence of active flux. The control scheme is theoretically simple and is shown to be fast and dynamic with sensorless control from standstill to rated speed.

High-performance position sensorless control of a TL RSM is shown in [31], implementing d-axis flux- and q-axis current-control. The hybrid scheme combines an EMF-based estimator with a signal injection method resulting in dynamic performance in the whole speed range. Magnetic- and cross-saturation effects are taken into account by implementing a flux-observer, since accurate knowledge of machine magnetic behaviour is required for the sensorless control scheme.

Hybrid position sensorless vector control (FOC) of a TL RSM through the entire rated speed range is presented in [32]. The scheme combines the simplified HFI scheme in [24] and the fundamental saliency method in [20] with a speed hysteresis region to eliminate constant switching between estimation techniques at a working point. Position sensorless current- and speed control is showcased in the entire rated speed range with extended load capabilities.

It should be noted that some of the position estimation schemes listed are for PMSMs or permanent magnet assisted reluctance synchronous machines (PMARSMs), but that

they could possibly be made applicable to RSMs with appropriate control strategies and some alterations.

1.3 Problem Statement

In order for RSM drives to be a practical alternative to current industrial drive solutions the following characteristics need to be achieved:

- High efficiency
- High torque density
- Robust design
- Dynamic performance
- Cost effectiveness

Optimised design of the RSM enable high efficiency and torque density while cost is inherently low. Mechanically the RSM drive system is very robust with the use of appropriate materials and only a physical position sensor would compromise this. Therefore the only remaining problem faced for RSM drive systems is reliable, dynamic and accurate position sensorless control for all load conditions in the entire speed range. In consideration of the specifications for a practical alternative industrial drive, the control schemes derived are aimed at close to optimum efficiency in the entire rated speed and load range.

The transverse-laminated RSM considered for control herein has some distinct advantages compared to an axially-laminated anisotropic (ALA) RSM, but the latter is advantageous for the use of position estimation techniques, because it has inherent inductance saliency without the presence of current. The aim of this research is control of a transverse-laminated RSM, because it has a distinct advantage in ease of manufacturing and poses the greatest potential for large scale commercial implementation as noted by [6]. Therefore, the disadvantage in terms of sensorless control has to be dealt with.

As an application of the RSM to reliable wind generator systems the characteristics listed above are required and attention should be paid to reliable and stable sensorless control in the negative current region (generator action). This has potential implications for position estimation schemes and should therefore be investigated.

1.4 Approach to Problem

As the main topic of this thesis is sensorless control of RSMs, a mathematical and FE model of the reluctance synchronous machine is investigated. Control techniques are then studied and simulated using a computer model of the RSM. What follows thereafter is investigation into position estimation and sensorless control techniques for RSMs.

Previous research on position sensorless control of the RSM at the Stellenbosch University Electrical Machines lab was done by Wikus Villet in his Masters and PhD [33] theses, implementing the alternating high-frequency injection method in [24], the fundamental saliency method in [20] and in his PhD the arbitrary injection method proposed in [23]. In order to investigate the suitability of other position sensorless control techniques

with possible advantages, the following position estimation methods were investigated and implemented.

The unified PSC active-flux method proposed by Ion Boldea in [19] is implemented as an alternative fundamental model estimation technique, because it possibly has better low speed performance and mainly the same structure for any AC machine. Furthermore, it proved to have a very simple theoretical derivation. Estimation using this method is simulated using a Matlab® Simulink® model whereafter it is implemented practically on a transverse-laminated RSM in the lab.

For zero- to low-speed estimation the arbitrary injection method is also implemented. This method has higher torque capabilities in the very low speed region than when compared to other saliency based signal injection methods, because it does not rely on a specific injected voltage shape but only requires the presence of a current derivative term. Furthermore, this method is expanded in [27] to be completely independent of initial knowledge of machine parameters and can be adapted to be applicable to any synchronous machine. This method is also simulated using a Matlab Simulink model and implemented practically.

A hybrid position sensorless controller is then designed to combine the active flux and arbitrary injection methods in the entire rated speed range. This novel scheme is implemented practically with standstill to rated-speed tests in the entire rated load-range. With some adaptation the combination of these two techniques could result in a unified position sensorless control technique for any synchronous machine.

Because of the drawbacks and limitations encountered with the preceding hybrid method an assisted fundamental model scheme is investigated in order to maintain fundamental model control in the entire rated speed range. This is done by implementing the fundamental saliency based method proposed by Peter Landsmann et al. in [20].

Before the practical tests, a FPGA-based rapid prototyping system (RPS) was set-up to run the control algorithm, supply switching signals to the inverter, and display control outputs and measurements. This system runs a Linux real time application interface (RTAI) based operating system and was developed by among others Peter Stolze of the Technical University of Munich, Germany. The set-up included hardware fault debugging, programmable logic device firmware coding, system layout design and some circuit design.

1.5 Thesis Layout

The layout of the remaining part of the thesis is as follows:

Chapter 2: A mathematical model for the RSM is derived in terms of stator voltage equations in order to allow design of controllers for the machine. This is followed by modelling of the mechanical system and an analysis of the machine parameters. Finally the Matlab® Simulink® models used before practical implementation of the controllers are described.

Chapter 3: The drive system and some practical implications are described followed by design and validation of the current and speed controllers. This includes simulation and measured results of the controllers.

Chapter 4: The active-flux position estimation method is described including simulation and practical results. This includes practical implications for implementation of the AF method on a TL RSM.

Chapter 5: The arbitrary injection position estimation method is described including simulation and measured results. This includes a parameter estimation section that allows the scheme to be completely parameter independent. Also, some practical implications for implementation of the method on a TL RSM are described.

Chapter 6: The designed hybrid position sensorless controller scheme combining the AF and AI methods is described with measured results.

Chapter 7: A different hybrid position sensorless control scheme is investigated considering the results found in chapter 6. This includes simulation results.

Chapter 8: Conclusions are drawn regarding the research contained in this thesis followed by some recommendations by the author.

Chapter 2

Mathematical Model of the RSM

In this chapter the RSM is described mathematically using electrical equations. These equations describe the electrical and mechanical behaviour of the RSM and are manipulated in later chapters to derive transfer functions for control of the machine and to enable rotor position estimation. Quantities are described by their vector representations in certain space reference frames which are described and explained in Appendix A. Secondly, the simulated and measured machine parameters are described and derived. The final section describes the simulation model used to design the machine controllers and analyse electrical and mechanical behaviour characteristics.

In this and following chapters quantities in lower-case bold-font represent vectors (i.e. $\boldsymbol{v}$), upper-case bold-font represent matrices or tensors (i.e. $\mathbf{T}$), hatted quantities represent estimated values (i.e. $\hat{\theta}$), and error quantities (i.e. $\tilde{\theta}$) are indicated with a tilde (except for the tangential inductance $\tilde{L}$). The dummy notations x and y represent orthogonal axes in a reference frame. Subscripts describe the location of the physical quantity and superscripts the used reference frame.

2.1 Electrical Circuit Model

The stator voltage equation for a three-phase RSM is equal to [2]

$$\boldsymbol{v}_{abc} = R_s \boldsymbol{i}_{abc} + \frac{d}{dt}\boldsymbol{\psi}_{abc} \tag{2.1.1}$$

with

$$\boldsymbol{x}_{abc} = \begin{bmatrix} x_a & x_b & x_c \end{bmatrix}^T.$$

By applying the Clarke transformation the stator voltage equation in stator reference frame (see Appendix A) is equal to

$$\boldsymbol{v}_s^s = R_s \boldsymbol{i}_s^s + \frac{d}{dt}\boldsymbol{\psi}_s^s \tag{2.1.2}$$

where

$$\boldsymbol{x}_s^s = x_\alpha + j x_\beta.$$

By defining the q-axis to be leading the d-axis by 90° and aligning the d-axis on the rotor axis with the lowest reluctance path the stator voltage can be transformed to the $dq0$ reference frame (rotor reference frame) to result in [34]

$$\boldsymbol{v}_s^r = \mathbf{K}_r \boldsymbol{v}_{abc} \tag{2.1.3}$$
$$= \mathbf{T}^{-1} \boldsymbol{v}_s^s \tag{2.1.4}$$

where

$$\begin{aligned} \boldsymbol{x}_s^r &= x_d + j x_q \\ \mathbf{T} &= \begin{bmatrix} \cos\theta_e & -\sin\theta_e \\ \sin\theta_e & \cos\theta_e \end{bmatrix} \\ \mathbf{T}^{-1} &= \mathbf{T}^T. \end{aligned} \tag{2.1.5}$$

so that

$$v_d = R_s i_d + \frac{d}{dt}\psi_d - \omega_e \psi_q \tag{2.1.6}$$
$$v_q = R_s i_q + \frac{d}{dt}\psi_q + \omega_e \psi_d \tag{2.1.7}$$
$$v_0 = R_s i_0 + \frac{d}{dt}\psi_0. \tag{2.1.8}$$

When considering a balanced three phase system the zero sequence voltage v_0 falls away so that the combination of (2.1.6) and (2.1.7) equals

$$\boldsymbol{v}_s^r = R_s \boldsymbol{i}_s^r + \frac{d}{dt}\boldsymbol{\psi}_s^r + j\omega_e \boldsymbol{\psi}_s^r. \tag{2.1.9}$$

The reference frames aligned on a simple two pole ($p = 1$) RSM is displayed in Figure 2.1. The axis labelled a is the magnetic a-axis which would be produced by a positive current flowing into the conductor a and out of $-a$ of the a-phase winding. θ_e is the angular separation between axes a and d which is defined as the electrical rotor angle, evident from the figure. Therefore, for a synchronous machine, the d-axis rotates with the induced stator flux vector at synchronous speed ω_e.

The flux linkage-time derivative terms $\frac{d}{dt}\psi$ in (2.1.6) and (2.1.7) is expanded in the following section. Flux linkage is a function of current and rotor angle, defined as

$$\psi_d = f(i_d, i_q, \theta_e), \tag{2.1.10}$$
$$\psi_q = f(i_q, i_d, \theta_e). \tag{2.1.11}$$

Therefore, the time derivative of the flux linkages can be expressed as

$$\frac{d}{dt}\psi_d = \frac{\partial \psi_d}{\partial i_d}\frac{di_d}{dt} + \frac{\partial \psi_d}{\partial i_q}\frac{di_q}{dt} + \frac{\partial \psi_d}{\partial \theta_e}\frac{d\theta_e}{dt}, \tag{2.1.12}$$
$$\frac{d}{dt}\psi_q = \frac{\partial \psi_q}{\partial i_q}\frac{di_q}{dt} + \frac{\partial \psi_q}{\partial i_d}\frac{di_d}{dt} + \frac{\partial \psi_q}{\partial \theta_e}\frac{d\theta_e}{dt}. \tag{2.1.13}$$

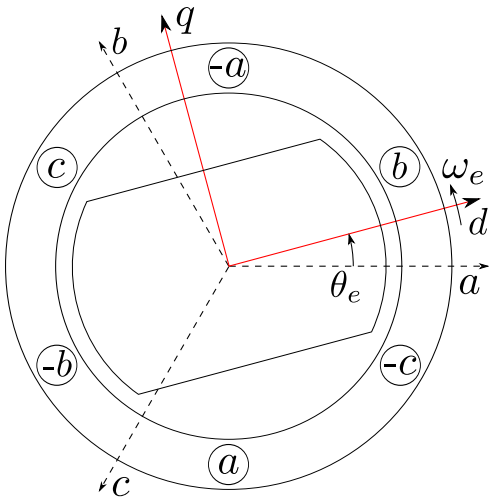

Figure 2.1: The $dq0$ and abc reference frames aligned on a two pole RSM.

Defining $\tilde{L}_x = \frac{\partial \psi_x}{\partial i_x}$ as tangential inductance as in [35], $M_x = \frac{\partial \psi_x}{\partial i_y}$ as mutual inductance and $\omega_e = \frac{d\theta_e}{dt}$ as electrical angular rotor velocity the following results

$$\frac{d}{dt}\psi_d = \tilde{L}_d \frac{di_d}{dt} + M_d \frac{di_q}{dt} + \frac{\partial \psi_d}{\partial \theta_e}\omega_e, \tag{2.1.14}$$

$$\frac{d}{dt}\psi_q = \tilde{L}_q \frac{di_q}{dt} + M_q \frac{di_d}{dt} + \frac{\partial \psi_q}{\partial \theta_e}\omega_e. \tag{2.1.15}$$

It is now assumed that the change in flux-linkage with change in rotor position $\frac{\partial \psi}{\partial \theta_e}$ is negligible (which is a fair assumption when using a skewed rotor [36]). In actual fact the flux-linkage is indeed a function of the rotor position because of stator slot openings as in [35] which has a direct effect on the torque ripple of the machine [37]. The assumption simplifies the stator voltage equations so that the direct and quadrature axis components are

$$v_d = R_s i_d - \omega_e \psi_q + \tilde{L}_d \frac{di_d}{dt} + M_d \frac{di_q}{dt}, \tag{2.1.16}$$

$$v_q = R_s i_q + \omega_e \psi_d + \tilde{L}_q \frac{di_q}{dt} + M_q \frac{di_d}{dt}. \tag{2.1.17}$$

These equations can be understood using an electrical circuit diagram representation as shown in Figure 2.2. Decoupled quantities are represented as resistive and inductive elements, since their voltage potential is directly proportional to the corresponding current in that circuit. Coupled quantities are represented by voltage sources.

Considering a balanced three-phase sinusoidal voltage excitation in steady state, it is deemed advantageous to work in the dq reference frame, since these values are then DC quantities which are much simpler to control with conventional methods. This is the case, because an evenly distributed constant amplitude sinusoidal excitation creates a rotating magnetic field of constant strength and the dq-reference frame rotates synchronously at the same frequency. Furthermore, considering analysis of the RSM in variable speed, a per-phase model is not applicable since it is only valid under steady state [38].

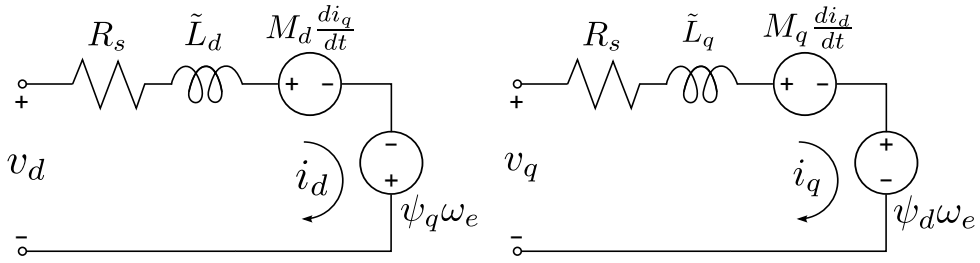

Figure 2.2: Electrical circuit representation of the RSM in $dq0$ reference frame.

2.2 Mechanical Model

Torque in a reluctance machine is produced by the alignment of the minimum reluctance path of flux in the rotor (d-axis) with the rotating magnetizing MMF caused by the stator currents (in the case of AC voltage excitation) called the reluctance effect [39]. The electromechanical torque, τ, produced by a RSM in terms of dq quantities is expressed

$$\tau = \frac{3}{2} p(L_d - L_q) i_d i_q, \tag{2.2.1}$$

where L is the linearised inductance $L = \frac{\psi}{i}$. Without taking magnetic saturation into account the tangential and linearised inductances would be equal ($\tilde{L}_d = L_d$ and $\tilde{L}_q = L_q$) [35]. The factor $\frac{3}{2}$ in (2.2.1) results from the reference frame transformation used, which is non-power invariant [35]. It is obvious from (2.2.1) that the machine torque capabilities are strongly dependant on the ratio of the direct-axis inductance L_d to the quadrature-axis inductance L_q. This ratio $\chi = \frac{L_d}{L_q}$ is a direct indicator of performance of a reluctance synchronous machine, where higher values relate to higher performance [40]. The mechanical system can be described using the torque equation as

$$\tau = J_{eq} \frac{d\omega_m}{dt} + B_{eq} \omega_m + \tau_L \tag{2.2.2}$$

where τ_L is the load torque, J_{eq} is the equivalent system inertia, and B_{eq} is the equivalent wind and friction in the system. The electrical and mechanical rotor speeds and angles are directly proportional to each other by the number of pole pairs as

$$\omega_e = p\omega_m \tag{2.2.3}$$
$$\theta_e = p\theta_m. \tag{2.2.4}$$

In the following chapters these equations are manipulated further for analysis and control of the RSM and later, rotor position estimation.

2.3 Machine Parameters

This project is concerned with the control of a four pole, transverse laminated RSM with specifications listed in table 2.1. Machine parameters are required for analysis, simulation and control of the machine and are determined by the use of FE software. Because the machine has four poles, only a quarter of the model is used for simulation - which takes into account all possible rotor/stator position combinations. The rotor was designed and manufactured at the Electrical Machines Laboratory at Stellenbosch University, implementing steel laminations. During simulation the full stack length of laminations is taken

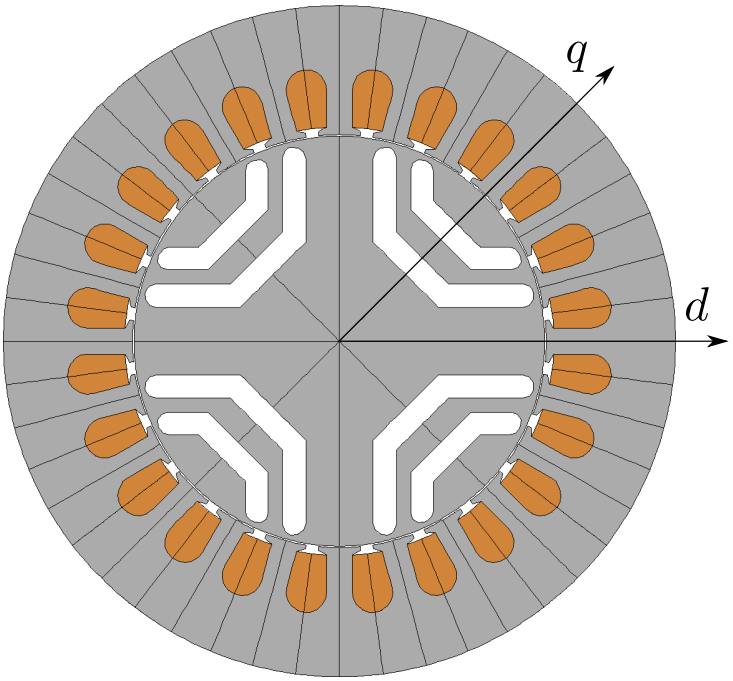

Figure 2.3: The four pole RSM design used for simulation with rotor fixed axis highlighted.

into account. The JMAG® software package coupled with a Python™ script to map the flux linkages is used for simulations.

The machine design shown in Figure 2.3 indicates the d and q axes of the rotor. The d axis is in the direction without flux barriers (rotor slots) - allowing free flow of flux in the steel - in contrast with the q axis where the flow of magnetic flux is inhibited by air regions. This relates to a higher inductance in the d axis, which results to a design characteristic of the RSM in the saliency ratio, defined as $(\tilde{L}_d - \tilde{L}_q)/2$ [4, 5]. The physical rotor can be seen in Figure E.3 in Appendix E.

A static analysis displaying magnetic flux density and contour plots at rated current and speed of the machine is shown in Figure 2.4. Notice the high flux density and corresponding flux contours in the stator in the d axis compared to the low flux density in the q axis. Hotter colours represent higher magnetic flux density.

2D static analysis at various rotor positions for a range of excitation states is run to deliver simulated results for the flux linkage of the machine at various current angles and magnitudes, averaged for the different rotor angles. These results are used to map

Table 2.1: Rated RSM drive parameters

Parameter	**Value**
DC Link Voltage	600 V
Nominal Power	1.1 kW
Phase Current	3.54 A (RMS)
Mechanical speed (ω_m)	1500 r/min
Stator Phase Resistance (R_s)	5 Ω
Current Angle (γ)	60°
Pole Pairs (p)	2

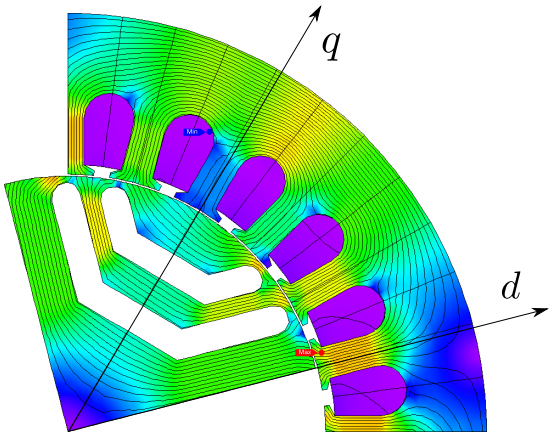

Figure 2.4: A flux density plot of the RSM for a static FE analysis at rated conditions.

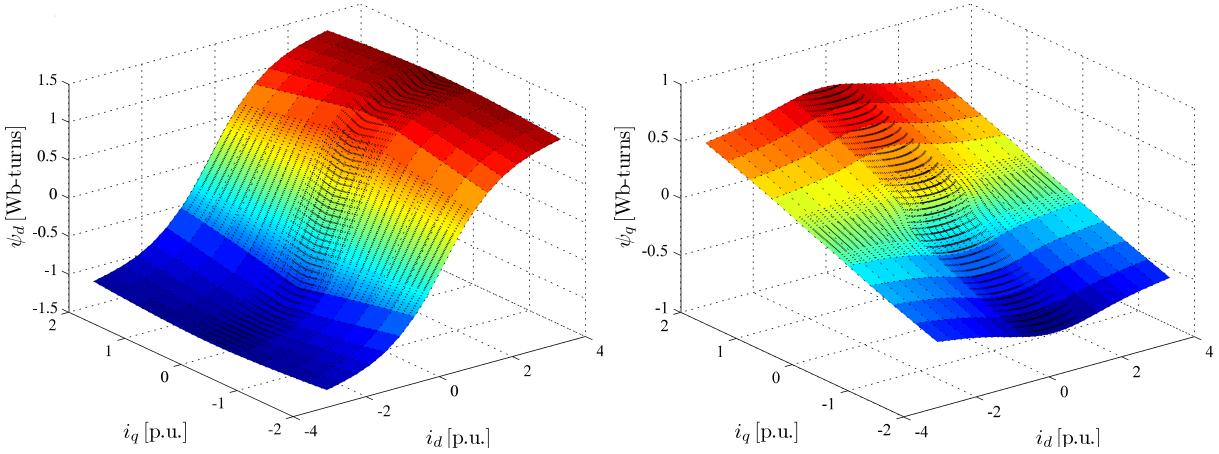

(a) d-axis flux-linkage versus current (b) q-axis flux-linkage versus current

Figure 2.5: Simulated flux-linkage maps determined with FE analysis.

flux-linkages ψ_d and ψ_q as a function of i_d and i_q, shown in Figure 2.5. It should be noted that the per unit base value for these currents are their respective values at rated machine current with rated current angle as given in Table 2.1. Therefore 1 p.u. d-axis current would be 2.5 A_{pk} and 1 p.u. q-axis current is 4.33 A_{pk}. It is obvious that flux-linkage is a non-linear function of current, which is especially evident for ψ_d versus i_d in Figure 2.5a. This is because of magnetic saturation in the steel. Cross-magnetization effects are also visible, since the d-axis flux-linkage changes with q-axis current and ψ_q changes with i_d.

The simulated flux-density maps shown in Figure 2.5 can be derived using physical measurements for more accuracy and verification of the simulation results. This is done using a method explained in [33]. The flux-linkage value can be calculated for a specific current value by

$$\boldsymbol{\psi}_s^r = \mathbf{J}^{-1} \frac{\boldsymbol{v}_s^r - R_s \boldsymbol{i}_s^r}{\omega_e}, \tag{2.3.1}$$

where

$$\mathbf{J} = \begin{bmatrix} 0 & -1 \\ 1 & 0 \end{bmatrix}. \tag{2.3.2}$$

The flux-linkage map is derived by driving the RSM at a constant speed ω_e externally, applying a constant current control $\boldsymbol{i}_s^r$ and measuring the applied voltage $\boldsymbol{v}_s^r$. It is assumed

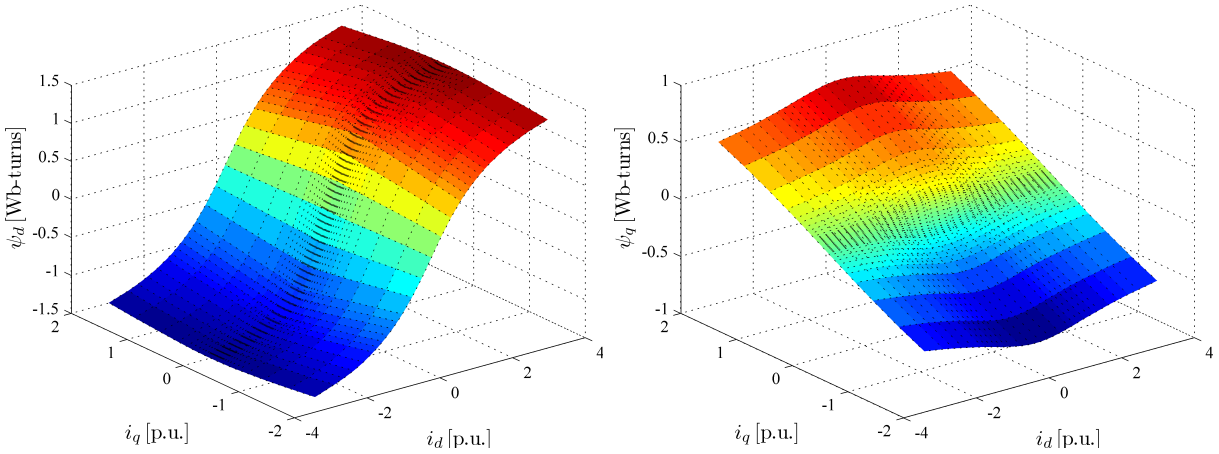

(a) d-axis flux-linkage versus current (b) q-axis flux-linkage versus current

Figure 2.6: Measured flux-linkage maps determined from practical tests.

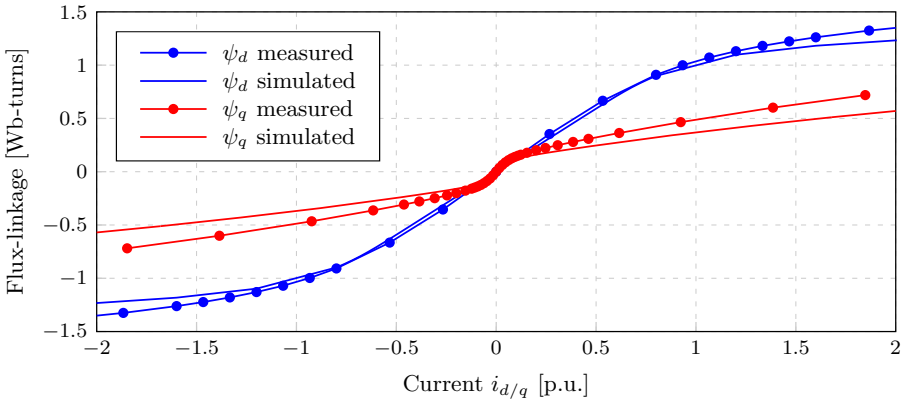

Figure 2.7: Comparison of the measured and simulated flux-linkages versus current.

that the phase resistance R_s is known. Using this method the results in Figure 2.6 were obtained, as taken from [33].

In order to compare the accuracy of the simulated FE results the flux-linkage ψ, tangential inductance $\tilde{L}$ and linearised inductance L at zero cross-magnetization for the measured and simulated maps are plotted. This is done by taking the d- and q-axis values for ψ, $\tilde{L}$ and L at zero q- and d-axis currents respectively.

The measured and simulated uncoupled flux-linkage versus current plots are shown in Figure 2.7 for comparison. It is evident here that saturation effects in the physical machine is less pronounced than in simulations. Notice how the measured flux-linkage plot rises above the simulated plot around and beyond the saturation point. In Figure 2.8 the measured and simulated tangential and linearised inductances are compared. The d-axis inductances differ quite significantly, especially at lower currents. This has an effect on the actual saliency ratio of the machine. Uncertainty about the actual steel used in manufacturing of the machine is the most probable cause of these discrepancies, since FE simulations usually result in much more accurate values [41]. Furthermore, 2D FE analysis using JMAG does not include end-winding inductances which could relate to a difference between measured and simulated machine inductances, although this should not normally contribute to as much of a difference.

Subsequently, for control and simulation purposes in this project, the measured results are used in look-up tables (LUTs) since they represent the physical machine parameters.

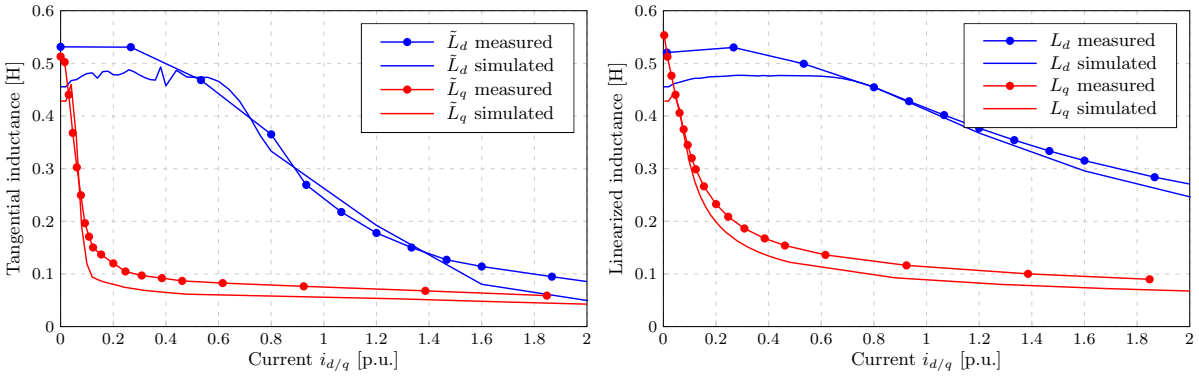

(a) Tangential inductance versus current (b) Linearized inductance versus current

Figure 2.8: Comparison of the measured and simulated inductance plots.

The mechanical parameters of the system in (2.2.2) are determined roughly to create a starting point for the speed controller design. The equivalent wind and friction coefficient, B_{eq}, would be zero in a perfect system, but it has some value because of the bearings on the rotor and wind turbulence. It is taken as a small value

$$B_{eq} = 1 \times 10^{-3} \ \frac{\text{Nm.s}}{\text{rad}}. \tag{2.3.3}$$

The equivalent moment of inertia, J_{eq}, is derived by taking the rotor structure as a solid cylinder. This simplification disregards the flux barriers (air regions) and difference in shaft and lamination materials. The calculated value is used as part of the design of the machine speed controller so the practical difference is subsequently compensated for. From [42] the mass moment of inertia of a solid cylinder with mass m and radius r is calculated as

$$J = \frac{1}{2} m r^2. \tag{2.3.4}$$

The mass is calculated for a solid volume with density ρ and volume v

$$m = \rho \text{v} \tag{2.3.5}$$

so that for the rotor using M470-50A steel with density 7700 kg/m^3, radius r_{rotor} = 39.7 mm, and stack length l_{stack} = 122 mm the inertia is calculated

$$J_{eq} = \frac{1}{2} \rho \pi r_{rotor}^2 l_{stack} . r_{rotor}^2 \tag{2.3.6}$$

$$= 3.665 \times 10^{-3} \text{ kg.m}^2. \tag{2.3.7}$$

This value is applicable to the machine unconnected to a load which would have an added inertia and wind and friction component, but is used for the speed controller design as the differences would entail slower speed response than anticipated.

2.4 Simulation Model

This section describes the Matlab® Simulink® model used to simulate the RSM electrical and mechanical characteristics in order to derive appropriate controllers and implement

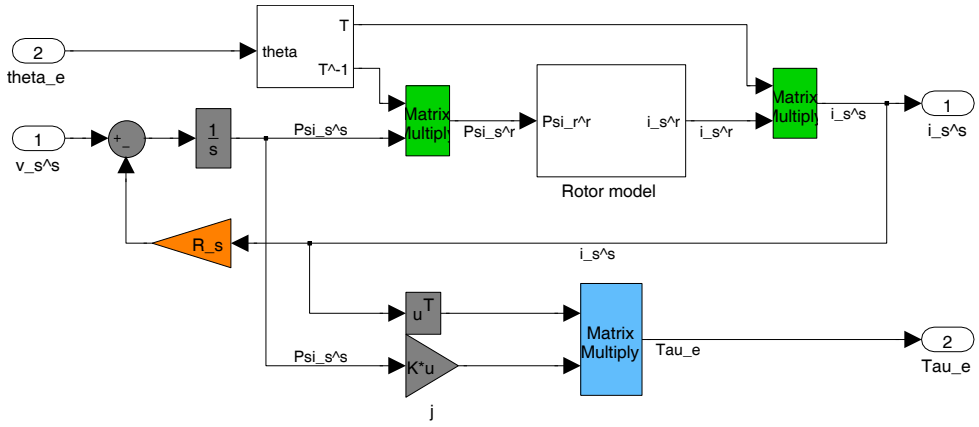

Figure 2.9: The simulation block diagram of the electrical model of the RSM.

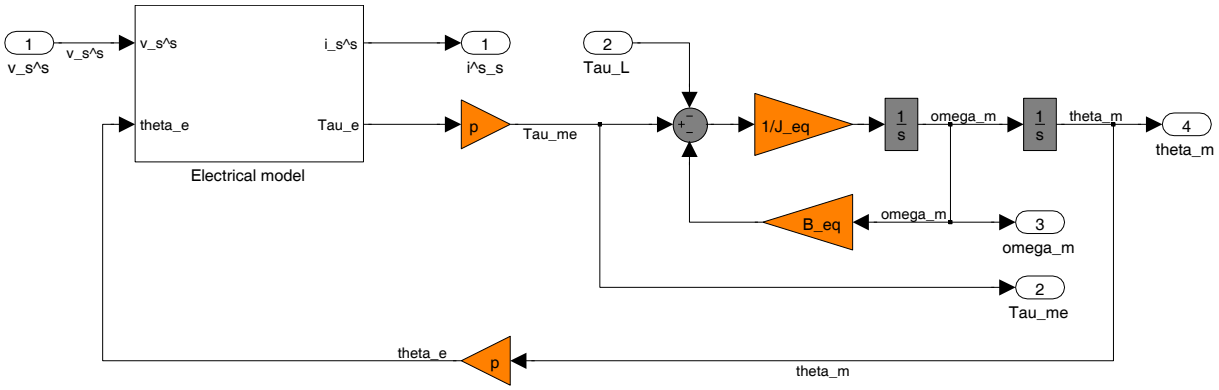

Figure 2.10: The simulation block diagram of the mechanical model of the RSM.

various estimation techniques before practical tests. This greatly accelerates prototyping, because changing model elements is fast and any system variable can be analysed.

The Simulink model implements the flux-linkage maps derived in section 2.3 that are plotted in Figure 2.6 as part of a block diagram representation of the electrical and mechanical equations derived in this chapter describing the machine. This results in an ideal model of the drive system disregarding inverter non-linearities, measurement offsets and noise, voltage modulation, etc.

The electrical model of the machine is simulated using the block diagram model in Figure 2.9. The rotor model consists of a linear inverse interpolation of rotor d/q-axis flux-linkages from the measured flux-linkage versus current tables to result in the rotor d/q-axis currents. This is combined with (2.1.2) and (2.2.1) to result in a model that takes the stator voltage $\boldsymbol{v_s^s}$ and electrical rotor angle θ_e as inputs and delivers the stator current $\boldsymbol{i_s^s}$ and electrical torque τ_e as outputs. Since the voltage equation is implemented in stator reference frame the model inherently includes cross-saturation effects and speed voltage terms.

The mechanical model of the machine is simulated using the block diagram model in Figure 2.10. This includes the electrical model of Figure 2.9 and is a block diagram representation of (2.2.2). The model takes the stator voltage $\boldsymbol{v_s^s}$ and load torque τ_L as inputs and delivers the stator current $\boldsymbol{i_s^s}$, electromechanical torque τ_{em}, mechanical angular speed ω_m, and mechanical rotor position θ_m as outputs.

Chapter 3

Control of the RSM

This chapter discusses the control methodology used considering the RSM. The drive system and rapid prototyping system is described followed by the design of the current and speed controllers. Each of the controller sections include simulation and practical results to show their functionality.

3.1 Drive System

Since open-loop control of the RSM has very low performance [43], closed-loop vector voltage control (VVC) (also known as FOC) is normally implemented. Considering (2.1.16) and (2.1.17) the stator currents, $i_{d/q}$ ($\boldsymbol{i}_s^r$), can be controlled by the stator voltages, $v_{d/q}$ ($\boldsymbol{v}_s^r$), with knowledge of the machine parameters and rotor speed. Since these equations are in rotor fixed reference frame rotor position information is required, because current measurements are done on stator phase *abc*-axes and have to be transformed. Vector control of the currents result in torque control from (2.2.1) and in turn allows speed and position control of the machine.

The three-phase stator voltages are applied to the machine using a voltage source inverter (VSI) which is controlled using a space vector pulse width modulation scheme (SVPWM). The use of SVPWM allows a maximum voltage vector amplitude of $\frac{\sqrt{3}}{2}V_{DC}$ [44], where V_{DC} is the DC-bus voltage rectified by the inverter from 3-phase mains. The derivation of switching times (duty cycles) for use with SVPWM is discussed in Appendix B. This algorithm calculates the appropriate switching times (d_{abc}) for the DC-AC 3-phase converter with stator voltage references in α/β reference frame, $\boldsymbol{v}_s^s$. Once again, the rotor angle is required since the current control reference quantities, $\boldsymbol{v}_s^r$, are in d/q reference frame.

3.1.1 Layout

Figure 3.1 represents the drive system layout used to control the RSM. A Linux based real time application interface rapid prototyping system is used to run the control algorithm and supply switching signals to the inverter. The RPS design is described in section 3.2. The inverter calculates IGBT switching dead-times from the duty cycles received for the three top semiconductors visible in Figure 3.2 to ensure the top and bottom switches are never closed at the same time. Current and DC-bus voltage measurements, $\boldsymbol{i}_s^s$ and V_{DC}, are also done in the inverter and sent to the RPS. These measurements are sampled at

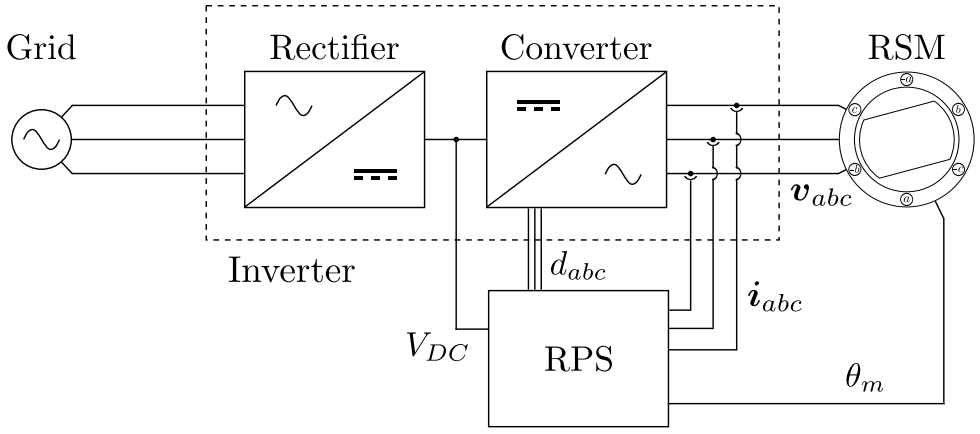

Figure 3.1: The RSM drive layout implemented.

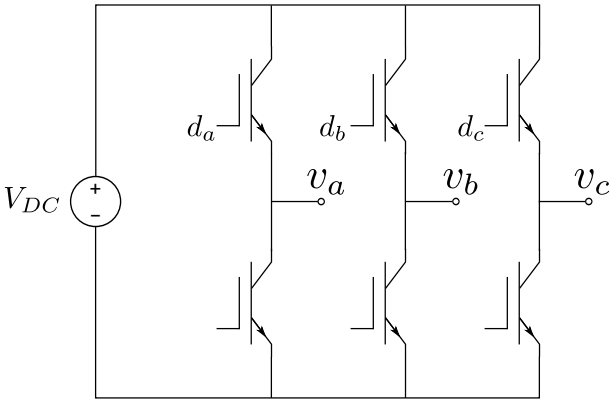

Figure 3.2: The three-phase two-level DC to AC converter layout of the inverter.

the sampling frequency, $F_s = 10$ kHz. The mechanical rotor angle is measured using a position resolver and input to the RPS.

3.1.2 Practical considerations

The RSM d-axis position resolver offset (for rotor zero position, $\theta_m = 0$) is determined by applying a stator voltage with sufficient magnitude of the form

$$\boldsymbol{v}_s^s = \begin{bmatrix} v_\alpha \\ 0 \end{bmatrix} \tag{3.1.1}$$

so that the rotor d-axis aligns with the stator α-axis. The measured position resolver value is then taken as the resolver offset and subtracted from subsequent position resolver measurements to result in the actual mechanical rotor angle θ_m.

The RSM is shaft-connected to an IM that operates as load when the RSM is speed controlled. The two machines connected via a torque sensor are shown in Figure 3.3. When testing the current control of the RSM at standstill the shaft is held stationary using a clamp while current control at speed is tested by operating the IM under speed control.

Each machine is controlled using a separate RPS with two back-to-back connected inverters sharing a DC-bus voltage. This allows energy flow between generator and machine so that testing is more energy efficient. When the RSM is speed controlled a positive torque from the IM (with the direction of rotation) would require a negative torque from

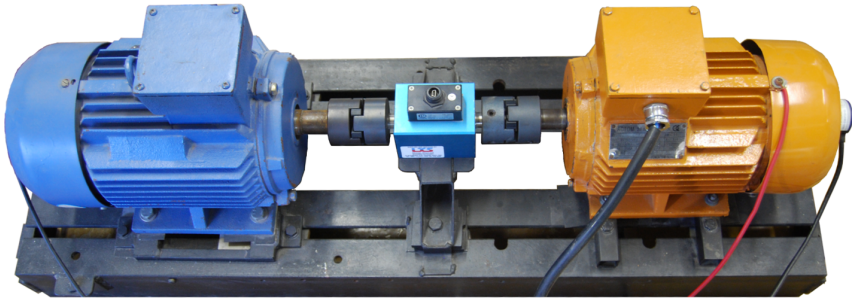

Figure 3.3: The shaft-connected test bench machines. RSM - Orange, IM - Blue.

the RSM (against the direction of rotation) to brake the shaft - relating to a negative current (generator action) for the RSM. A negative torque from the IM relates to force against the direction of motion requiring positive torque from the RSM and therefore positive current (motor action) for the RSM. Note that this is referring to rotation in the direction shown in Figure 2.1 and that negative rotation would constitute a sign change for the RSM currents mentioned.

Figure E.1 Appendix E contains a photograph of the test bench used while the back-to-back connected inverters are shown in Figure E.5.

3.2 Rapid Prototyping System

This section describes the rapid prototyping system (RPS) that was completed as a precursor to the control research contained in this thesis and used to deliver switching signals to the inverter supplying the RSM for practical validation of the control techniques. The FPGA-based Real-Time RPS was designed at and partly supplied by the Department of Electrical Drive Systems & Power Electronics at the Technical University of Munich.

The RPS runs a Linux real time application interface (RTAI) in which C-code is written as a control algorithm for the drive system. This is interfaced with the FPGA-board which can be seen as a sort of central nervous system that receives all system inputs and controls all outputs.

Appendix E contains some photographs of the RPS and the board layout.

3.2.1 System Layout

Figure 3.4 shows a block diagram layout of the RPS showing the input/output variables corresponding to the drive system layout in Figure 3.1. Bus connection widths are indicated by xW, where W is the number of bits. The RTAI system runs on an industrial Pentium® 4 motherboard which is connected to the CPLD and FPGA boards via an ISA connector. Since the FPGA has a limited number of pins the ISA bus is split between the FPGA board for to/from data-handling using 16 bits and the 21 address-bits (20 address plus one BALE signal) are connected to the CPLD. The 21-bit RTAI address-instruction received on the CPLD is mapped onto 5 bits depending on the sign of the BALE signal and the validity of the address. Two supplementary logic signals controlling read/write (IO) of the data bus are routed through the CPLD from the RTAI system to the FPGA. Depending on the sign of the IO signals the FGPA or the RTAI system takes control of the 16-bit data bus between them. Finally an interrupt signal from the FPGA to the RTAI PC is routed through the CPLD for initialisation and timing of the control algorithm.

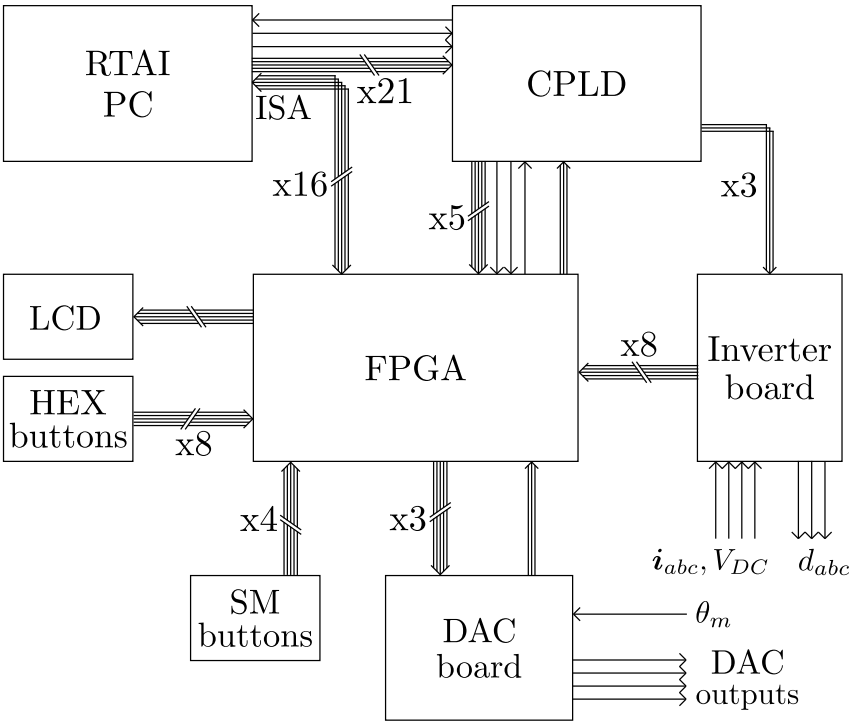

Figure 3.4: A block diagram representation of the rapid prototyping system layout.

The optical-transmitters for the PWM duty-cycle signals (d_{abc}) are situated on the CPLD board so that the PWM signals generated on the FPGA are sent from the FPGA to the CPLD via a 3-bit connection. Optical-fibre cables connect the PWM-outputs on the CPLD to an inverter board that is used for inverter connection interfacing. The PWM duty-cycles are sent from the inverter board via BNC-connected co-axial cables. Implementing the optical transmitters on the CPLD board allows great flexibility for more complex inverter switching topologies. It also allows implementing inverter dead-time compensation on the RPS so that high- and low-level switching signals can be output directly from the CPLD board with only high-level switching signal inputs from the FPGA. Current measurements and the DC-bus voltage ($\boldsymbol{i}_{abc}$ and V_{DC}) are received also via BNC-connected co-axial cables. These measurements are sent to the FPGA board from the inverter board using shielded ethernet cables via RJ-45 connectors implementing differential signalling which allows a long distance between the inverter (and adjacent inverter board) and the RPS.

Encoder measurements of the mechanical rotor angle is input via the DAC-board to the FPGA. Four DAC channels are available for viewing measurement- and control status-outputs using for example an oscilloscope. A 3-bit Serial Peripheral Interface bus connecting the FPGA board to the DAC board controls the DAC chip. An LCD is used to display the control status and hex button values that are changed using eight push buttons arranged in two rows. Four additional buttons are connected to the FPGA for state machine (SM) control.

3.2.2 Control Algorithm

The RTAI control algorithm written in C is executed at every switching cycle (after every ΔT_s) and used as the high-level drive system controller. RPS measurements, inputs and outputs controlled by the FPGA are available in the RTAI environment and implemented

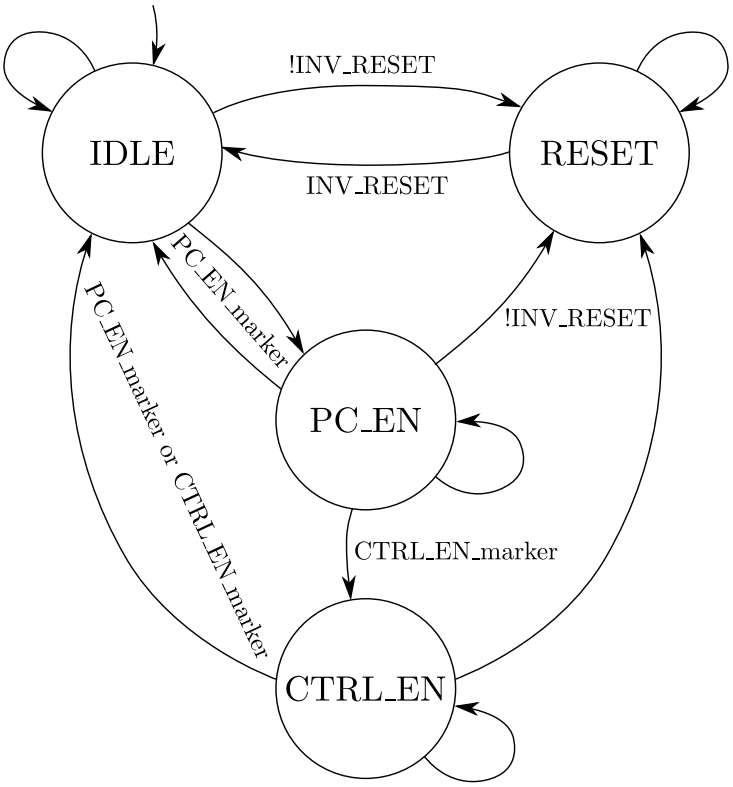

Figure 3.5: The state machine followed by the RPS FPGA.

to realise an emulated version of the controllers designed in the previous chapters. The measured quantities and control outputs are updated after every switching cycle and real time user control is realised using the hex button array. The button controlled hex value is also accessible in the RTAI environment and can be used to set control values as required for example the reference current, speed or torque and rotation direction. The result is an easily modifiable control system with a lot of flexibility and room for complex nested controllers.

The FPGA-system operates as a state machine in the form of Figure 3.5. When the system is started up it enters the IDLE state after initialising the ADCs, DACs, LCD, etc. The PC_EN_marker is sent from the RTAI system when a control algorithm is compiled and ready to be run. This moves the state machine to an intermediate state, PC_EN, where secondary acknowledgement is required from the user by pressing the control enable button (sending the CTRL_EN_marker). The state machine then moves to the CTRL_EN state where the PWM signals are enabled and the RTAI control algorithm is processed at every switching cycle. Control is disabled by removing the RTAI control algorithm (sending PC_EN_marker) or pressing the required button (CTRL_EN_marker) in order to return to the IDLE state. If at any time a inverter reset signal is received (INV_RESET with inverse logic) the system goes to the RESET state. Return to the IDLE state is done by pressing the required button to reset the INV_RESET signal.

Direct return to the IDLE state from the CTRL_EN state on pressing of the control enable button was implemented for safety reasons for complete removal of the control algorithm during initial testing and implementation of the system. It is the author's recommendation to change the state machine behaviour so that the system would return to the PC_EN state on reception of the CTRL_EN_marker (control enable button press) when in the CTRL_EN state in order to allow more rapid application of control during subsequent tests when there is no change to the control algorithm code. Safety is still

intact since the control algorithm can be instantly stopped (with switching signals to the inverter removed) when the inverter reset button is pressed and return to the idle state can be initiated by the RTAI system sending the PC_EN_marker.

3.3 Current Control

As mentioned in the introduction of this chapter the physically measured quantities of the machine and the inverter reference voltages are in stator fixed reference frame. The simulation model used is built around the flux-linkage LUTs derived in Chapter 2 which are developed in rotor reference frame. In order to include speed voltages and mutual inductances to the simulation model, the flux-linkages are calculated from the LUTs to the stator reference frame as $\boldsymbol{\psi}_s^s$. Subsequently the electrical model in simulation is formed in stator reference frame from (2.1.2). The derived mathematical model of the machine is in rotor fixed reference frame, allowing derivation of a transfer function (TF) in the rotor reference frame. Therefore, the current controllers are designed in rotor reference frame. In order to directly compare simulation and practical setups using the rotor angle as part of the controllers and transformation between reference frames the control is done in rotor fixed reference frame while the machine model is in stator fixed reference frame as explained above.

The continuous TF model of the machine is now derived from (2.1.16) and (2.1.17), followed by a discretization of the model so that it can be controlled using a digital system.

3.3.1 Continuous model

The mutual inductance terms, $M_{d/q}$, in the stator voltage equations are left out in the control, because they are relatively small compared to the other terms and with a sufficient gain the integral component of the PI current controller used compensates for the target offset. As mentioned during the mathematical derivation in Chapter 2 the change in flux-linkage with rotor position is neglected. This offset is also compensated for with the integral PI term.

The simplified stator voltage equations are now equal to

$$v_d = R_s i_d - \omega_e \psi_q + \tilde{L}_d \frac{di_d}{dt}, \tag{3.3.1}$$

$$v_q = R_s i_q + \omega_e \psi_d + \tilde{L}_q \frac{di_q}{dt}. \tag{3.3.2}$$

Taking the Laplace transform $\mathcal{L}_t\{f(t)\}$ to the s-domain results in

$$V_d = R_s I_d - \omega_e \Psi_q + s\tilde{L}_d I_d, \tag{3.3.3}$$

$$V_q = R_s I_q + \omega_e \Psi_d + s\tilde{L}_q I_q \tag{3.3.4}$$

where $V_d = V_d(s)$, etc. It is evident that the voltage equations can be completely decoupled by removing the speed voltage terms $\omega_e \Psi$. The speed voltages are compensated for later in the control scheme (but the effect of ignoring it is also shown). Rearranging now to give equations for the currents result in

$$I_d = \frac{V_d}{R_s + s\tilde{L}_d}, \tag{3.3.5}$$

$$I_q = \frac{V_q}{R_s + s\tilde{L}_q}. \tag{3.3.6}$$

To calculate gains for the PI controller the current equations are used to obtain the following 1st-order decoupled TFs representing the machine current response characteristics:

$$G_d(s) = \frac{1/\tilde{L}_d}{s + R_s/\tilde{L}_d}, \tag{3.3.7}$$

$$G_q(s) = \frac{1/\tilde{L}_q}{s + R_s/\tilde{L}_q}. \tag{3.3.8}$$

It should be noted that this model is applicable to the machine at standstill ($\omega_e = 0$) with constant inductances $\tilde{L}_{d/q}$ and stator resistance R_s. It is very obvious from the inductances of Figure 2.8 that this is not the case for the RSM, but taking the inductance values for the machine at a chosen working point - the rated load conditions - one can design the controller with sufficient prediction of its response characteristics. This results in a greatly simplified controller design process with sufficient dynamics that does not require adaptation.

Since the stator voltages are applied by an inverter system the applied voltage lags the reference voltage because of inverter switching dead-times as shown in [45]. This results in an added delay component in the system which can be modelled by

$$F_{inverter}(s) = \frac{\boldsymbol{v}_s^s(s)}{\boldsymbol{v}_{s,ref}^s(s)} = e^{-sT_{dead}} \tag{3.3.9}$$

$$\approx \frac{1}{1 + sT_{dead}}, \tag{3.3.10}$$

where T_{dead} is the switching dead-time added by the inverter. Inverter dead-time can be compensated for by adding this model to the controller design, modifying the reference PWM voltage, adding a logical compensation circuit, etc. In this project the effects of inverter dead-time was disregarded initially and satisfactory results were obtained so that it was not compensated for. Further work could include dead-time compensation for more predictable behaviour, or adding the dead-time model in simulation for improved simulation/practical correlation.

3.3.2 Discrete model

The system used implements a digital controller, implying that the controller will sample measurements for input and output discrete values. The basic block diagram of the control system is illustrated in Figure 3.6. The switch represents sampling every switching cycle with period T_s and $G_{ho}(s)$ represents the zero-order hold (ZOH) model of the digital-to-analog converter (DAC) supplying control signals to the inverter. $D(z)$ is the digital controller and $r(t)$ is the reference signal i.e. $i_{d/q}$. The sampling model of the analog-to-digital converter (ADC) is moved to after the subtraction, $e(t) = r(t) - y(t)$, which differs from the actual system where sampling of the measured signal $y(t)$ is done before subtraction is done discretely. This change makes no difference practically as the sampling is still accounted for.

To proceed the ZOH model is added to the plant model, $G(s) = G_{d/q}(s)$, during discretization to result in the ZOH equivalent of $G(s)$

$$G(z) = \frac{z-1}{z}\mathcal{Z}\left\{\frac{G(s)}{s}\right\} \tag{3.3.11}$$

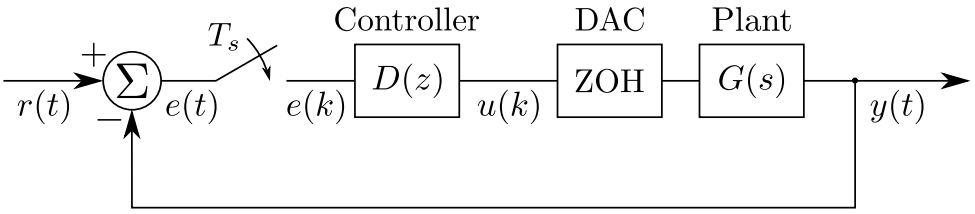

Figure 3.6: The simplified discrete current controller block diagram.

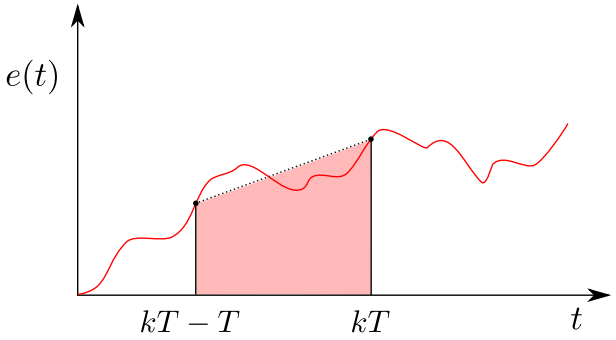

Figure 3.7: Trapeziodal integration done at each step of the bilinear approximation.

which is transformed to the w-plane using Tustin's method by taking

$$G(\mathrm{w}) = G(z) \mid_{z = \frac{1 + \frac{T}{2}\mathrm{w}}{1 - \frac{T}{2}\mathrm{w}}} . \tag{3.3.12}$$

Tustin's method (or the bilinear approximation) approximates the continuous input by a straight line between samples, implementing trapezoidal integration at each step to materialize a discrete integrator [46]. Figure 3.7 illustrates trapezoidal integration. This method takes the integral as the area of the shaded trapezium as opposed to the area under $e(t)$ over the last period T. Evidently, with higher frequency (smaller T) more accurate results will be achieved.

Mapping from the continuous s-plane to the discrete z-plane (or vise-versa) using the bilinear transformation is done by substituting

$$s = \frac{2}{T}\left(\frac{z-1}{z+1}\right) \tag{3.3.13}$$

or

$$z = \frac{1 + \frac{T}{2}s}{1 - \frac{T}{2}s}. \tag{3.3.14}$$

Through the z- and w-transform the primary strip on the left half s-plane in between $^{j\omega_s}/_2$ is mapped on to the unit circle in the z-plane, and back onto the entire left half of the w-plane [47]. This transformation is always stable since it maps from the left half s-plane. The frequency is warped since the primary strip of the left half s-plane is mapped to the entire left half w-plane [47]. Therefore the w-plane is equal to the s-plane with a warped frequency axis where the bilinear transformation frequency, $\tilde{\omega}$, results from the true frequency, ω, as

$$\tilde{\omega} = \frac{2}{T}\tan\left(\frac{\omega T}{2}\right). \tag{3.3.15}$$

It can be shown that for sampling frequencies $\omega_s = \frac{2\pi}{T_s} >> 4\omega$ the bilinear transformation frequency is approximately equal to the true frequency. Therefore, with a sufficiently high sampling frequency (and control system) the discrete system will behave satisfactory compared to the continuous system when using the w-plane design.

Subsequently, a continuous controller, $D(s)$, is designed for the new plant, $G(\mathrm{w})$, using conventional techniques and transformed back to the z-plane using the inverse bilinear transform equivalent to result in the discrete controller as

$$D(z) = D(\mathrm{w})|_{\mathrm{w} = \frac{2}{T}\left(\frac{z-1}{z+1}\right)}. \tag{3.3.16}$$

In order to more accurately model the digitization in such a control system with ZOH a bilinear transformation with pre-warping can be implemented as in [48] which does not have extra phase-lag compared to the original continuous controller at frequency ranges comparable to the Nyquist frequency. It was deemed unnecessary to implement these further measures as the system sampling frequency of 10 kHz would allow controlling the current sufficiently fast.

Following these steps results in the ZOH-compensated current models in discrete form

$$G(z) = \frac{z-1}{z}\mathcal{Z}\left\{\frac{1/\tilde{L}}{s(s + R_s/\tilde{L})}\right\} \tag{3.3.17}$$

$$= \frac{1 - e^{-R_s T_s/\tilde{L}}}{R_s(z - e^{-R_s T_s/\tilde{L}})}. \tag{3.3.18}$$

Now the TF can be mapped to the w-plane by applying (3.3.12)

$$G(w) = \frac{1 - e^{-R_s T_s/\tilde{L}}}{R_s\left(\frac{1+\frac{T_s}{2}\mathrm{w}}{1-\frac{T_s}{2}\mathrm{w}} - e^{-R_s T_s/\tilde{L}}\right)} \tag{3.3.19}$$

$$= \frac{\left(\frac{e^{-R_s T_s/\tilde{L}}-1}{R_s(e^{-R_s T_s/\tilde{L}}+1)}\right)\mathrm{w} + \frac{2(1-e^{-R_s T_s/\tilde{L}})}{R_s T_s(1+e^{-R_s T_s/\tilde{L}})}}{\mathrm{w} + \frac{2(1-e^{-R_s T_s/\tilde{L}})}{T_s(1+e^{-R_s T_s/\tilde{L}})}}. \tag{3.3.20}$$

Evidently, the ZOH-compensation adds a zero in the right half plane when comparing to (3.3.7) and (3.3.8), but it is shown later that this zero's effect is at such a high frequency that it can be ignored.

3.3.3 Current controller

The machine current vector, $\boldsymbol{i}_s$, is controlled using FOC in order to produce close to the highest efficiency. This is done by implementing constant current angle control (CCAC) as in [36] to result in maximum torque per ampere (MTPA). This is opposed to constant field current control (CFCC) which is simpler to implement and takes the d-axis current as a constant, only changing q-axis current for torque control. The current vector for CCAC is shown in Figure 3.8 where the current angle, γ, is kept constant and the current vector length/magnitude is varied. The reference d/q-axis current magnitudes are calculated from the reference stator current magnitude as

$$i_d = |\boldsymbol{i}_s|\cos(\gamma), \tag{3.3.21}$$

$$i_q = |\boldsymbol{i}_s|\sin(\gamma). \tag{3.3.22}$$

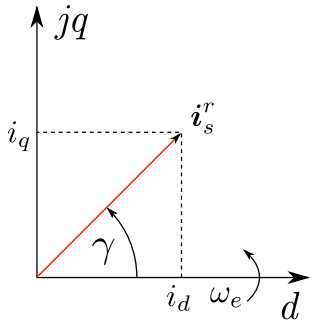

Figure 3.8: The Current vector controlled at constant angle.

Negative torque (negative current) is produced by changing the sign of the q-axis current so that the stator current vector in rotor reference frame is in die fourth quadrant. This operates the machine as a generator (when the rotational speed is positive).

As mentioned earlier, for controller design purposes the machine inductances $\tilde{L}_{d/q}$ are taken at a specific working point - the rated current conditions - where

$$\boldsymbol{i}_s^r = 5\angle 60°\text{A}. \tag{3.3.23}$$

At this current the machine inductances are from Figure 2.8

$$\tilde{L}_d = 0.1318 \text{ H}, \tag{3.3.24}$$

$$\tilde{L}_q = 0.0443 \text{ H}. \tag{3.3.25}$$

Stator resistance is taken as the measured 'cold' value from Table 2.1. This value will change when the motor gets warmer under load, but it was deemed to be out of the scope of this thesis to determine the actual resistances. Resistance adaption as in [25] can be implemented to compensate for these changes in further studies. The continuous TFs resulting from these values are

$$G_d(s) = \frac{7.587}{s + 37.94}, \tag{3.3.26}$$

$$G_q(s) = \frac{22.57}{s + 112.9}. \tag{3.3.27}$$

With a sampling time of $T_s = {}^1/_{F_s} = 0.1$ ms the ZOH-compensated TFs in the w-plane are

$$G_d(\text{w}) = \frac{-0.0003794\text{w} + 7.587}{\text{w} + 37.94}, \tag{3.3.28}$$

$$G_q(\text{w}) = \frac{-0.001129\text{w} + 22.57}{\text{w} + 112.9}. \tag{3.3.29}$$

As mentioned earlier one can see that the ZOH-compensation adds a fast zero in the right-half plane. Now current controllers can be designed for the plants in order to achieve the desired current response.

A PI controller is implemented for current control, because it will deliver fast transient response as well as a zero steady state error for this plant. The design is done using the Matlab® rltool function. This function plots the root locus, frequency response, and step-response plots for a given model and allows real-time compensator design by adding zeros/poles and changing the loop gain to result in the required response characteristics.

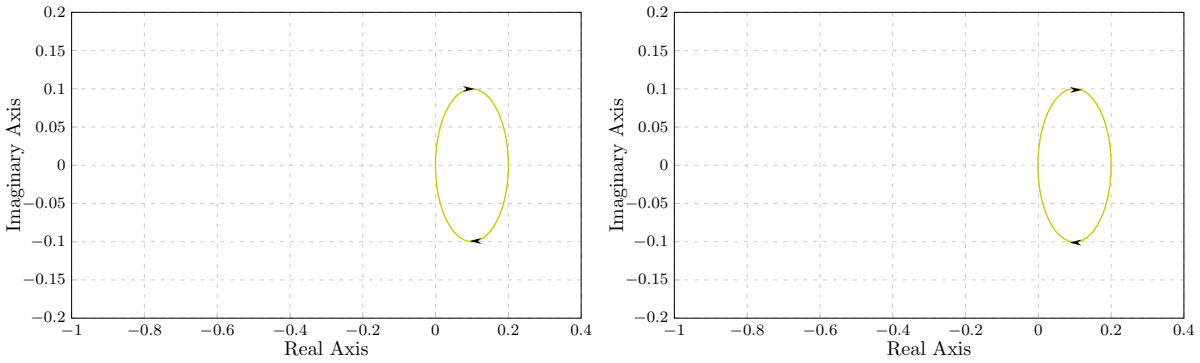

(a) G_d(w) nyquist plot (b) G_q(w) nyquist plot

Figure 3.9: The d/q-axes current model open-loop Nyquist plots.

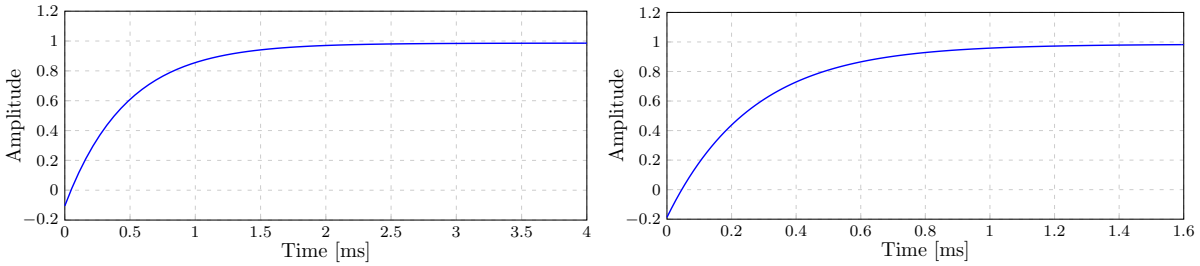

(a) d-axis current (b) q-axis current

Figure 3.10: The simulated d/q-axes current step responses from root locus plots.

Using resources such as Matlab greatly accelerate design times for varying or new systems, because a change in the plant simply constitutes a change in the model variables. Following the same modular process for any plant to design the compensator therefore is immensely fast compared to designing the compensator by hand. It can also be used to verify hand calculations.

The open-loop Nyquist plots for the d/q-axes current models described by (3.3.28) and (3.3.29) are shown in Figure 3.9. These are non-minimum phase systems (because of the zeros in the right half plane) with the maximum group delay of the set of systems that have the same magnitude response, therefore maximum-phase. The contours have no clockwise/counter-clockwise rotations around the point (-1,0) indicating that the systems are stable [46]. The use of Nyquist plots allows a fast and easy determination of the stability of the controller without too much concern for the dynamics.

PI controllers (3.3.30) and (3.3.31) are now added using the Matlab rltool to result in simulated current step responses shown in Figure 3.10. The d-axis current has a 2% settling time of 2.33 ms while the q-axis current has a 1.31 ms settling time. Both systems exhibit no overshoot and some negative initial response, especially evident from the q-axis response in Figure 3.10b which is explained by the zero in the right half plane. These are ideal current step responses as they are very fast, exhibit no oscillation, no overshoot and zero steady state error. It is pointed out again that these models disregard the machine speed voltages and take the resistance and inductances as constant values at the rated conditions in order to result in a simple controller. A more realistic analysis of the controller is done hereafter using a complete electrical machine model.

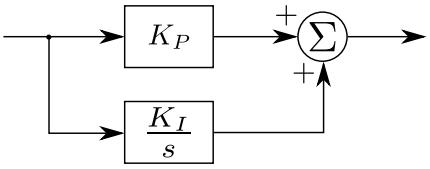

Figure 3.11: Proportional/Integral controller block diagram layout.

Table 3.1: Current controller gains

Gain	**Value**
K_{Pd}	250
K_{Pq}	140
K_{Id}	2500
K_{Iq}	8400

The resulting current controllers in continuous domain are

$$D_d(s) = 250\frac{(s+10)}{s}, \tag{3.3.30}$$

$$D_q(s) = 140\frac{(s+60)}{s} \tag{3.3.31}$$

so that for a PI controller layout as in Figure 3.11 with TF (3.3.32) the continuous controller gains are as listed in Table 3.1. On investigation it can be found that the controller zero is placed far below (closer to the origin) the plant pole in order to produce a closed loop pole close to the origin. The pole-cancellation method is not used since the plant models are known to be very variable so that with a change in the plant pole position the transient closed loop behaviour of the system would not be affected severely.

$$PI(s) = K_P\frac{(s+\frac{K_I}{K_P})}{s} \tag{3.3.32}$$

Current PI controller saturation is also implemented to eliminate integrator runaway. This is done by disabling the integrator when the current controller output is larger than the voltage limit of the system (imposed by SVPWM).

As mentioned cross-saturation effects are disregarded in the machine models when designing the current controllers to result in a much simpler solution. This is a common simplification used throughout in literature, but it can cause problems when aiming for ultimate precision. The mutual inductances of the machine in question is plotted versus current in Figure 3.12 showing that the magnitude of the mutual inductances are regularly below 5 mH. In [49] the effects of cross-saturation on saliency based position sensorless control techniques are shown to be significant enough when an accurate control action is required and it is compensated for in [50]. Compensation for mutual inductance requires an accurate machine model and subsequent LUTs, complicating the controller and making it more parameter dependant. One of the possible outcomes of this research is an eventual generic position sensorless controller for any synchronous machine, which requires it to be parameter independent. Therefore it was chosen to not further consider implementation of cross-saturation compensation.

With the completed d/q-axis current controllers designed a speed-uncoupled system is created as in Figure 3.13. The speed voltages are compensated for by adding the

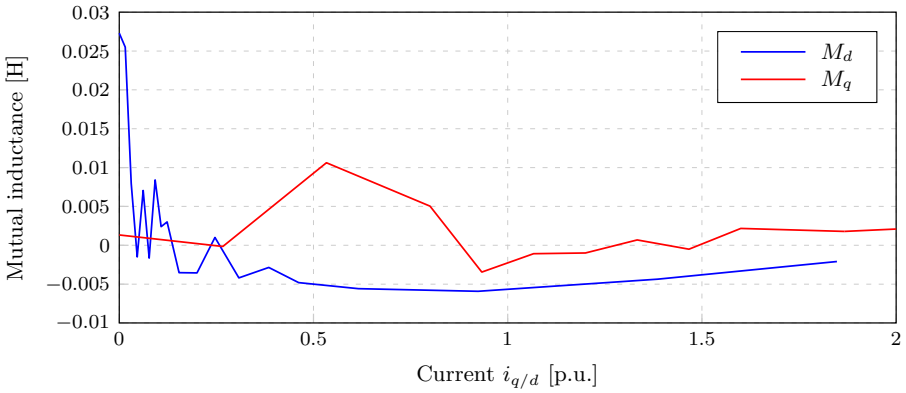

Figure 3.12: The d/q-axes mutual inductance versus current.

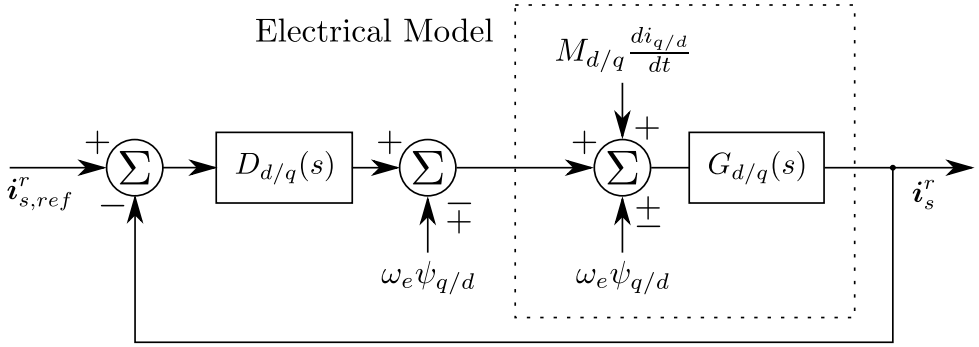

Figure 3.13: The continuous speed-uncoupled current controller block diagram

negative thereof (calculated using a LUT of the machine flux and the measured/estimated speed) to the controller output. The impact of the inclusion/exclusion of speed voltage compensation is shown in simulated and practical results.

3.3.4 Simulation Results

The simulation model derived in section 2.4 is used to test and tune the current controllers before it is implemented practically. This represents a close resemblance to the practical setup, except for the inverter model, measurement errors, etc.

Figure 3.14 representing (3.3.21) and (3.3.22) is the CCAC block diagram that takes the reference stator current magnitude as input and results in the according d/q-axis current reference values at the rated current angle. Figure 3.15 is the speed voltage compensation block diagram that uses a LUT to find the current flux-linkage values from the measured flux maps and multiplies it by the electrical speed of the rotor to result in the speed voltage compensation terms, $\omega_e\psi_{d/q}$. The complete Simulink block diagram used for the current control loop is shown in Appendix D in Figure D.2 containing the mechanical model of the RSM, CCAC block, and speed voltage compensation block from Figures 2.10, 3.15, and 3.14 respectively.

As mentioned in chapter 2 the machine currents are given in per unit scale, where 1 p.u. equals the current value at rated stator current magnitude and current angle. Therefore the rated values for d- and q-axis currents are

$$i_d = 2.5 \text{ A} = 1 \text{ p.u.} \tag{3.3.33}$$

$$i_q = 4.33 \text{ A} = 1 \text{ p.u.} \tag{3.3.34}$$

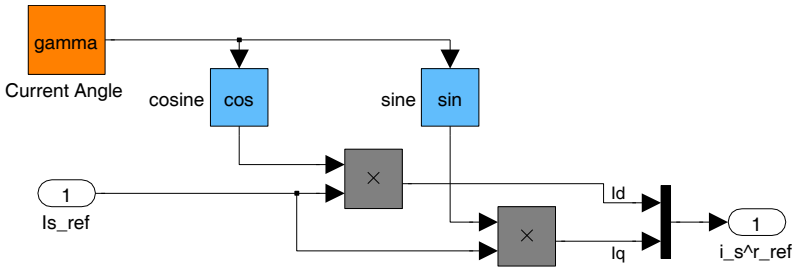

Figure 3.14: The constant current-angle control simulation block diagram.

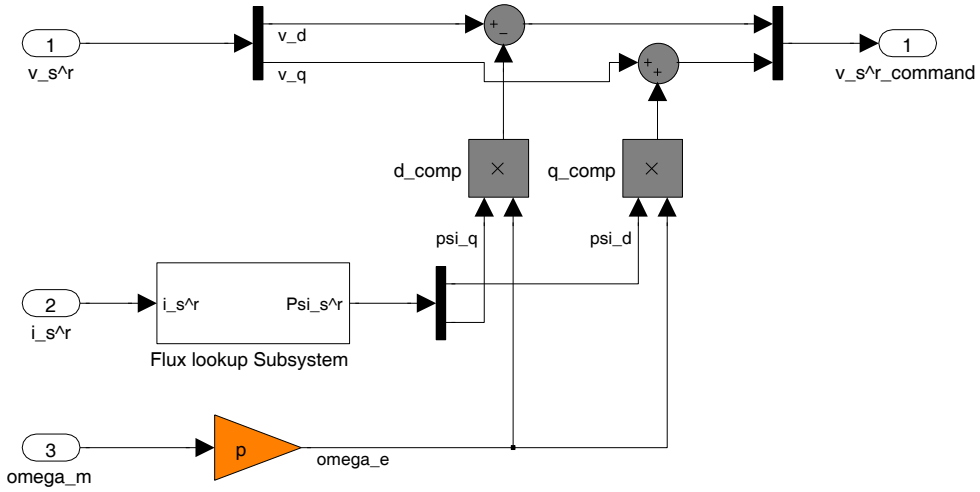

Figure 3.15: The speed voltage compensation simulation block diagram.

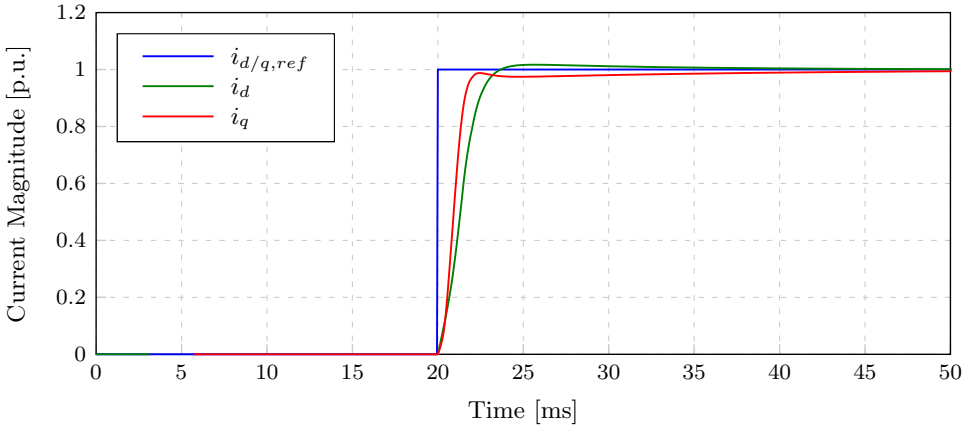

Figure 3.16: Simulation result for the rated-current control step with locked-rotor without speed-voltage compensation plotting reference and actual rotor currents versus time.

with a stator current magnitude of $|\boldsymbol{i}_s| = 5$ A and current angle $\gamma = 60°$.

Figure 3.16 shows a locked-rotor rated-current control step simulation without speed voltage compensation using the controller gains given in Table 3.1. It is evident that the current controllers do not behave as ideally as predicted using the simplified plant models in (3.3.28) and (3.3.29), but they have 2% settling times just about twice as long as the simplified model. This can be attributed mainly to taking the machine inductance terms as constant values as well as disregarding the mutual inductance terms in section 3.3.1.

In Figure 3.17 a rated-current control step simulation without speed voltage compensation at rated speed is shown. Evidently the speed voltage term $\omega_e \psi_{d/q}$ in Figure 3.13

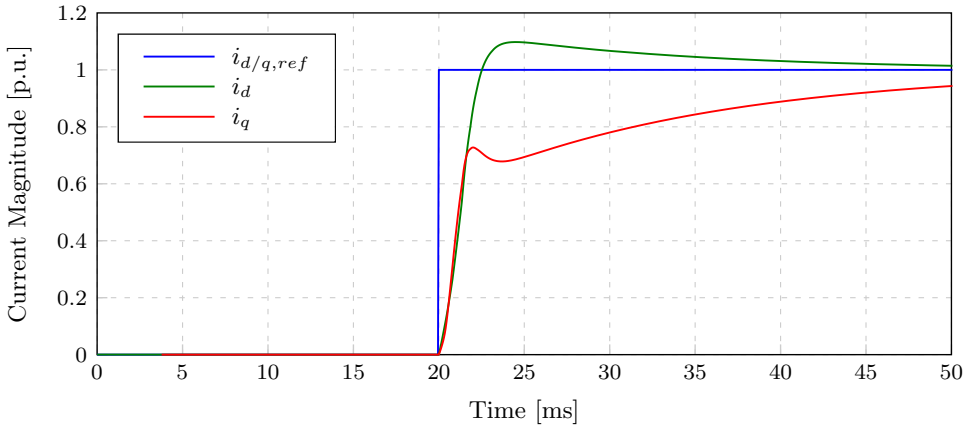

Figure 3.17: Simulation result for the rated-current control step at rated speed without speed-voltage compensation plotting reference and actual rotor currents versus time.

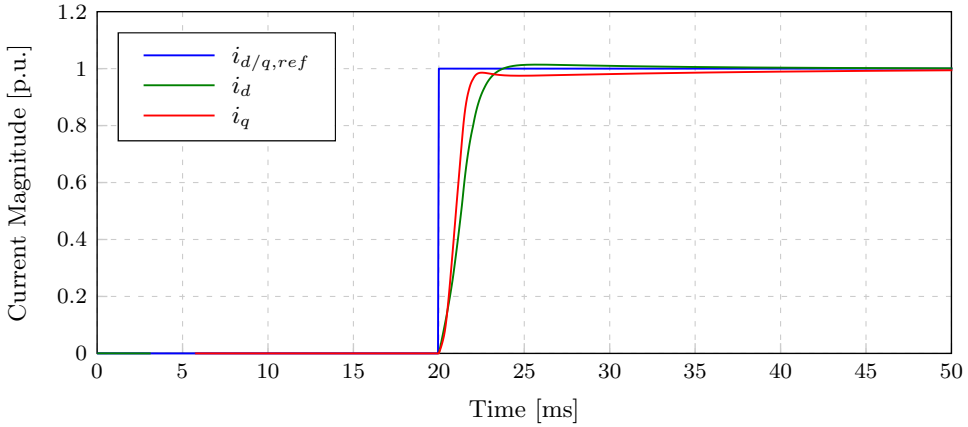

Figure 3.18: Simulation result for the rated-current control step at rated speed with speed-voltage compensation plotting reference and actual rotor currents versus time.

has quite a dramatic impact at speed when comparing the results of Figure 3.17 to the results shown in Figure 3.16. Note the large difference in the effect of the speed voltages on the d- and q-axis current controllers, owing to the fact that the d-axis flux is larger in magnitude at rated current angle above about 0.125 p.u. stator current (see (3.3.3), (3.3.4 and Figure 2.7). Compensating for these speed voltage terms leads to the result given in Figure 3.18. See how the speed voltage-compensated result of Figure 3.18 compares to the result at standstill in Figure 3.16. The speed voltage-compensated rated-current control step simulation result at rated speed in Figure 3.18 has d-axis and q-axis 2% settling times of 4.5 ms and 2.5 ms respectively.

In order to improve the current controller dynamics without speed voltage compensation the controller PI gains are adjusted. Figure 3.19 shows the adjusted gain rated-current control step at rated speed with no speed voltage compensation. At first glance it might seem that the current response is still too slow, but it can be determined that about 10 ms after the current step in the figure the torque produced by the machine is equal to 98% of its value at rated current. This result is accepted as sufficient for current control purposes, since the speed controller is designed to be much slower than that. Note however that during the current transient the current angle is not equal to the rated/selected value, since each current controller functions separately. Also, it can be considered as the worst case scenario since it is a full load step at rated speed.

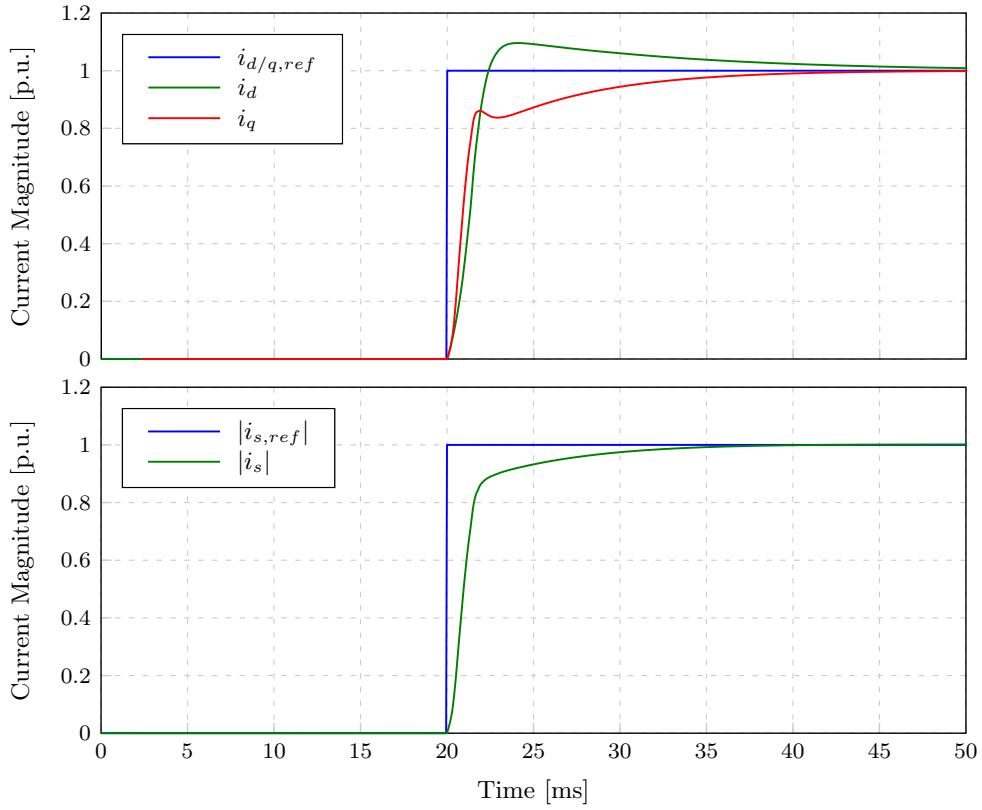

Figure 3.19: Final simulation result for the rated-current control step at rated speed without speed-voltage compensation plotting reference and actual currents versus time.

Table 3.2: Current control simulation variables

Variable	**Value**
K_{Pd}	300
K_{Pq}	250
K_{Id}	30000
K_{Iq}	37500
V_{DC}	608 V

The final current controller simulation variables are given in Table 3.2. The DC-bus voltage is taken as a rectified line voltage of $v_{ab} = 430$ V for the stator voltage magnitude limitation.

3.3.5 Practical Results

Practical measurements of the current controllers coincided relatively well with the simulated results, as will be shown here.

A standstill (locked-rotor) rated-current control step measurement is shown in Figure 3.20. It can be seen that the direct- and quadrature-axis current controllers behave very similarly to the simulated controllers when comparing to the results of Figure 3.16.

A rated current-control step measurement at rated-speed is shown in Figure 3.21. This result is without speed voltage compensation implemented. It can be seen that the

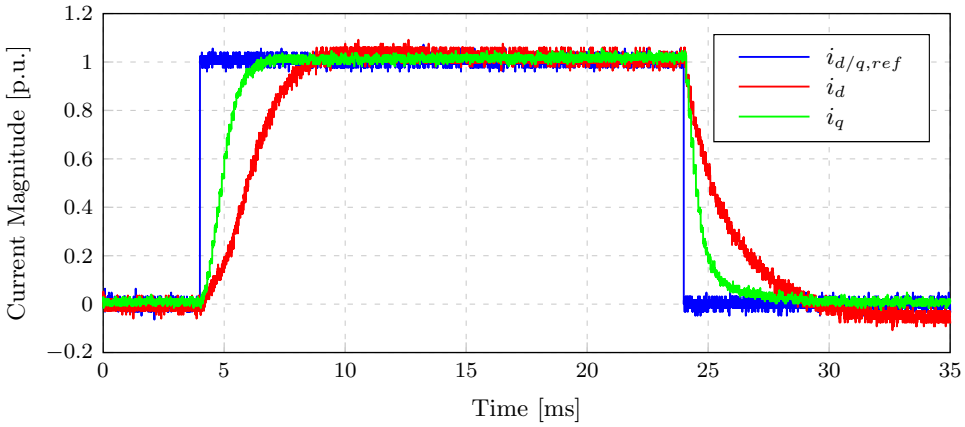

Figure 3.20: Measured results of the rated-current control step with locked-rotor without speed-voltage compensation plotting reference and actual d/q-currents versus time.

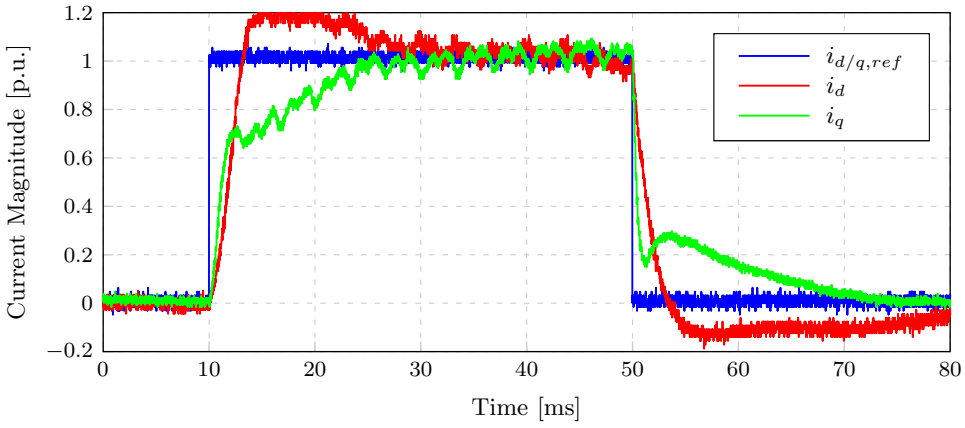

Figure 3.21: Measured results of the rated-current control step at rated speed without speed-voltage compensation plotting reference and actual d/q-currents versus time.

current controllers are still relatively fast and settle within about 10 ms. See the similarity with the simulated results of Figure 3.19.

Speed voltage compensation is implemented for the rated-current control step measurement at rated-speed shown in Figure 3.22. It can be seen that the initial over- and undershoot in the d- and q-axis current controllers are once again compensated quite well. Other than the simulated result this current control step at speed does not perfectly resemble the standstill result. This is attributed to a noisy resolver signal - since it cannot be perfectly aligned with the rotor shaft - as well as a filtered speed measurement.

3.4 Speed Control

With a completed current controller the machine torque can be accurately controlled with very fast dynamics allowing design of a speed controller. The electromechanical torque of the machine in (2.2.1) can be rewritten as a function of the stator current vector, $\boldsymbol{i}_s$, since the d/q-axes currents are controlled proportional to each other with constant current angle as in (3.3.21) and (3.3.22) so that

$$\tau_{em} = \frac{3}{4} p(L_d - L_q) \sin(2\gamma) |\boldsymbol{i}_s|^2. \tag{3.4.1}$$

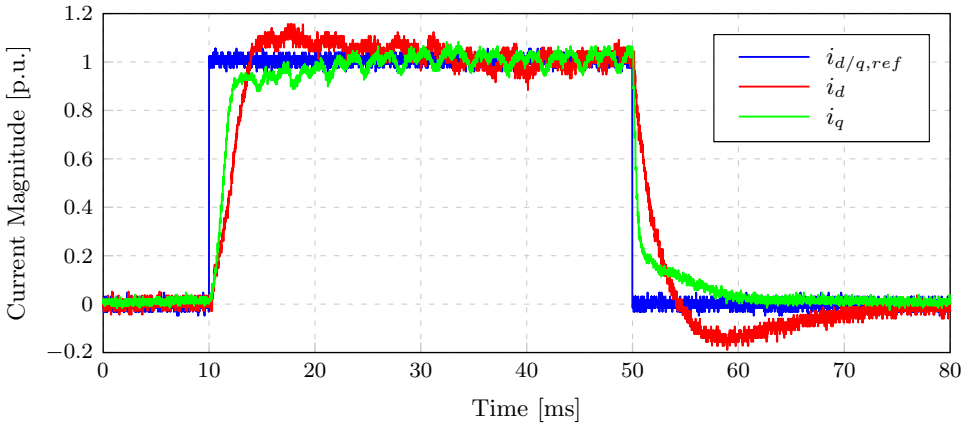

Figure 3.22: Measured result for the rated-current control step at rated speed with speed-voltage compensation plotting reference and actual d/q-currents versus time.

Since the inductances are functions of current (now taking into account cross saturation effects) as

$$L_{d/q} = f(i_d, i_q) = f(|\boldsymbol{i}_s| \cos\gamma, |\boldsymbol{i}_s| \sin\gamma) \tag{3.4.2}$$

and the current angle is kept constant the torque can be expressed in terms of a variable, K_τ, which is a function of the stator current magnitude as

$$K_\tau = \frac{3}{4} p(L_d - L_q) \sin(2\gamma) \tag{3.4.3}$$

$$= f(|\boldsymbol{i}_s|). \tag{3.4.4}$$

Subsequently the torque is expressed as

$$\tau_{em} = K_\tau |\boldsymbol{i}_s|^2. \tag{3.4.5}$$

The torque variable and electromechanical torque versus stator current magnitude (at rated current angle) for the machine is shown in Figure 3.23. Note from the torque variable plot how magnetic saturation plays a role in the produced torque of the machine at lower currents. Above the saturation point the plot resembles a quadratic shape with a negative slope which counteracts the quadratic nature of (3.4.5) so that the generated torque plot approaches a straight line.

Considering the preceding derivation and the mechanical system equation in (2.2.2) we can derive a transfer function for the system describing its motion characteristics. From Figure 3.10 it can be seen that the machine current follows a constant reference value within 2 ms so that for a much slower speed control loop the current model becomes

$$H(s) = \frac{\boldsymbol{i}_s^r}{\boldsymbol{i}_{s,ref}^r} \approx \frac{1}{1 + 0.002s} \approx 1, \tag{3.4.6}$$

and the torque model becomes (from Figure 3.23)

$$I(s) = \frac{\tau_{em}}{|\boldsymbol{i}_s|} \approx \frac{8.12}{5} = 1.624. \tag{3.4.7}$$

(3.4.7) approximates Figure 3.23 as a straight line to result in a very simple torque controller. The reference torque from the speed controller is therefore used as the reference value for the current controller to result in the cascaded control loop structure in Figure 3.24.

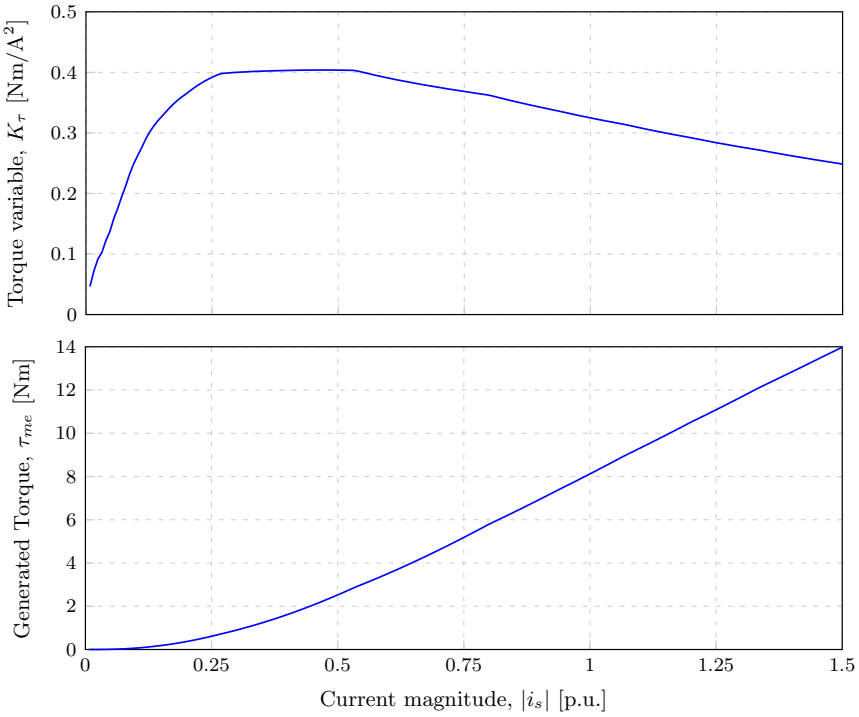

Figure 3.23: The calculated machine torque variable and generated torque versus current.

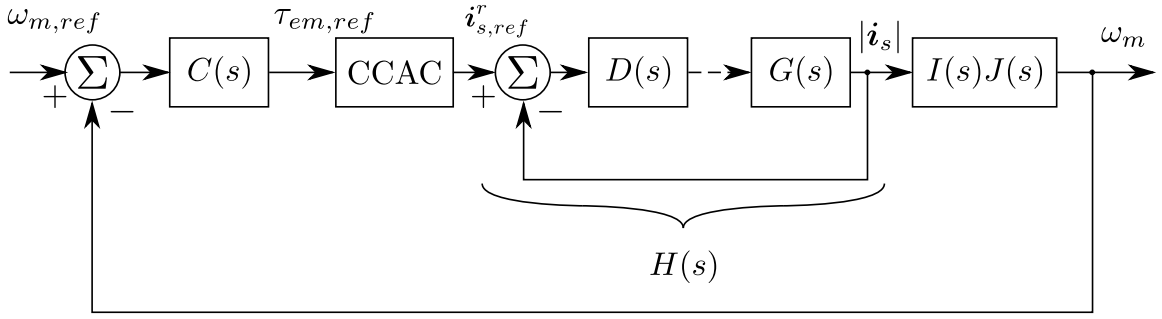

Figure 3.24: The cascaded speed controller block diagram containing the current controller with CCAC for MTPA.

3.4.1 Speed Controller

The mechanical speed versus torque model of the machine can be derived from (2.2.2) by considering the load torque, τ_L, as a disturbance signal so that

$$J(s) = \frac{\omega_m}{\tau} = \frac{1}{J_{eq}s + B_{eq}} \tag{3.4.8}$$

$$= \frac{1/B_{eq}}{1 + sT_{mech}}, \tag{3.4.9}$$

where $T_{mech} = \frac{J_{eq}}{B_{eq}}$ is the mechanical time constant. This continuous first order model multiplied by $I(s)$ is used to design a speed controller for the drive system without discrete compensation since the speed loop is chosen to be orders of magnitude slower than the switching time.

A PI controller is chosen for the speed control to result in a zero steady state error as

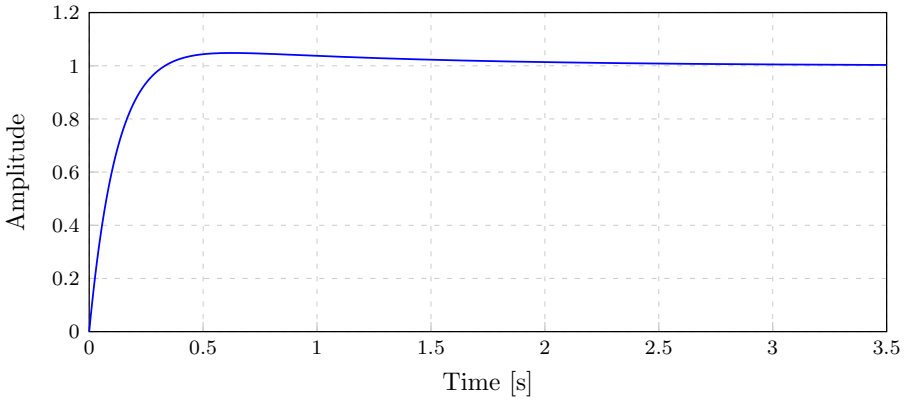

Figure 3.25: The closed-loop unit step response from the root locus plot.

with current control. The controller

$$C(s) = 0.02\frac{(s + 0.925)}{s} \tag{3.4.10}$$

results in the closed-loop unit step response in Figure 3.25 that has a 5% peak overshoot and a settling time of 1.63 s. Once again is should be noted that this step response is valid for the derived model. The chosen controller results in a proportional speed controller gain of $K_P = 0.02$ and an integrator gain of $K_I = 0.0185$ so that the closed-loop speed controller bandwidth is $\omega_{BW} = 9.46$ rad/s.

Anti-integration wind-up is implemented for the speed control loop by disabling the integrator when the controller output is higher than the current limit. This is important, because the speed loop is designed to be much slower than the current loop and switching cycle and the integration term is only required for a zero steady state speed error. The output magnitude of the controller is also limited to a chosen value so as to not exceed the current specifications of the stator windings.

3.4.2 Simulation Results

The simulation block diagram used is shown in Figure D.3. It shows the cascaded PI controller layout with the speed controller output being the current control loop input. The stator current magnitude is given in per unit scale where 1 p.u. equals rated current magnitude at rated current angle. Machine speed is given in per unit where 1 p.u. equals the rated machine speed. Throughout the speed control simulations no speed voltage compensation is done in the current control loop in order to showcase the relative speed of the current controller to the speed controller.

A no-load speed control simulation with controller gains as derived in this section is shown in Figure 3.26. It is evident that the dynamics do not exactly match that of the simplified model step response in Figure 3.25 with much more damped behaviour in the simulation result. Nonetheless, the step response has a 2% settling time of 1.46 s which is quite similar to the 1.63 s designed although the rise time is much longer. Note how the machine current seems to be equal to the reference value on this time scale so that the assumption made during the speed controller design is confirmed.

Adding a load disturbance to the speed control simulation resulted in unsatisfactory results with the controller gains used before. It was decided to move the zero position further away from the integrator while maintaining the same speed controller bandwidth. This resulted in a controller with satisfactory disturbance rejection and speed behaviour

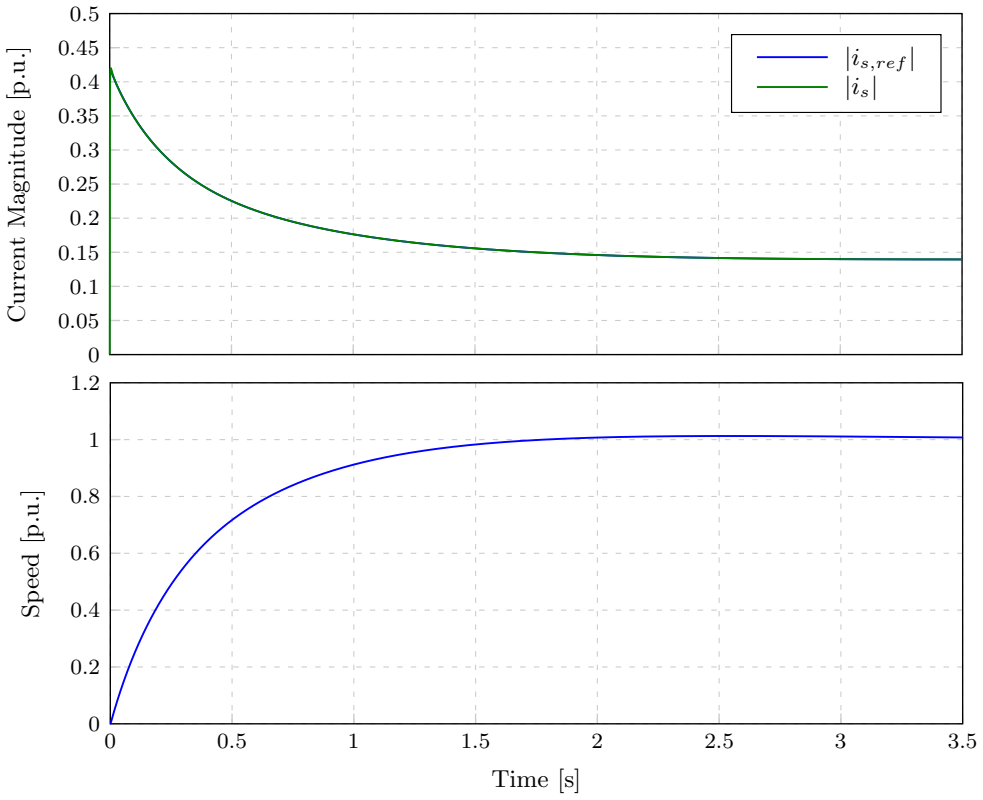

Figure 3.26: No-load standstill to rated speed control step response simulation result plotting machine current and mechanical speed versus time.

Table 3.3: Speed control simulation variables

Variable	**Value**
K_P	0.018
K_I	0.03726
n_m rated	1500 rpm
$\|\boldsymbol{i}_s\|$ rated	5 A
$\|\boldsymbol{i}_s\|$ limit	5.5 A

under load torque conditions. Figure 3.27 gives a speed control simulation result with a standstill to rated speed step at about rated load. The speed step response has a 2% settling time of 1.154 s. It can be seen that the machine is already under load when the reference speed step is given and the reference current hits the limit imposed in order to accelerate the machine.

Using the new speed controller gains a final no-load rated-speed control step simulation is done in order to show the implications of the new zero position. This simulation result is given in Figure 3.28 showing the speed overshoot because of a less-damped controller. The no-load speed step result has a 2% settling time of 2.3 s and a maximum overshoot of 10%. The final simulation variable values used in the simulations are given in Table 3.3. The stator current is limited to 110% of its rated value in order to allow acceleration under full-load conditions.

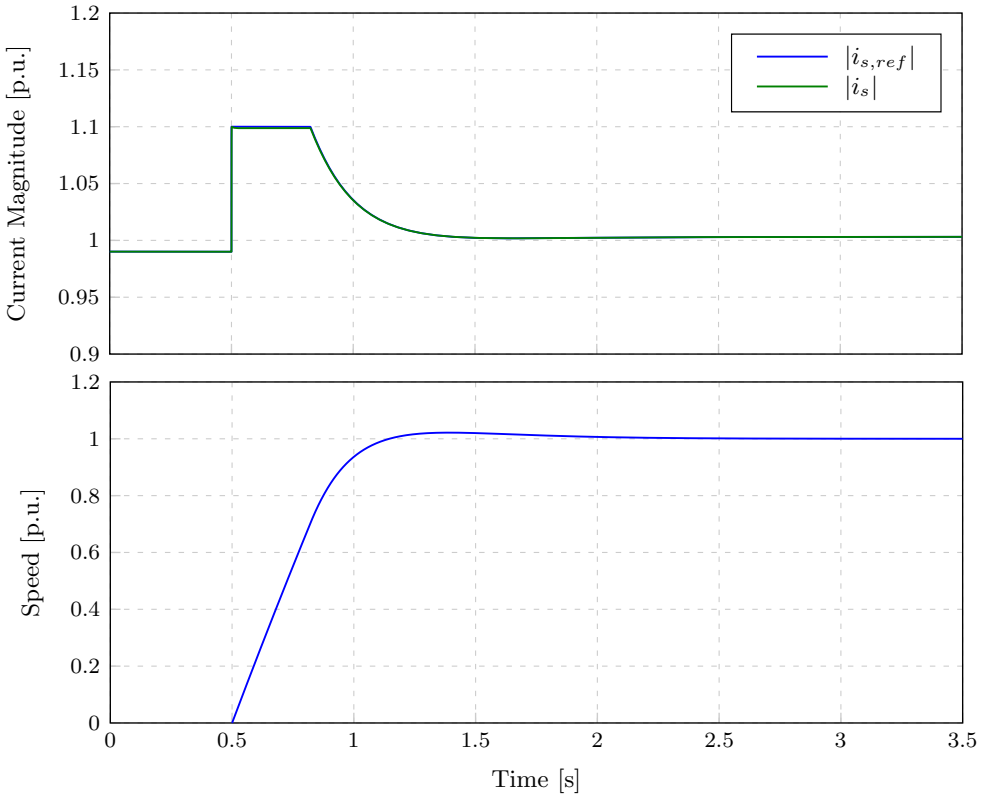

Figure 3.27: A full-load rated-speed step control simulation result plotting machine current and mechanical speed versus time.

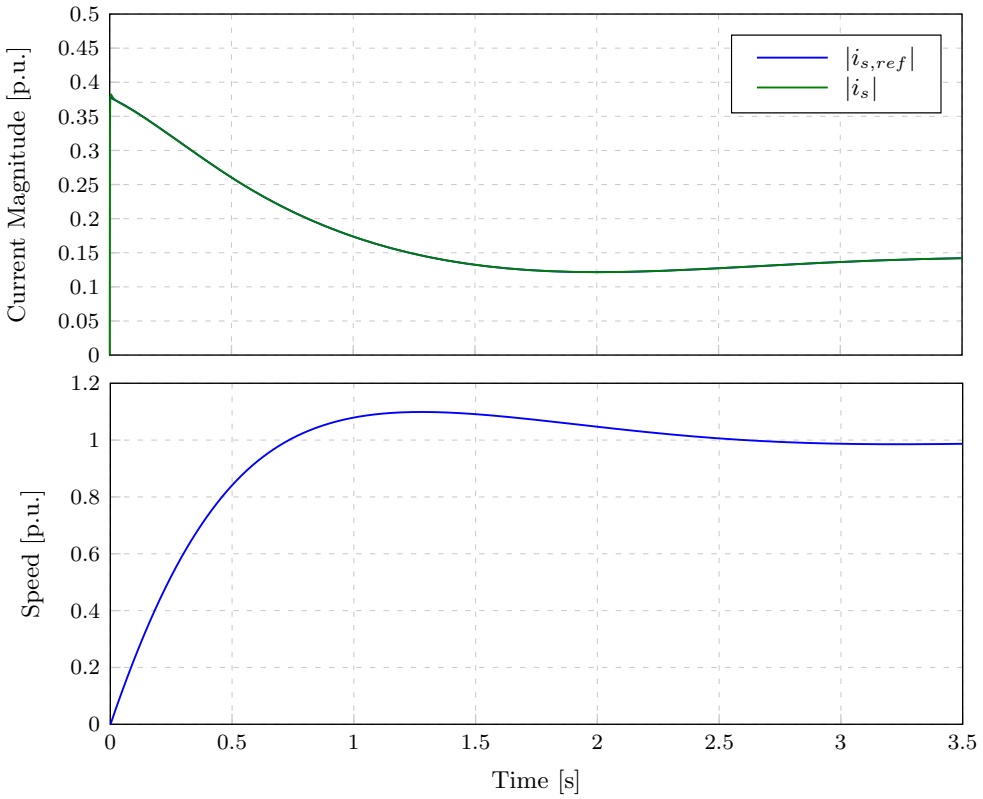

Figure 3.28: Final no-load rated-speed step control simulation result plotting machine current and mechanical speed versus time.

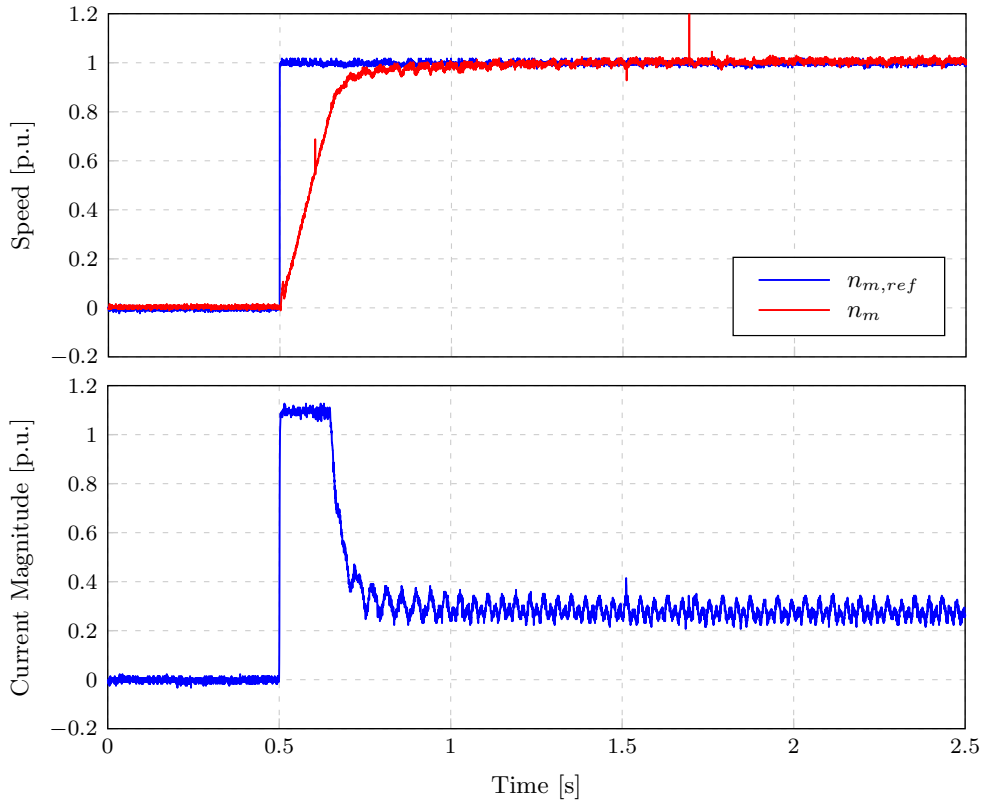

Figure 3.29: Measured no-load standstill to rated speed control step response result plotting mechanical speed and machine current versus time.

3.4.3 Practical Results

Practical measurements for the speed controllers differed a bit from the simulated values, and is attributed to differences in actual and theoretical friction and inertia values.

A no-load standstill to rated-speed control step measurement is shown in Figure 3.29. It can be seen that the speed response exhibits much more damped behaviour than that of the simulated response in Figure 3.28. This is most likely to be from a larger system wind and friction coefficient, B_{eq}, than estimated. Therefore the stator current magnitude settles at about 0.25 p.u. in the measured result compared to the simulation result of about 0.15 p.u. Subsequently it can be concluded that the system wind and friction is about 66.6% larger. Much higher current is also required to accelerate the system, attributed to an expected larger system inertia, as mentioned in section 2.3.

A full-load standstill to rated-speed control step measurement is shown in Figure 3.30. It can be seen that the machine accelerates much slower than simulated values, again attributed to the difference in system inertia. Nonetheless, fast and over-damped speed control with a 2% settling time of just over 1 s is achieved.

Figures 3.31 and 3.32 show standstill and rated-speed control measurements with large load torque steps applied. It can be seen that the speed controller has relatively good disturbance rejection. The slower speed recovery in the result of Figure 3.32 is because of the 1.1 p.u. current limit imposed.

These results are considered to be sufficient for the purposes of this research, since it is focused on position sensorless control of the RSM. It will be shown that in order to achieve stable sensorless control the dynamics of the speed controller had to be sacrificed and speed controller gains were lowered considerably.

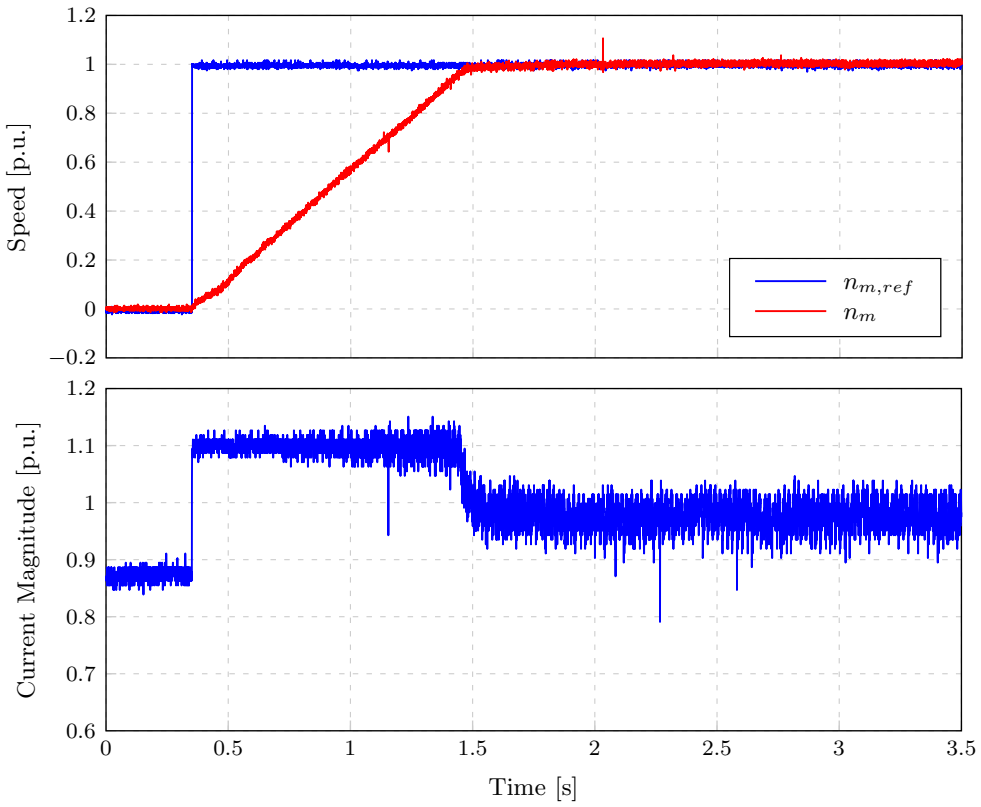

Figure 3.30: A measured full-load rated-speed step control result plotting mechanical speed and machine current versus time.

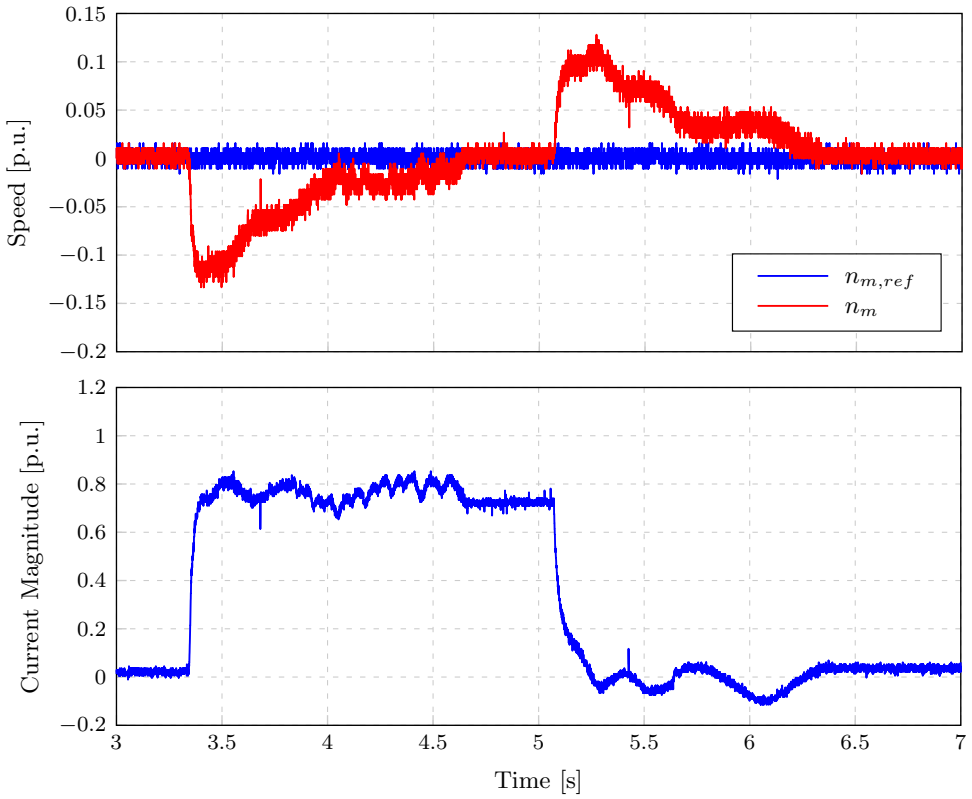

Figure 3.31: A measured load-step standstill speed control result plotting mechanical speed and machine current versus time.

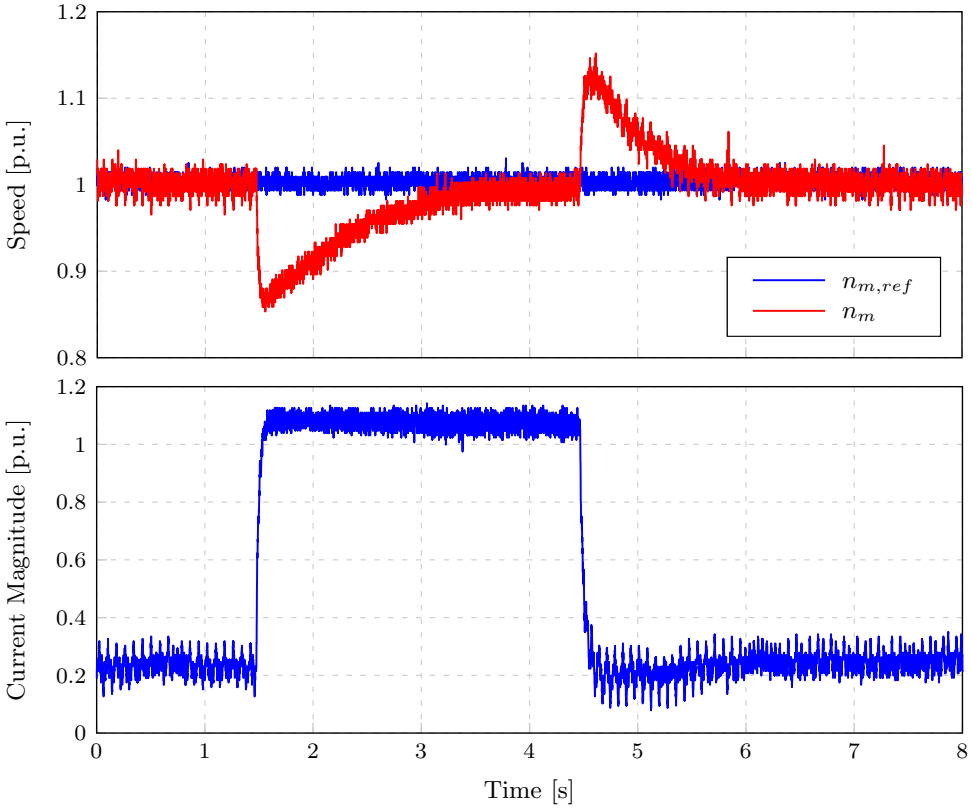

Figure 3.32: A measured load-step rated-speed control result plotting mechanical speed and machine current versus time.

Chapter 4

Active-Flux Position Estimation Method

This chapter contains the investigation into the active-flux position estimation method including the mathematical derivation, practical considerations for implementation on the investigated machine, simulation- and measured-results.

The active-flux (AF) position estimation method introduced in [19] is a fundamental model technique based on the stator voltage model of any AC machine. It aims to track the torque producing flux in the machine - which is aligned with the rotor axis in a predetermined way - to result in the rotor angle. Owing to it's model the AF estimation scheme has approximately the same structure for all AC machines. It has been investigated for DTC of an interior permanent magnet synchronous machine in [51].

In this research the AF estimation technique is investigated for position sensorless control of the transverse-laminated RSM for the first time to the authors knowledge, and implemented as part of the hybrid controller scheme derived in chapter 6.

4.1 Active flux vector

The electrical equation for torque in (2.2.1) can be rewritten as

$$\tau = \frac{3}{2} p \psi_d^a i_q, \tag{4.1.1}$$

where

$$\psi_d^a = (L_d - L_q) i_d \tag{4.1.2}$$

is the active flux vector also described as the torque producing flux for the RSM [30]. This vector is aligned with the rotor d-axis so that accurate estimation of it would result in knowledge of the rotor position. From (4.1.1) it is evident that the AF method turns the RSM (actually any AC machine) into a fictitious nonsalient-pole (isotropic) equivalent machine with saliency hidden in ψ_d^a.

Laplace transforming (2.1.9) and using the equation for the stator flux vector in rotor reference frame

$$\begin{aligned} \boldsymbol{\psi}_s^r &= \psi_d + j\psi_q \\ &= L_d i_d + j L_q i_q \end{aligned} \tag{4.1.3}$$

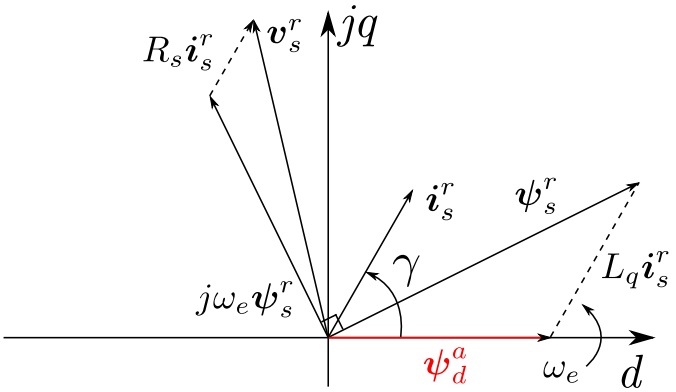

Figure 4.1: The steady state active flux vector diagram.

the stator voltage equation can be written as

$$\begin{aligned} \boldsymbol{v}_s^r &= R_s \boldsymbol{i}_s^r + s(L_d i_d + jL_q i_q) + j\omega_e(L_d i_d + jL_q i_q) \\ &= R_s \boldsymbol{i}_s^r + (s + j\omega_e)L_q \boldsymbol{i}_s^r + (s + j\omega_e)\boldsymbol{\psi}_d^a. \end{aligned} \tag{4.1.4}$$

Once again it is evident that (4.1.4) transforms the RSM into a nonsalient-pole equivalent machine [30].

The active-flux vector can be written in terms of the stator flux-linkage and current vectors from 4.1.2 as

$$\begin{aligned} \boldsymbol{\psi}_d^a &= (L_d - L_q)i_d + jL_q i_q - jL_q i_q \\ &= L_d i_d + jL_q i_q - L_q i_d - jL_q i_q \\ &= \boldsymbol{\psi}_s^r - L_q \boldsymbol{i}_s^r. \end{aligned} \tag{4.1.5}$$

This equation can be graphically understood by the steady state vector diagram shown in Figure 4.1 where the active flux vector is highlighted in red; see (2.1.9) considering that in steady state the change in rotor flux should be zero, therefore $\frac{d}{dt}\boldsymbol{\psi}_s^r \approx 0$. Note that the active-flux is a fraction of the total d-axis flux in the machine.

Solving for the stator flux vector from the stator voltage equation in (2.1.2) results in

$$\boldsymbol{\psi}_s^s = \int (\boldsymbol{v}_s^s - R_s \boldsymbol{i}_s^s).dt \tag{4.1.6}$$

which gives a starting point for determining the active-flux vector without knowledge of the electrical speed, ω_e. Integrator drift is caused by parameter estimation- and measurement errors as well as inverter non-linearities [52]. This is because a pure integrator has infinite gain at zero frequency so that any constant offsets in the input would cause a pure integrator to drift away beyond limits [52]. This drift is rectified for calculation of the stator flux vector with a compensation voltage, $\boldsymbol{v}_{comp}$, which is a function of the voltage-flux and current-flux models of the machine defined respectively as [30]

$$\boldsymbol{\psi}_s^{sv} = \int (\boldsymbol{v}_s^s - R_s \boldsymbol{i}_s^s + \boldsymbol{v}_{comp}).dt \tag{4.1.7}$$

and

$$\boldsymbol{\psi}_s^{si} = \mathbf{T}(L_d i_d + jL_q i_q) \tag{4.1.8}$$

$$= \mathbf{T}(\psi_d + j\psi_q). \tag{4.1.9}$$

By feeding the difference of the two models through a PI compensator as in (4.1.10) the estimated stator flux vector, $\hat{\boldsymbol{\psi}}_s^s = \boldsymbol{\psi}_s^{sv}$, is predominantly equal to the current-flux model at low frequencies and the voltage-flux model at higher frequencies [53]. This compensates for pure integrator offset and drift errors as well as stator resistance measurement errors [30].

$$\boldsymbol{v}_{comp} = (K_P + \frac{K_I}{s})(\boldsymbol{\psi}_s^{si} - \boldsymbol{\psi}_s^{sv}) \tag{4.1.10}$$

Solving for the estimated stator flux vector, $\hat{\boldsymbol{\psi}}_s^s$, from (4.1.7) and (4.1.10) results in

$$\hat{\boldsymbol{\psi}}_s^s = \frac{s}{s^2 + K_P s + K_I}(\boldsymbol{v}_s^s - R_s \boldsymbol{i}_s^s) + \frac{sK_P + K_I}{s^2 + K_P s + K_I}\boldsymbol{\psi}_s^{si}. \tag{4.1.11}$$

Evidently the voltage-flux and current-flux models are high-pass filtered and low-pass filtered respectively, at a cut-off frequency determined by the K_P and K_I gains [30].

The active flux observer in the stator reference frame is defined as [19]

$$\begin{aligned}
\hat{\boldsymbol{\psi}}_d^{as} &= \hat{\boldsymbol{\psi}}_s^s - L_q \boldsymbol{i}_s^s \\
&= \int (\boldsymbol{v}_s^s - R_s \boldsymbol{i}_s^s + \boldsymbol{v}_{comp}).dt - L_q \boldsymbol{i}_s^s && (4.1.12) \\
&= \psi_d^a \cos\theta_{\psi_d^a} + j\psi_d^a \sin\theta_{\psi_d^a}. && (4.1.13)
\end{aligned}$$

In effect then (4.1.12) is basically a voltage model with some compensation required at low speeds [19].

Since the AF vector is defined to be aligned to the d-axis of the rotor the estimated rotor angle can be calculated directly from (4.1.12) using trigonometry. The angle of the vector is equal to the estimated rotor angle as

$$\hat{\theta}_e = \theta_{\hat{\psi}_d^{as}} = \arctan \frac{\hat{\psi}_{d\beta}^a}{\hat{\psi}_{d\alpha}^a}. \tag{4.1.14}$$

During testing it was found that the directly calculated angle could not be used for closed loop control of the machine and consequently a phase-locked loop (PLL) approach is taken - as explained in Appendix C from [14] - to estimate the electrical rotor angle from the estimated AF vector.

4.2 Phase-Locked Loop Angle

The error signal in (4.2.1) from [30] is equal to zero when the output angle of the PLL, $\hat{\theta}_e$, is equal to the estimated AF angle, $\hat{\theta}_{\psi_d^{as}}$, as is evident from (4.2.3). This approach results in the estimated electrical rotor angle and angular velocity from the PLL scheme in Figure 4.2.

$$\begin{aligned}
K \sin\tilde{\theta}_e &= \psi_{d\beta}^a \cos\hat{\theta}_e - \psi_{d\alpha}^a \sin\hat{\theta}_e && (4.2.1) \\
&= |\hat{\boldsymbol{\psi}}_d^{as}|(\sin\theta_{\hat{\psi}_d^{as}} \cos\hat{\theta}_e - \cos\theta_{\hat{\psi}_d^{as}} \sin\hat{\theta}_e) && (4.2.2) \\
&= |\hat{\boldsymbol{\psi}}_d^{as}| \sin(\theta_{\hat{\psi}_d^{as}} - \hat{\theta}_e) && (4.2.3)
\end{aligned}$$

Using a PLL angle observer has some advantages compared to direct angle calculation as listed:

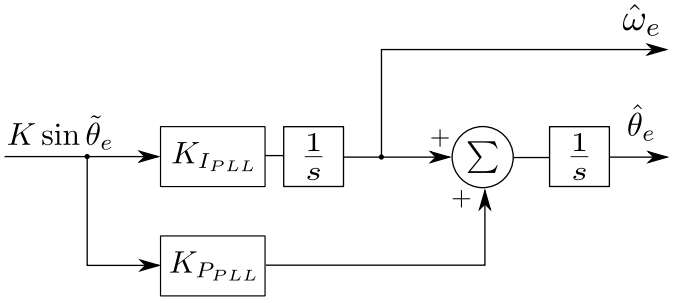

Figure 4.2: The PLL observer scheme with error signal input and estimation output.

- Stability and disturbance rejection.
- Cleaner, filtered output.
- Can be synchronised with other estimation techniques.

The main drawback when using a PLL angle for the AF estimator is the initial synchronisation time which could amount more than 100 ms. This is problematic, because during the initial stages of this synchronisation the error angle is very large and could result in unstable control when it is used for control. This is one of the central design problems faced in this project.

In [30] a mechanical parameter based PLL is implemented in order to achieve better dynamics during speed transients with the AF estimator as fast speed changes causes the simple PLL scheme angle to drift away with small gains whereas high gains cause control instability. The drawback of this approach is the dependency on knowledge of the system mechanical parameters so that it was decided to not implement such a scheme and investigate the feasibility thereof.

Considering the derivation in Appendix C from the general algorithm for speed and position estimation of AC machines in [14] the PLL gains can be chosen as

$$K_{P_{PLL}} = \frac{2\rho}{|\hat{\boldsymbol{\psi}}_d^{as}|} \tag{4.2.4}$$

$$K_{I_{PLL}} = \frac{\rho^2}{|\hat{\boldsymbol{\psi}}_d^{as}|}, \tag{4.2.5}$$

where both poles are placed at $s = -\rho$ to ensure stability at constant speed. The pole position ρ is chosen as

$$\rho = \sqrt{\frac{\omega_{BW} \Delta\omega_{e,ref}}{\sin \tilde{\theta}_{e,max}}} \tag{4.2.6}$$

where ω_{BW} is the speed control loop bandwidth, $\Delta\omega_{e,ref}$ is the speed reference step size, and $\theta_{e,max}$ is the maximum allowed transient position estimation error [14]. Selecting the maximum transient position error as a relatively low value, say 10°, should eliminate the likelihood of the PLL being pulled out of phase [14]. It should be noted that increasing ρ directly increases noise in the speed estimate as shown in [14], consequently the estimator should not be made faster than necessary.

4.3 Considerations for implementation

In [30] the author recommends to apply a constant d-axis current in the machine and to control torque and speed using the q-axis current. This results in a overwhelmingly constant (varies slightly in the case of cross-magnetization) full-load d-axis flux-linkage in the machine in the entire load range. As mentioned in section 3.3 this method is known as CFCC, which is less efficient (especially at low loads). In this project CCAC is implemented which results in variable d- and q-axis currents and close to the highest efficiency for a RSM. A variable current implies that the flux-linkage in the machine is also not constant and therefore the AF in the machine would vary. This fact distinguishes this research from that presented in [30] in terms of the AF estimation technique implemented for a RSM.

4.3.1 d-axis saturation

Since the AF method tracks the virtual torque-producing flux-linkage in the d-axis, at least some d-axis current is required for the RSM as is evident from Figure 2.7. It is chosen to insert at least 1 A d-axis current when implementing the AF method, since this is equal to 0.4 p.u. d-axis current at the rated current angle which would result to about 50% of the full-load flux-linkage to be present. A lower value would result in higher efficiency at lower loads, but constitutes a much larger estimation error for the AF method. Therefore at and above 0.4 p.u. current reference the stator current would be at rated current angle.

4.3.2 Variable inductance

The author in [30] proposes using a constant value for the q-axis linearised inductance used in the AF scheme, since it is relatively constant for the ALA-rotor RSM used therein. From Figure 2.8b it is evident that the linearised inductance is notably variable and cannot be used as a constant. Since the flux-linkage levels are required for the current-flux model in the compensation voltage of the AF scheme as in (4.1.9), it is determined using a LUT of the flux maps in Figure 2.6. The determined q-axis flux-linkage value is then multiplied by the q-axis current to result in the linearised inductance at that working point.

4.3.3 Voltage saturation

The stator voltages are not measured practically (as is common practice in industry) and consequently the reference stator voltage vector, $\boldsymbol{v}_s^s$, is used in the AF scheme. This reference voltage vector is the value given to the SVPWM function to result in the inverter switching cycles. It gives satisfactory results even though the applied voltage lags the reference voltage as in 3.3.9. A crucial implication of this implementation is that when the reference voltage exceeds the limits of the SVPWM function the applied voltage is limited and the AF scheme would make very large estimation errors. Therefore for this control scheme the voltage should be kept within the linear region of the SVPWM function when operating in sensorless control mode.

4.3.4 PLL gain selection

Initial gains for the PLL are taken as in (4.2.4) and (4.2.5) by selecting the terms as the drive control system parameters. With a speed controller bandwidth of $\omega_{BW} = 9.46$ rad/s, a maximum reference speed step of zero to rated speed $\Delta\omega_{e,ref} = 1500$ rpm, a maximum transient position estimation error of $\tilde{\theta}_{e,max} = 10°$, and rated d-axis flux-linkage from Figure 2.7 as $|\boldsymbol{\psi}_d^{as}| \approx 1$ Wb-turns the PLL gains result to

$$K_{P_{PLL}} = 185, \tag{4.3.1}$$
$$K_{I_{PLL}} = 8557. \tag{4.3.2}$$

These values are used in simulation and are tuned when the AF method is implemented practically for ideal tracking.

4.3.5 Compensation voltage

The compensation voltage PI gains are chosen in such a way that the resulting filter transfer functions in (4.1.11) have poles at the same location (with the same filter frequency). As shown in [53] the coefficients can be chosen as

$$K_P = \omega_1 + \omega_2 \tag{4.3.3}$$
$$K_I = \omega_1 \times \omega_2, \tag{4.3.4}$$

where ω_1 and ω_2 are the closed-loop poles of the flux estimator. These poles are chosen as 8 and 10 to result in v_{comp} PI gains of

$$K_P = 18 \tag{4.3.5}$$
$$K_I = 80 \tag{4.3.6}$$

which results in a stator flux estimation which is predominantly equal to the current-flux model, ψ_s^{si}, below and to the voltage-flux model, ψ_s^{sv}, above about 10 rad/s. This electrical frequency relates to a mechanical rotor speed of the voltage-flux and current-flux model filter bode plots are shown in Figures 4.3a and 4.3b respectively.

The complete AF position estimation scheme in block diagram format is shown in Figure 4.4. The figure shows the current-flux model LUT block and the PLL block which is shown in Figure 4.2.

4.4 Simulation Results

Before practical implementation the AF method is tested using the Simulink model derived in section 2.4 since it contains a very accurate representation of the flux-linkage present in the machine. The simulation block diagram for the AF estimation scheme is shown in Figure 4.5 representing Figure 4.4 without the PLL and estimated angle output. It contains among others the current-flux model in the form of a flux-linkage LUT, the compensation voltage PI block, and the PLL error calculation block representing (4.2.1). The PLL error calculation block is shown in Figure 4.6 being the block diagram equivalent of (4.2.1).

The complete AF based PSC simulation block diagram for speed control of the RSM is shown in Appendix D in Figure D.4. It implements the AF estimation block in Figure 4.5

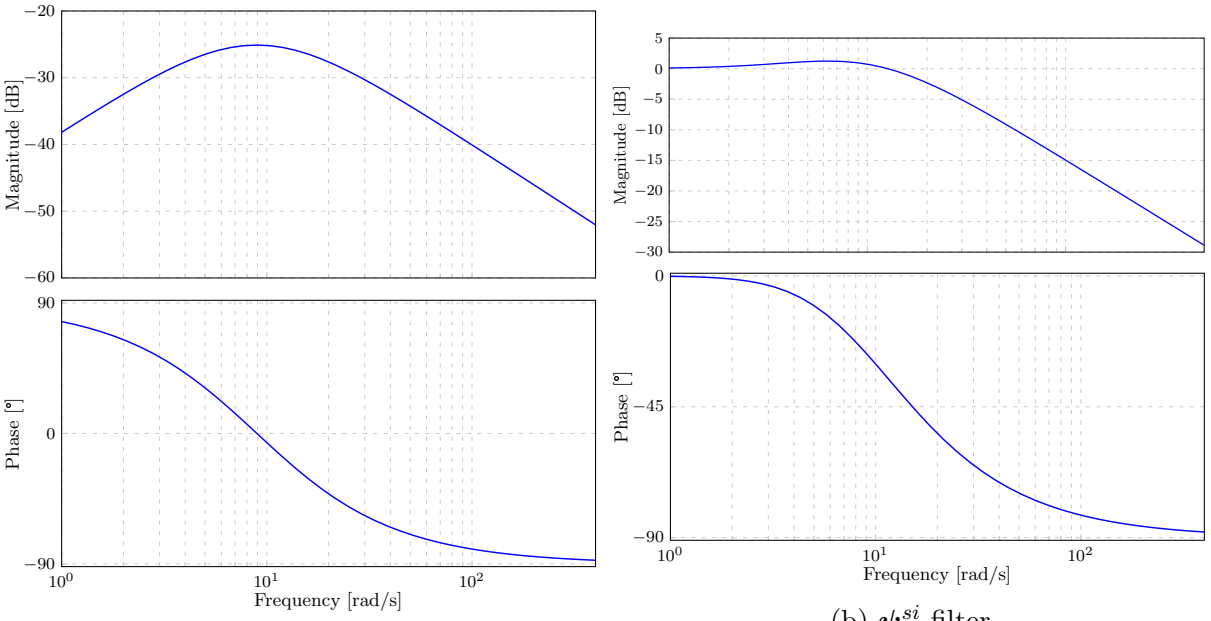

(a) $\boldsymbol{\psi}_s^{sv}$ filter

(b) $\boldsymbol{\psi}_s^{si}$ filter

Figure 4.3: The voltage-flux and current-flux estimation model filter bode plots.

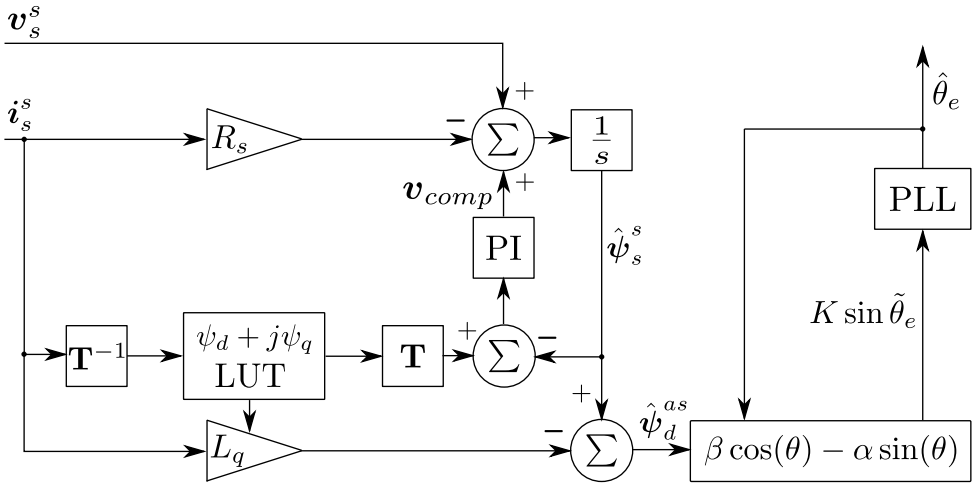

Figure 4.4: The AF position estimation scheme block diagram.

with its output error input to a PLL block with the layout given in Figure 4.2. The stator voltage vector, $\boldsymbol{v}_s^s$, is taken before the vector limit block since that is the value available in the practical setup as mentioned earlier.

It was found that under simulation conditions the AF estimation technique works very well, and that no compensation voltage, $\boldsymbol{v}_{comp}$, is even required since there are no measurement errors or noise disturbances and the stator resistance is simply a set variable value. Subsequently pure integration can be done to result in the estimated stator flux-linkage vector, $\hat{\boldsymbol{\psi}}_s^s$. The PLL gains and current saturation values were used as determined theoretically.

A sensorless current control step simulation from zero to rated current at rated-speed is shown in Figure 4.7. Since the flux-linkage LUTs are implemented as part of the AF estimation it was decided to implement speed-voltage compensation for current control since it would not constitute additional computation. It can be seen from the simulation

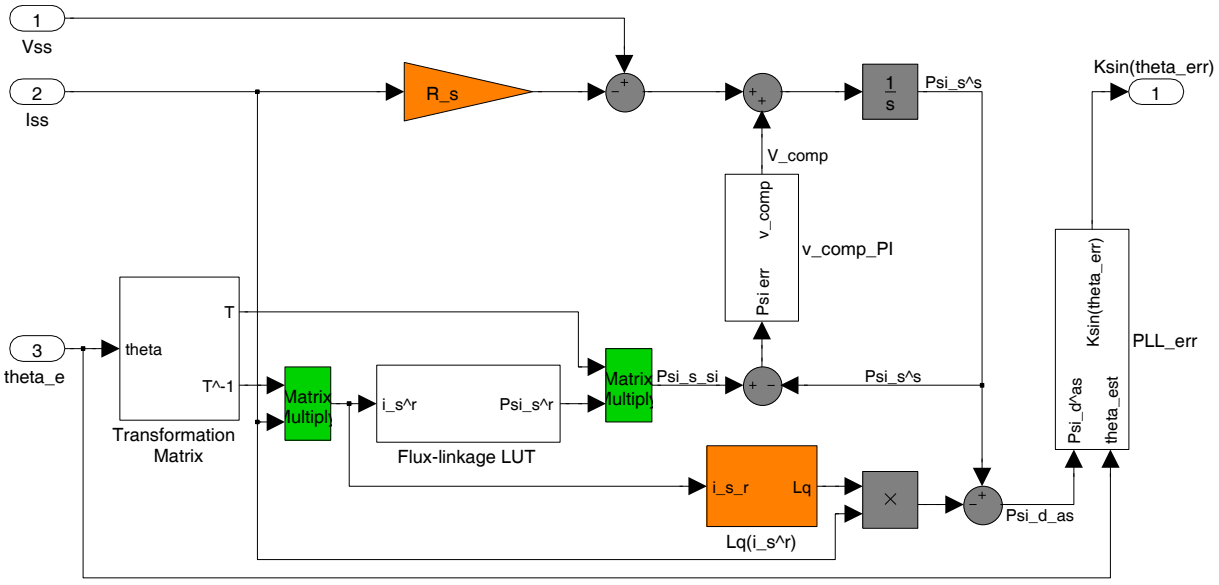

Figure 4.5: The AF estimation scheme simulation block diagram.

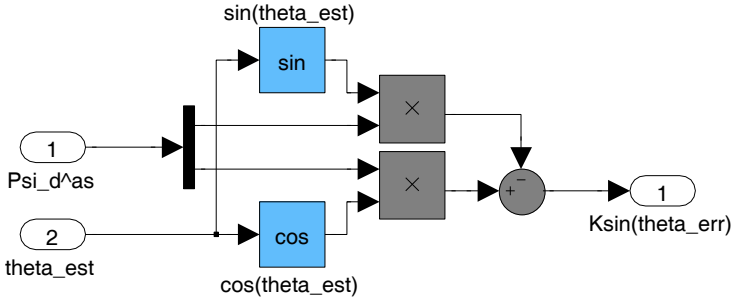

Figure 4.6: The AF PLL error calculation scheme simulation block diagram.

result that the current control is stable and settles to 2% of its final value within 5 ms. Note that before the reference current step the actual machine current is above the reference value since the minimum amount of d-axis current is being maintained ($i_d = 1$ A). The estimated electrical angle is also plotted over the actual angle to show that the position is estimated without error.

Figure 4.8 shows a sensorless low- to rated-speed control step simulation under full-load conditions. From the figure it can be seen that the speed transient creates a speed and position estimation error worth noting. Note once again that the current is limited to 110% of its rated value. The speed control is still stable and very fast, settling in about 0.5 s.

It is evident from these results that estimation using the AF method seems very accurate and reliable, without a position error in any load condition or at low speeds. It will be shown that practically the estimation error is indeed very much dependent on current and speed and has to be compensated to allow sensorless control.

4.5 Practical Results

The active-flux method is implemented on the drive system to validate the estimation technique for sensorless control of the RSM. Initially the PLL and compensation voltage PI gains had to be tuned in order to achieve accurate position observation.

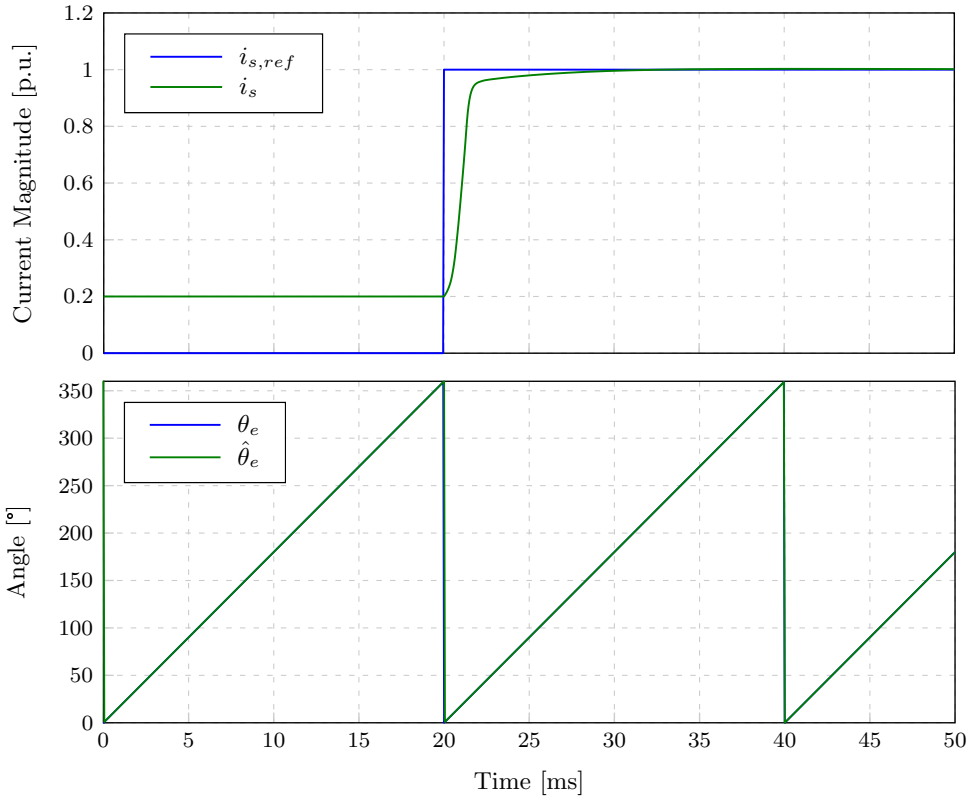

Figure 4.7: A sensorless rated-current control step simulation at rated-speed using the active-flux method plotting stator current and electrical angle versus time.

4.5.1 Compensation voltage

Practical implementation of the AF method resulted in a less than ideal amount of tuning and model-compensation in order to allow stable closed-loop sensorless control of the RSM. This is attributed mainly to the compensation voltage and PLL gain selections, with results differing quite drastically to theoretical and simulated values for negative current (generator action).

Measuring the estimation error of the AF estimator using the direct-angle or PLL-angle resulted in a current- and speed dependent error-map as given in Figure 4.9. It is evident from the map that the estimation error increases (or decreases for positive current) with current magnitude up to 0.4 p.u. where rated current angle is reached. Thereafter the error decreases slightly up to rated current, but is much more predictable. This phenomenon is attributed to the fact that as the ratio of q- versus d-axis current is increased up to the rated current angle (see subsection 4.3.1) the subsequent ratio of d- versus q-axis flux-linkage decreases, causing the active-flux to be less 'visible'. It can also be seen that with positive current the estimation error decreases linearly with a decease in speed, confirming that the voltage-flux and current-flux models function appropriately. Under negative-current conditions the estimation error increases exponentially as speed decreases and it was found that even with compensation of this error the estimated angle could not be used for closed-loop sensorless control.

Under inspection it was found that the estimated stator flux-linkage vector, $\hat{\boldsymbol{\psi}}_s^s$, moves away from the current-dependent flux-linkage-LUT vector, $\boldsymbol{\psi}_s^{si}$, under negative current conditions as shown in Figure 4.10.

It was determined that in order to mitigate the negative effects of a speed decrease under generator action and allow position sensorless control in the entire speed and current

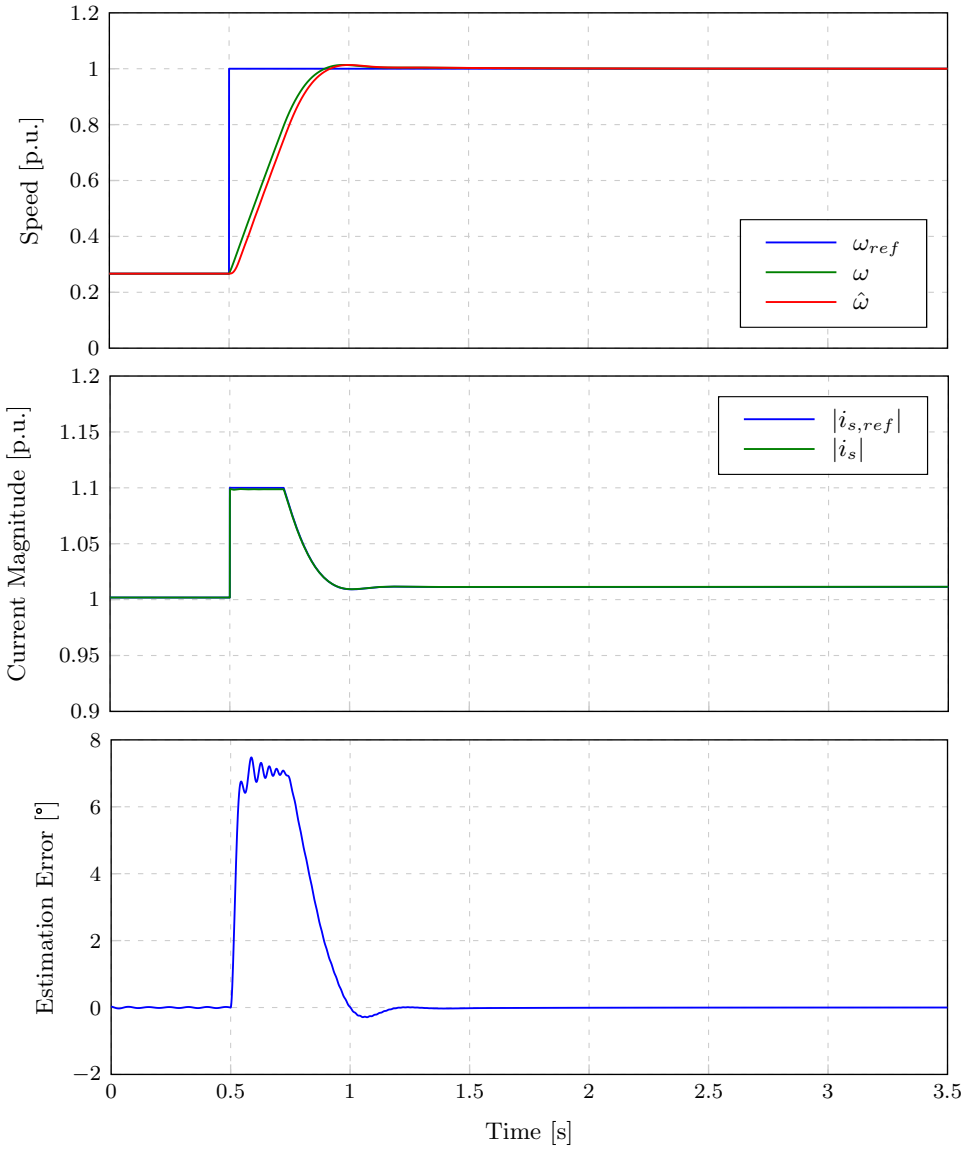

Figure 4.8: A rated load sensorless speed control step simulation from medium to rated-speed using the active-flux method plotting machine speed, stator current and estimation error versus time.

range the compensation voltage had to be adapted. The first passage of thought was to change the PI gains in order to result in a different changeover frequency for the voltage-flux and current-flux models, but it was found that this immediately made the PLL unstable. Finally the compensation voltage was changed by drastically reducing only the effects of the current-flux model. This was done by multiplying the current-flux model in (4.1.10) with a gain, KG_i, in order to result in a current-flux filter function (see (4.1.11)) of

$$G_i = \frac{KG_i(sK_P + K_I)}{s^2 + K_P s + K_I}. \tag{4.5.1}$$

This gain was chosen as $KG_i = 0.3$ which results in a current-flux filter bode plot as shown in Figure 4.11. Evidently the flux estimation is about 10 dB less equal to the current-flux model compared to Figure 4.3b. With this compensation the estimated stator flux-linkage vector and the current-dependent flux-linkage-LUT vector follow is each more closely as shown in Figure 4.12

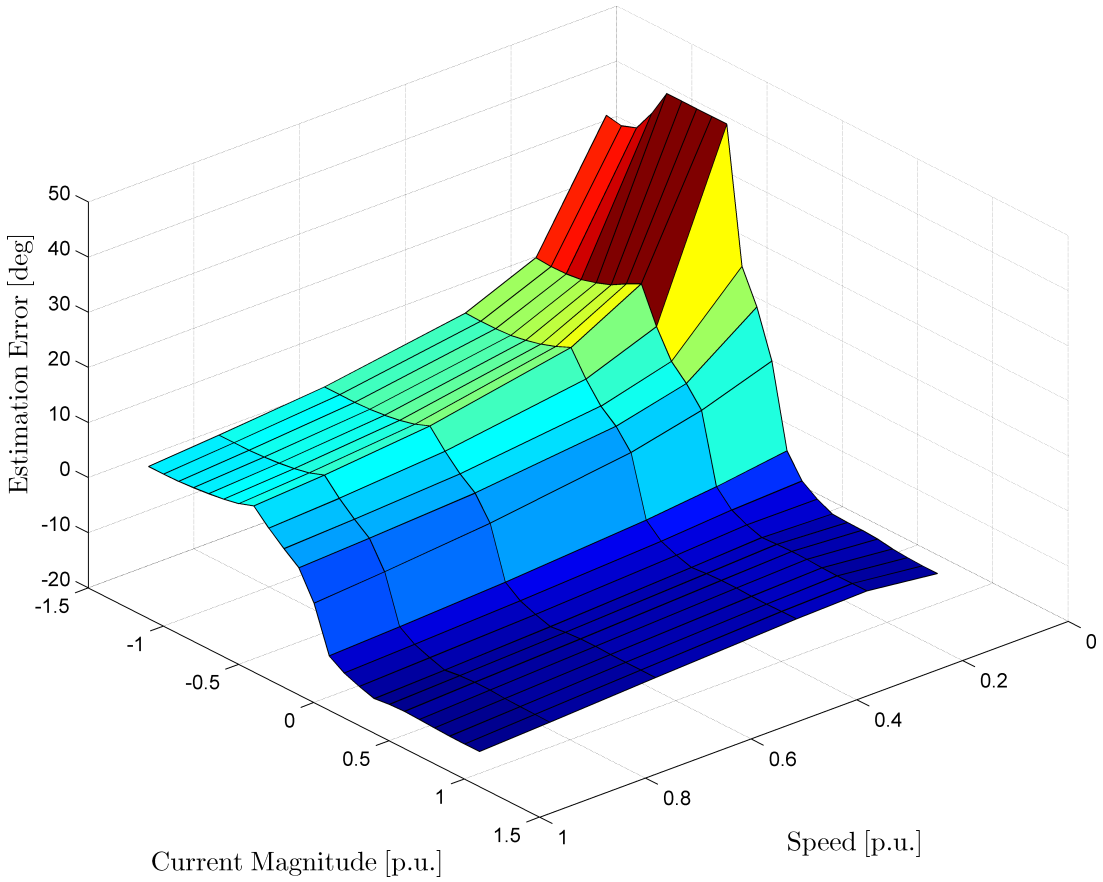

Figure 4.9: The measured active-flux estimation error plotting estimation error versus current and mechanical speed.

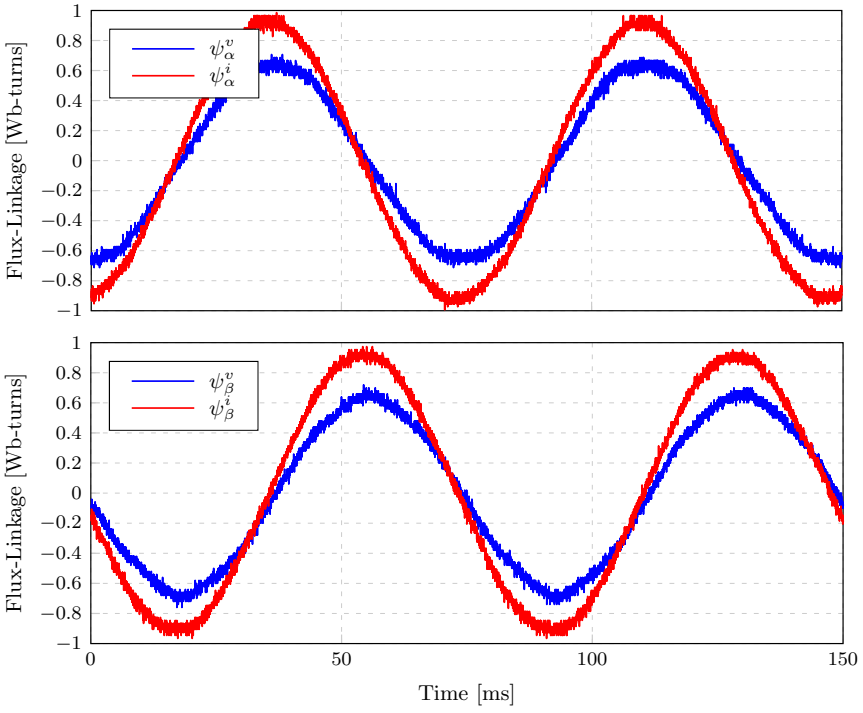

Figure 4.10: The measured active-flux estimated flux-linkage vector in α- and β-components respectively.

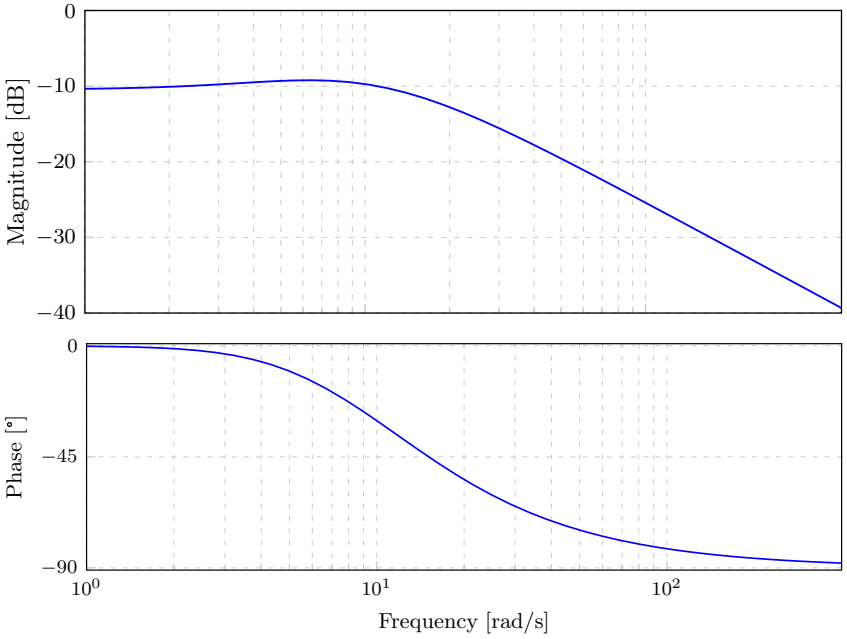

Figure 4.11: The gain-compensated active-flux stator flux estimation current-flux model filter bode plot.

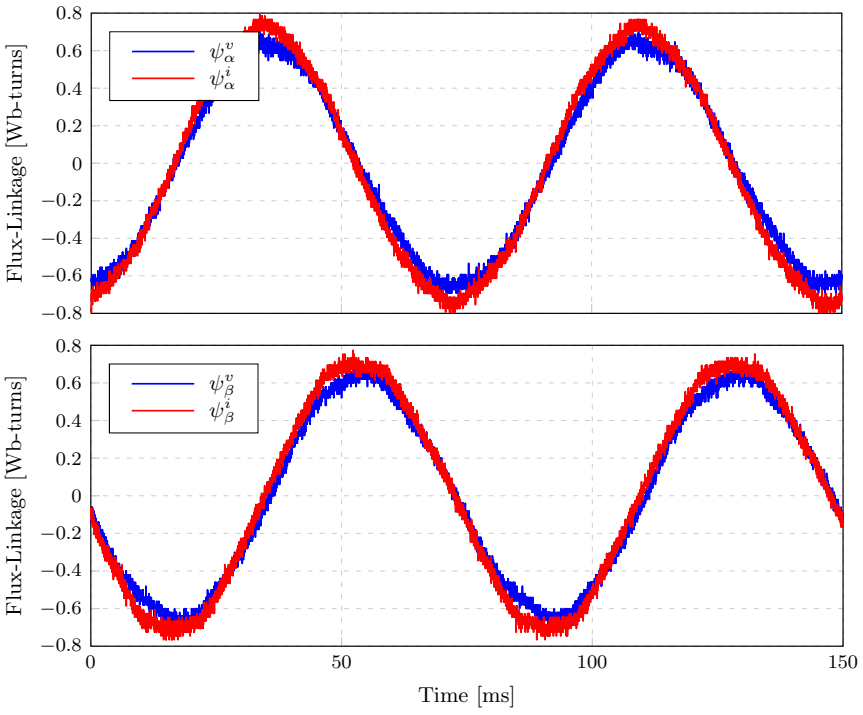

Figure 4.12: The measured compensated active-flux estimated flux-linkage vector in α- and β-components respectively.

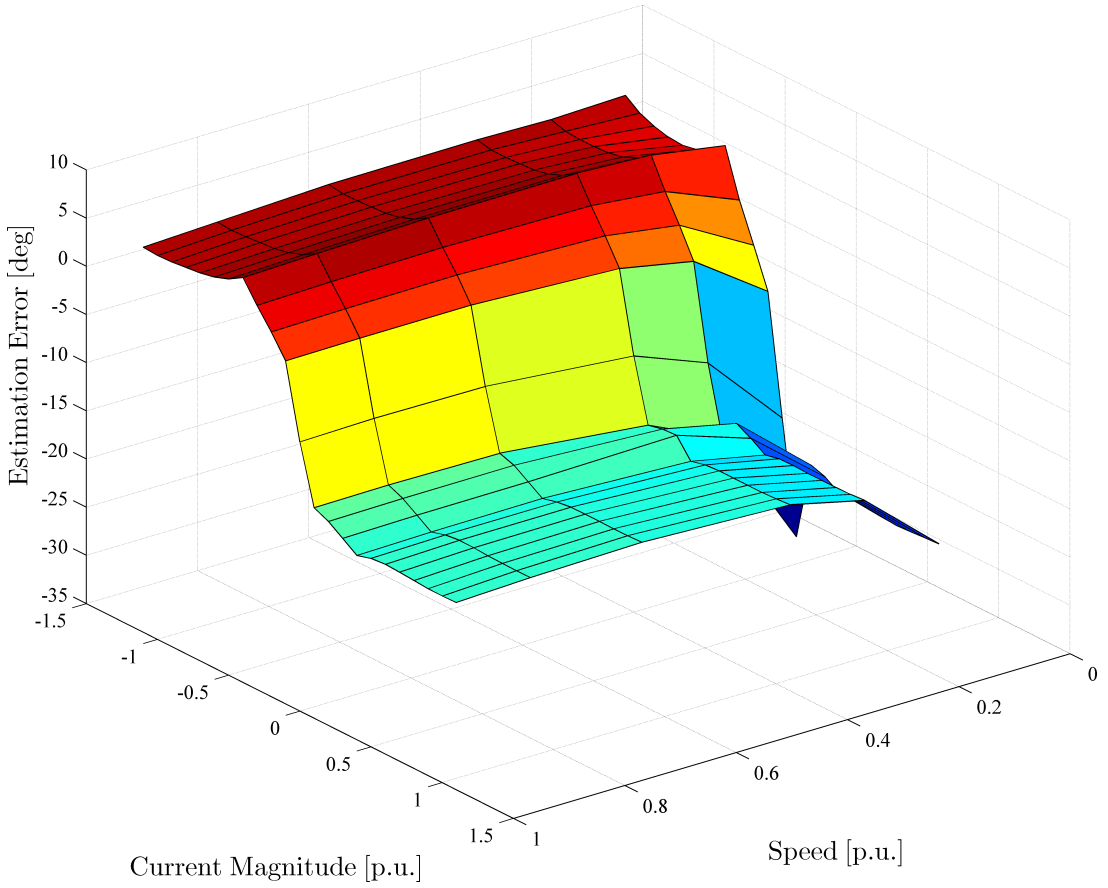

Figure 4.13: The measured compensated active-flux estimation error plotting estimation error versus current and mechanical speed.

The resulting estimation error map with this compensation voltage is shown in Figure 4.13. It can be seen that in this case the estimation error is more predictable for a change in speed in the negative current region, but that with positive current the error magnitude increases drastically. With this in mind a combined compensation voltage is implemented with the changed current-flux model gain for negative current and standard gains for positive current resulting in the error maps shown in Figure 4.14.

4.5.2 Error compensation

For closed-loop sensorless control using the AF method the estimated error has to be compensated using a pre-determined error function which can be extracted from the estimation error maps in Figure 4.14.

It was found that in the positive current region a current and speed dependent compensation had to be implemented for stable sensorless control with good dynamics. The estimation error as a function of positive current for the AF method is shown in Figure 4.15. As mentioned earlier the estimation error increases quickly up to the point where constant current angle control is implemented (0.4 p.u.) after which the error stays relatively constant. A 4th degree compensation curve for the error below the d-axis current 'saturation' point is then curve fitted as shown in Figure 4.16a and above the saturation point as shown in Figure 4.16b. Subsequently a speed dependent curve was determined by subtracting the combined current compensation curve from the positive current error map to result in an average error that is compensated using a 4th degree

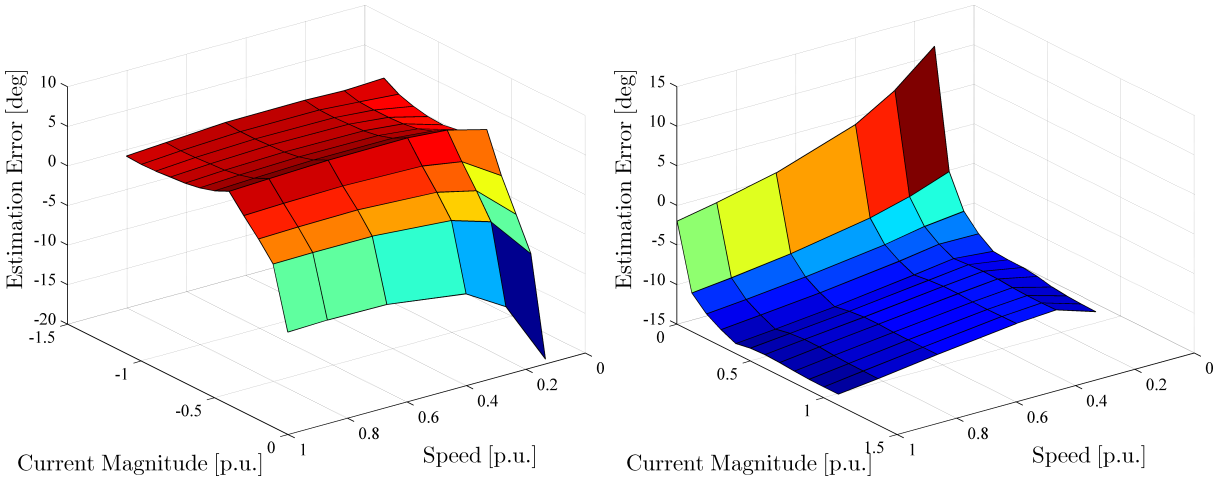

(a) Negative current error (b) Positive current error

Figure 4.14: The combined active-flux estimation error map.

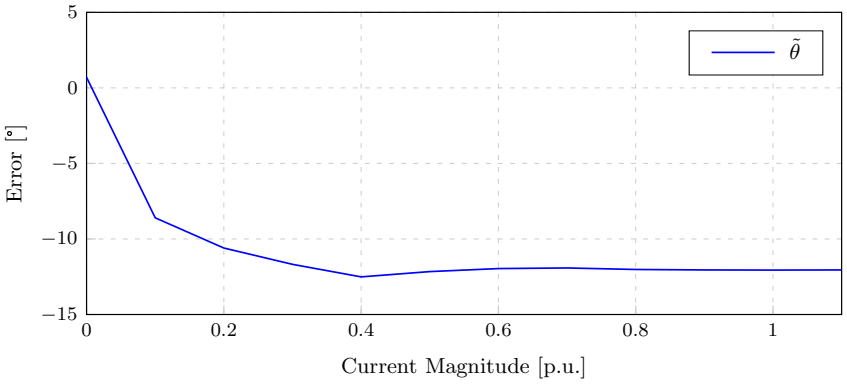

Figure 4.15: The estimation error curve for the active-flux method with positive current.

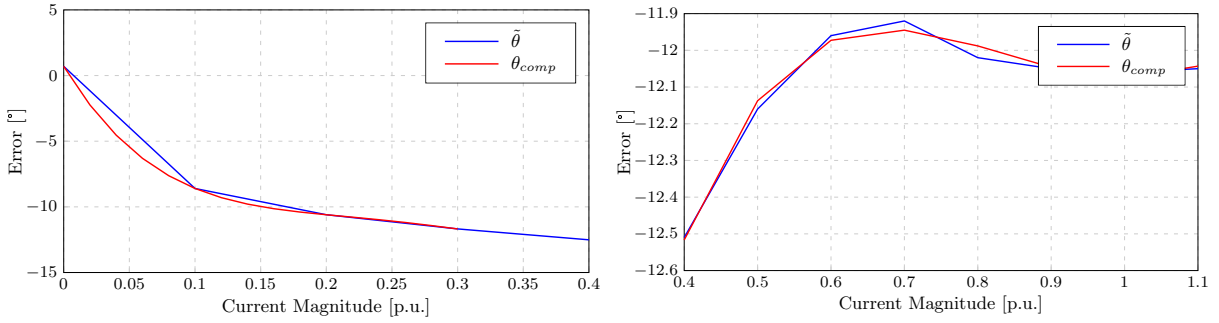

(a) Unsaturated positive current compensation (b) Saturated positive current compensation

Figure 4.16: The active-flux method compensation curves for positive current.

polynomial as shown in Figure 4.17.

Under negative current the AF estimation error looks similar to that of the positive current and is shown for under- and over-saturated currents in Figure 4.18. It was found that speed compensation was not necessary for the AF method under negative current conditions, because of a very fast PLL in that case, as will be discussed later.

When implementing the compensated estimated angle for closed loop sensorless control it was found that the PLL gains had to be tuned for stability. Even though very accurate

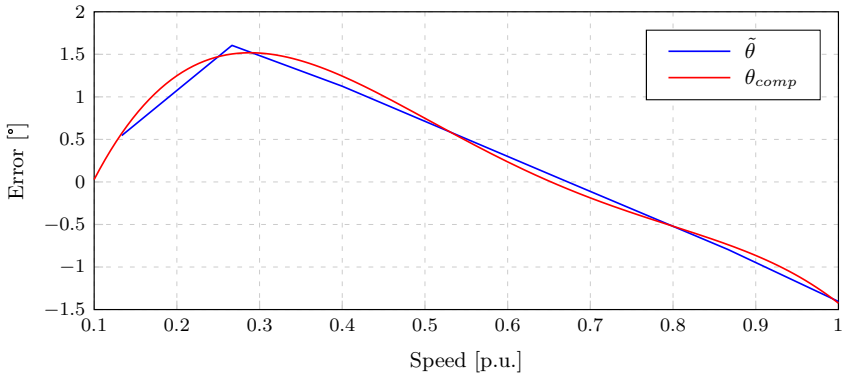

Figure 4.17: The speed dependent compensation curve implemented under positive current for the active-flux method.

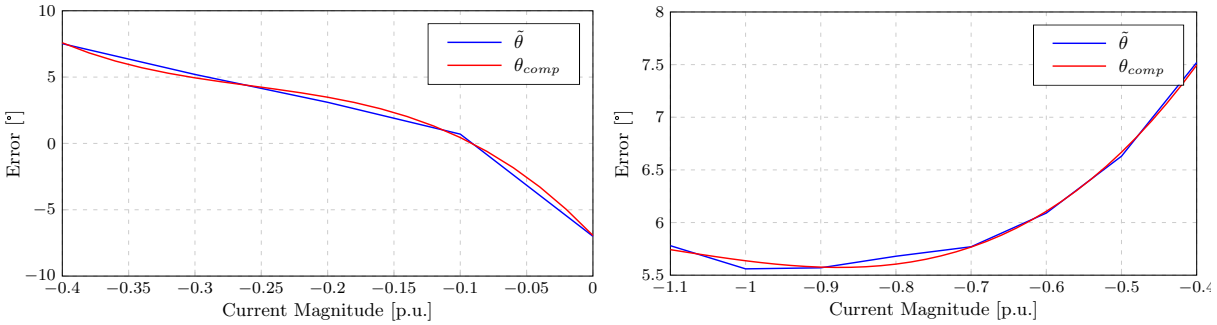

(a) Unsaturated negative current compensation (b) Saturated negative current compensation

Figure 4.18: The active-flux method compensation curves for negative current.

Table 4.1: Practical setup active-flux PLL gains

Gain	**Value**
$K_{P,+}$	240
$K_{I,+}$	4800
$K_{P,-}$	900
$K_{I,-}$	32000

position observation was possible, the PLL would go out of sync when using the estimated angle for control. For positive current conditions the PLL gains were slightly modified to result in a stable controller under all load conditions from low to rated speed. For negative current conditions the PLL gains had to be increased quite considerably in order to allow use of the estimated angle for sensorless control. With the theoretical PLL gains just a slight estimation error (2-3 degrees) would result in the PLL going out of sync and control of the machine would be lost. Even though noise-disturbance increases with larger PLL gains as noted in [14] it was found that the PLL could be made very fast for negative current conditions. This however was not the case for positive currents. Subsequently the AF estimator PLL was very fast when operating in the negative current region and did not require speed-dependent estimation error compensation for good dynamics. The resulting PLL gains for positive and negative currents are given in Table 4.1.

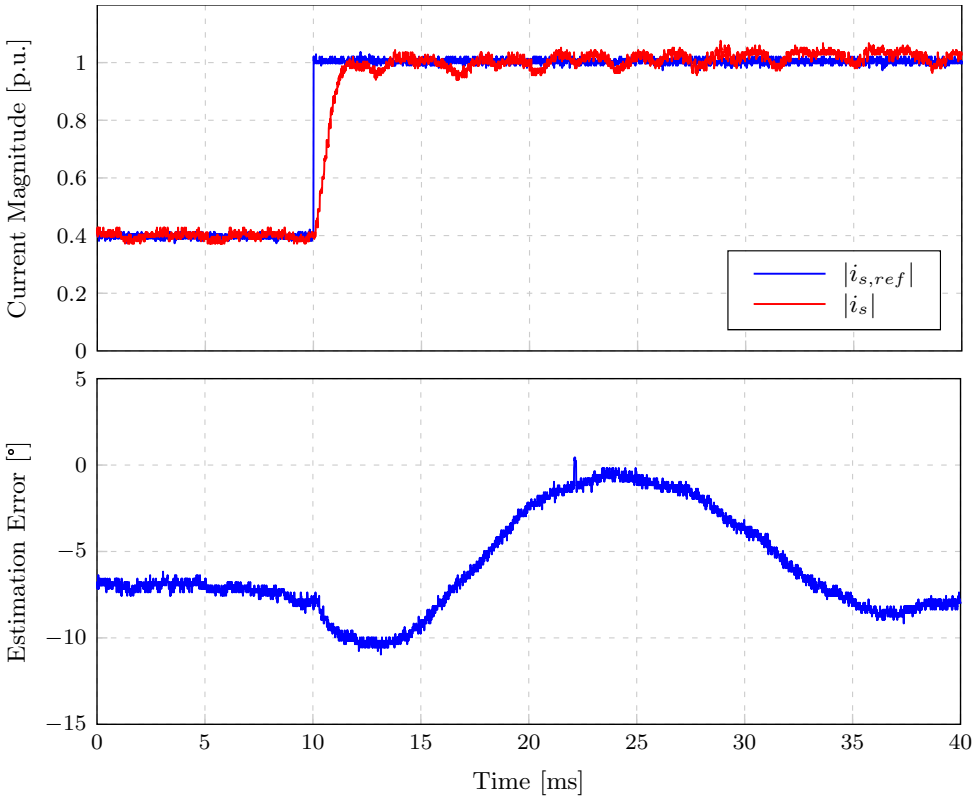

Figure 4.19: A measured sensorless rated-current control step measurement at rated-speed using the active-flux method plotting stator current and electrical angle estimation error versus time.

4.5.3 Sensorless control

In Figure 4.19 a large AF sensorless current control step at rated speed from the saturation point to rated-current is shown. It can be seen that the current control is stable and settles within 2 ms, since speed voltage compensation is implemented. The estimation error has a relatively large ripple, but remains stable and settles. Note that the rated speed for the sensorless RSM drive system was lowered to 1300 r/min, because of a limited 3-ψ supply and subsequent DC-bus voltage, causing the SVPWM scheme to saturate and the AF method to fail since it uses the reference stator voltage vector in its estimation. This is not the case for negative currents since the stator voltage vector is much smaller in magnitude and thus the rated speed under generator mode is left at 1500 r/min.

A sensorless rated-current low- to rated-speed control step is shown in Figure 4.20. The speed response is relatively slow compared to the sensored results in chapter 3, but this is required for stable closed loop sensorless control. It can be seen that the estimation error jumps during speed transients, also directly proportional to the current magnitude. Nonetheless sensorless speed control is stable with a small estimation error.

Another sensorless speed control step is shown in Figure 4.21, this time operating as a generator. It can be seen than the control is stable with a load torque step at speed and that the estimation error magnitude increases at lower speeds, since no speed-dependent compensation is implemented in generator mode for the AF method. The fast PLL allows good estimation during the speed transients.

Figure 4.22 shows a sensorless speed control step with a large torque load being applied and removed at speed. It can be seen that the estimation error jumps when the load is applied, but that the speed control is stable at above rated load. Once again it is evident

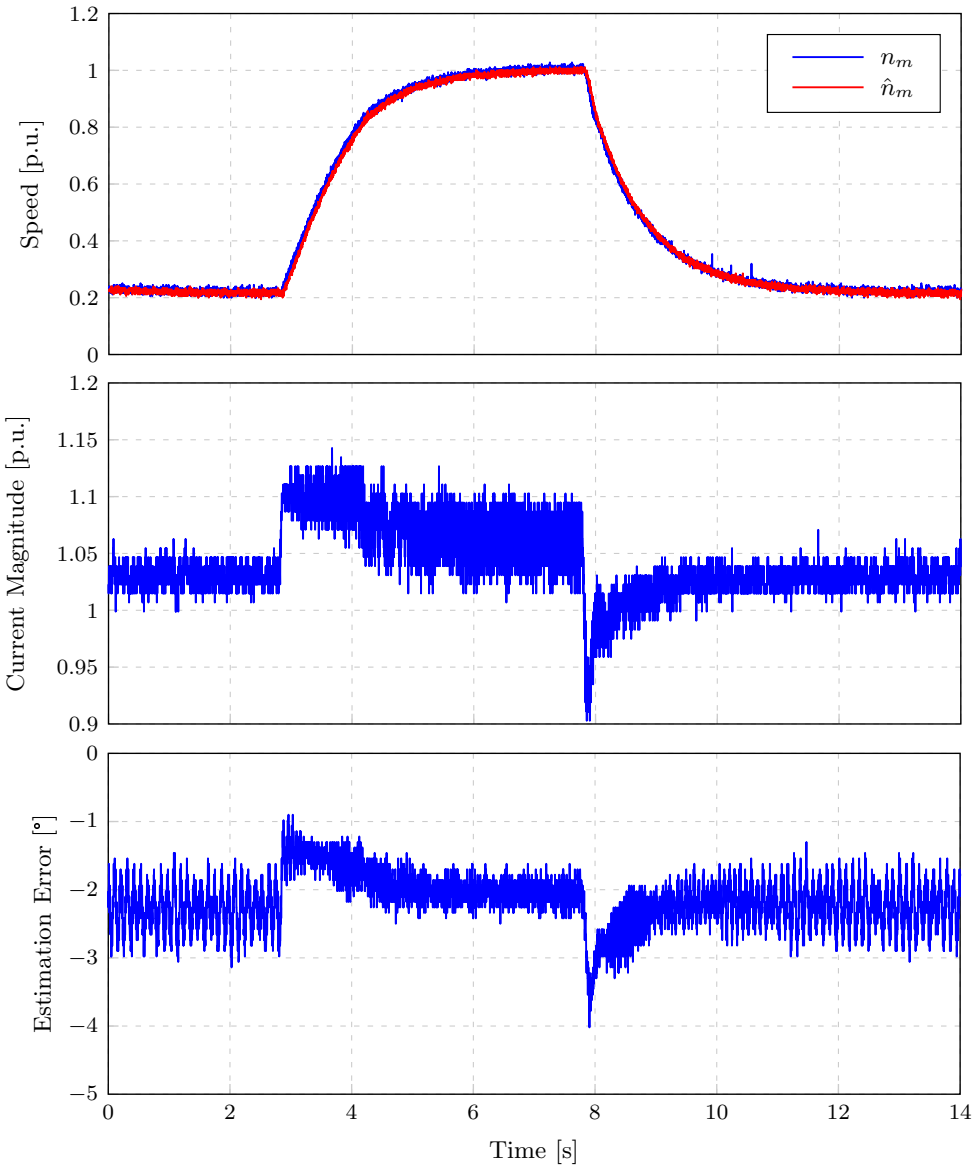

Figure 4.20: A measured rated load sensorless speed control step measurement from medium to rated-speed using the active-flux method plotting machine speed, stator current and estimation error versus time.

that the AF estimation has a measurable error during speed transients, limiting speed control dynamics.

These practical measurements show the capability of the AF method for sensorless control of the transverse-laminated RSM from low- to rated-speed in the entire rated load range. It will be implemented as part of a hybrid sensorless controller scheme in chapter 6.

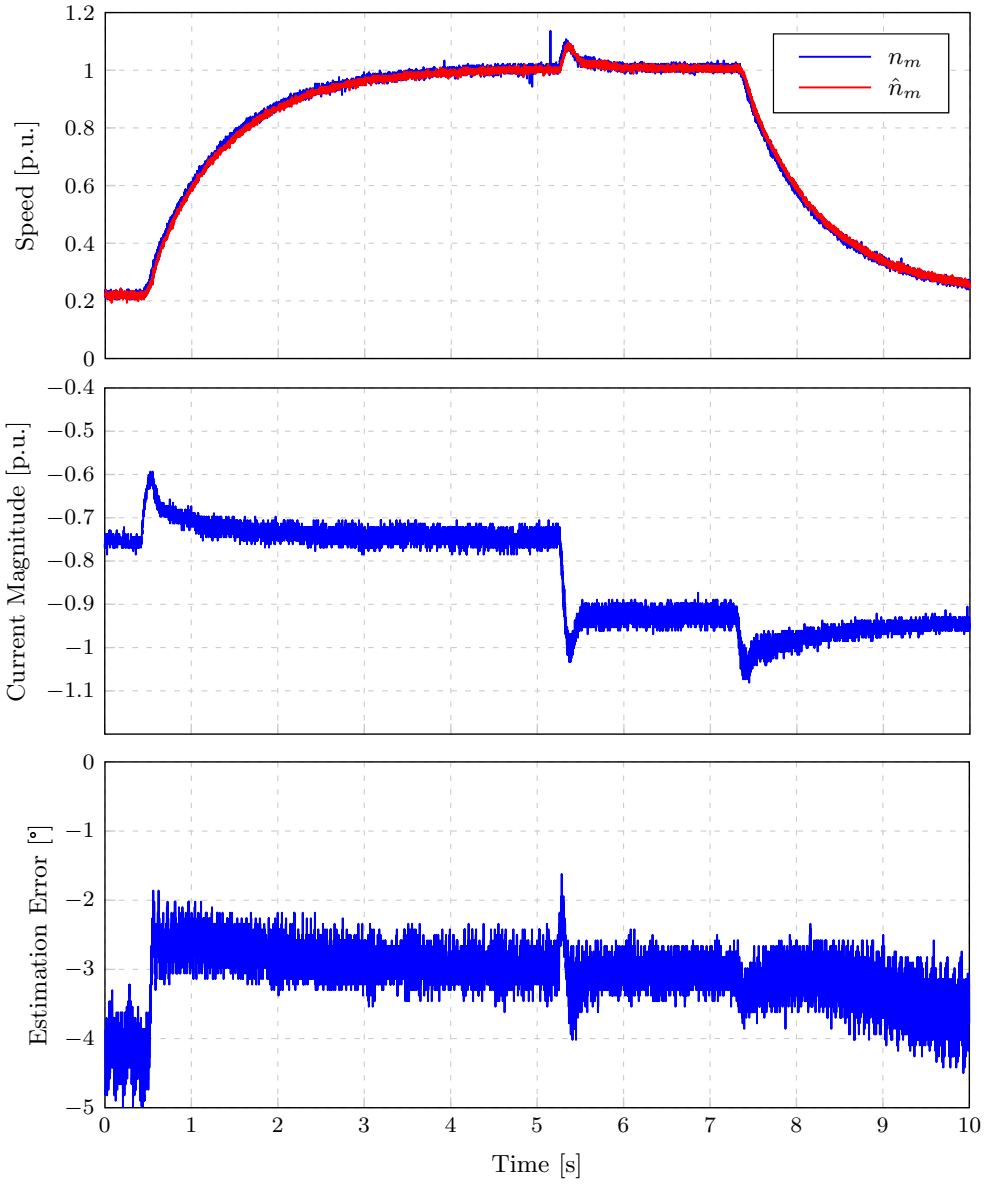

Figure 4.21: A measured sensorless generator speed control step measurement from medium to rated-speed using the active-flux method plotting machine speed, stator current and estimation error versus time.

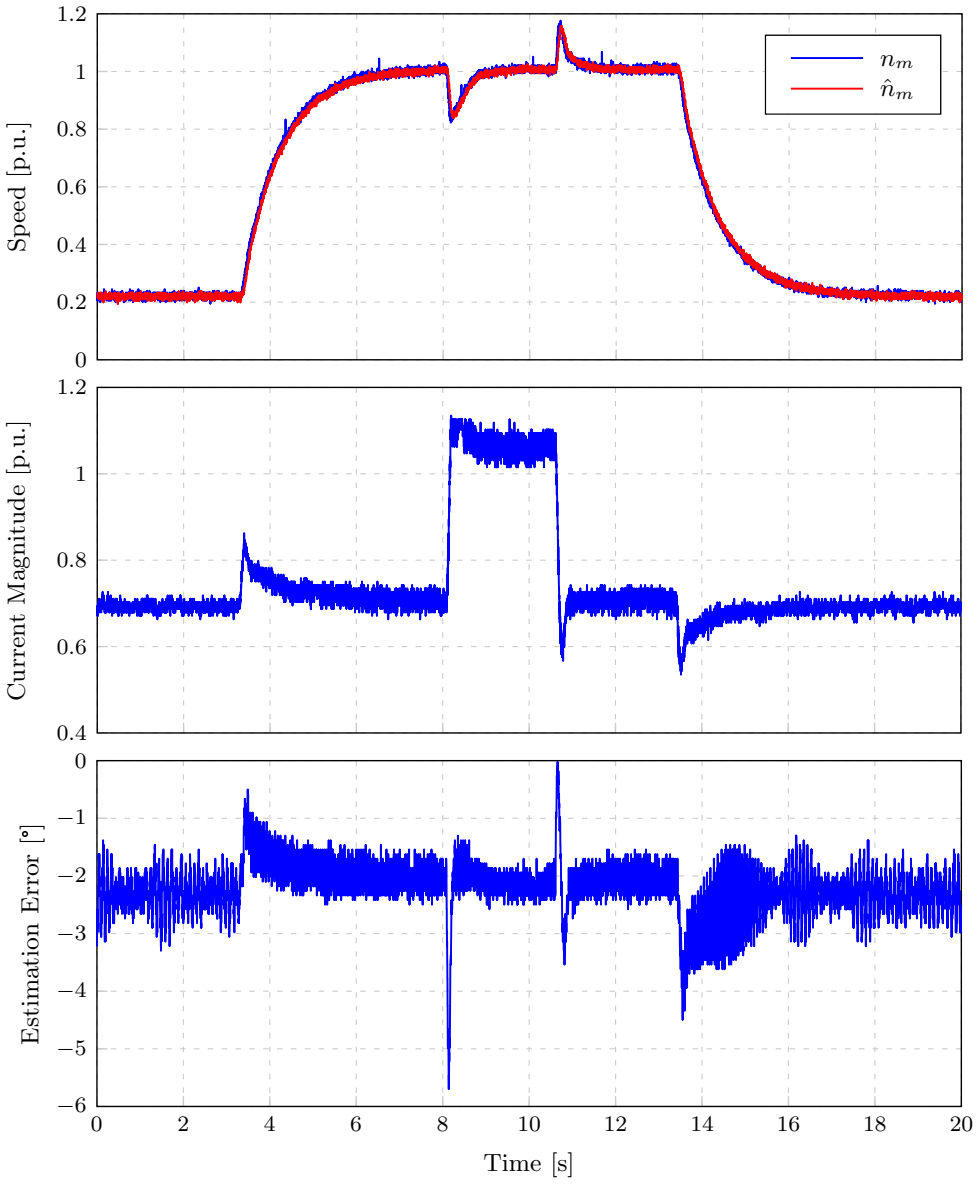

Figure 4.22: A measured sensorless load-step rated-speed control measurement using the active-flux method plotting machine speed, stator current and estimation error versus time.

Chapter 5

Arbitrary Injection Position Estimation Method

This chapter contains the investigation into the arbitrary injection position estimation method including the mathematical derivation, practical considerations for implementation on the investigated machine, simulation- and measured-results.

The arbitrary injection (AI) position estimation technique is a rather novel saliency-based method relying on the presence of a current derivative with the advantage of requiring no predetermined injection signal shape, allowing the use of a smaller fraction of the DC bus voltage [23]. This scheme enables elimination of some machine parameters in the position estimation algorithm as well as on-line parameter identification, allowing position estimation without any knowledge of machine parameters [27]. The AI method can be applied to any synchronous machine since it is based on the general model of synchronous machines and it is parameter independent with the use of online parameter identification [33].

The AI scheme implemented in this project is based on a combination of the work presented in [23, 27, 26] as comprehensively explained in [33].

5.1 Current Progression

The stator flux-linkage magnitude and orientation in the RSM is only caused by the stator currents as [26]

$$\begin{aligned}\boldsymbol{\psi}_s^s &= \boldsymbol{\psi}_s^s(\boldsymbol{i}_s^s, \theta_e) \\ &= \mathbf{T}\boldsymbol{\psi}_s^r(\boldsymbol{i}_s^r) \\ &= \mathbf{T}\boldsymbol{\psi}_s^r(\mathbf{T}^{-1}\boldsymbol{i}_s^s).\end{aligned} \tag{5.1.1}$$

Assuming a linear dependence of flux-linkage on stator current in the rotor reference frame (i.e. flux-linkage can be calculated using the inductance matrix $\tilde{\boldsymbol{L}}_s^r$) results in the following [26]:

$$\boldsymbol{\psi}_s^r(\boldsymbol{i}_s^r) = \tilde{\boldsymbol{L}}_s^r \boldsymbol{i}_s^r \tag{5.1.2}$$

so that the stator flux-linkage vector is

$$\boldsymbol{\psi}_s^s = \mathbf{T}\tilde{\boldsymbol{L}}_s^r\mathbf{T}^{-1}\boldsymbol{i}_s^s \tag{5.1.3}$$

$$= \tilde{\boldsymbol{L}}_s^s \boldsymbol{i}_s^s \tag{5.1.4}$$

where $\tilde{\boldsymbol{L}}_s^s = \mathbf{T}\tilde{\boldsymbol{L}}_s^r\mathbf{T}^{-1}$. Since the RSM rotor is anisotropic the rotor inductance vector is constant [26] as

$$\tilde{\boldsymbol{L}}_s^r = \begin{bmatrix} \tilde{L}_d & 0 \\ 0 & \tilde{L}_q \end{bmatrix}. \tag{5.1.5}$$

The stator tangential inductance matrix is then calculated as

$$\tilde{\boldsymbol{L}}_s^s = \begin{bmatrix} \tilde{L}_d \cos^2\theta_e + \tilde{L}_q \sin^2\theta_e & (\tilde{L}_d - \tilde{L}_q)\sin\theta_e\cos\theta_e \\ (\tilde{L}_d - \tilde{L}_q)\sin\theta_e\cos\theta_e & \tilde{L}_d \sin^2\theta_e + \tilde{L}_q\cos^2\theta_e \end{bmatrix} \tag{5.1.6}$$

and rewritten

$$\tilde{\boldsymbol{L}}_s^s = \frac{\tilde{L}_d + \tilde{L}_q}{2}\begin{bmatrix} 1 & 0 \\ 0 & 1 \end{bmatrix} + \frac{\tilde{L}_d - \tilde{L}_q}{2}\begin{bmatrix} \cos 2\theta_e & \sin 2\theta_e \\ \sin 2\theta_e & -\cos 2\theta_e \end{bmatrix} \tag{5.1.7}$$

$$\tilde{\boldsymbol{L}}_s^s = \tilde{L}_\Sigma \mathbf{I} + \tilde{L}_\Delta \mathbf{S}(\theta_e). \tag{5.1.8}$$

In the form of (5.1.8) the stator inductance is separated into isotropic and rotating terms [26]

$$\tilde{L}_\Sigma = \frac{\tilde{L}_d + \tilde{L}_q}{2} \tag{5.1.9}$$

and

$$\tilde{L}_\Delta = \frac{\tilde{L}_d - \tilde{L}_q}{2} \tag{5.1.10}$$

where

$$\mathbf{S}(\theta_e) = \begin{bmatrix} \cos 2\theta_e & \sin 2\theta_e \\ \sin 2\theta_e & -\cos 2\theta_e \end{bmatrix}. \tag{5.1.11}$$

Now taking the time derivative of (5.1.4) results in

$$\frac{d\boldsymbol{\psi}_s^s}{dt} = \tilde{\boldsymbol{L}}_s^s \frac{d\boldsymbol{i}_s^s}{dt} + \frac{d\tilde{\boldsymbol{L}}_s^s}{dt}\boldsymbol{i}_s^s \tag{5.1.12}$$

and the stator inductance is a function of the electrical angle which is a function of time so that

$$\begin{aligned} \frac{d\tilde{\boldsymbol{L}}_s^s}{dt} &= \frac{\partial \tilde{\boldsymbol{L}}_s^s}{\partial \theta_e}\frac{d\theta_e}{dt} \\ &= \frac{\partial \tilde{\boldsymbol{L}}_s^s}{\partial \theta_e}\omega_e. \end{aligned} \tag{5.1.13}$$

Solving for the current/time derivative in (5.1.12)

$$\frac{d\boldsymbol{i}_s^s}{dt} = \tilde{\boldsymbol{L}}_s^{s-1}\left(\frac{d\boldsymbol{\psi}_s^s}{dt} - \omega_e \frac{\partial \tilde{\boldsymbol{L}}_s^s}{\partial \theta_e}\boldsymbol{i}_s^s\right) \tag{5.1.14}$$

and substituting $\frac{d\psi_s^s}{dt}$ with (2.1.2) gives

$$\frac{d\boldsymbol{i}_s^s}{dt} = \tilde{\boldsymbol{L}}_s^{s-1}\left(\boldsymbol{v}_s^s - R_s\boldsymbol{i}_s^s - \omega_e\frac{\partial\tilde{\boldsymbol{L}}_s^s}{\partial\theta_e}\boldsymbol{i}_s^s\right). \tag{5.1.15}$$

The inverse of the stator inductance in stator reference frame $\tilde{\boldsymbol{L}}_s^{s-1}$ is calculated

$$\tilde{\boldsymbol{L}}_s^{s-1} = \frac{1}{\left|\tilde{\boldsymbol{L}}_s^s\right|}\begin{bmatrix}\tilde{L}_d\sin^2\theta_e + \tilde{L}_q\cos^2\theta_e & (\tilde{L}_q - \tilde{L}_d)\sin\theta_e\cos\theta_e \\ (\tilde{L}_q - \tilde{L}_d)\sin\theta_e\cos\theta_e & \tilde{L}_d\cos^2\theta_e + \tilde{L}_q\sin^2\theta_e\end{bmatrix} \tag{5.1.16}$$

$$= \frac{1}{\tilde{L}_d\tilde{L}_q}\left[\tilde{L}_\Sigma\mathbf{I} - \tilde{L}_\Delta\mathbf{S}(\theta_e)\right]. \tag{5.1.17}$$

This is rewritten in terms of inverse isotropic and rotating inductance terms as

$$\tilde{\boldsymbol{L}}_s^{s-1} = Y_\Sigma\mathbf{I} + Y_\Delta\mathbf{S}(\theta_e) \tag{5.1.18}$$

where the inverse inductances are equal to

$$Y_\Sigma = \frac{Y_d + Y_q}{2} \tag{5.1.19}$$

$$Y_\Delta = \frac{Y_d - Y_q}{2} \tag{5.1.20}$$

and $Y_d = 1/\tilde{L}_d, Y_q = 1/\tilde{L}_q$. Rewriting the inverse inductance matrix in this form allows much simpler calculations and highlights the effects of the isotropic and rotating components of the inverse inductances in the current progression.

The current progression can be derived by inserting $\frac{d\boldsymbol{i}_s^s}{dt} = \frac{\Delta\boldsymbol{i}_s^s}{\Delta t}$ $(\Delta t = T_s)$ into (5.1.15) which results in [26]

$$\Delta\boldsymbol{i}_s^s = \tilde{\boldsymbol{L}}_s^{s-1}\left(\boldsymbol{v}_s^s - R_s\boldsymbol{i}_s^s\right)\Delta t - \omega_e\tilde{\boldsymbol{L}}_s^{s-1}\frac{\partial\tilde{\boldsymbol{L}}_s^s}{\partial\theta_e}\boldsymbol{i}_s^s\Delta t \tag{5.1.21}$$

$$= \tilde{\boldsymbol{L}}_s^{s-1}\boldsymbol{v}_L^s\Delta t + \Delta\boldsymbol{i}_{FM}^s \tag{5.1.22}$$

which is separted into a scaling and rotating component by substituting (5.1.18)

$$\Delta\boldsymbol{i}_s^s = Y_\Sigma\boldsymbol{v}_L^s\Delta t + Y_\Delta\mathbf{S}(\theta_e)\boldsymbol{v}_L^s\Delta t + \Delta\boldsymbol{i}_{FM}^s \tag{5.1.23}$$

$$= \Delta\hat{\boldsymbol{i}}_{s\Sigma}^s + \Delta\boldsymbol{i}_{HF}^s + \Delta\boldsymbol{i}_{FM}^s. \tag{5.1.24}$$

$\Delta\boldsymbol{i}_{HF}^s$ and $\Delta\boldsymbol{i}_{FM}^s$ are circulating current terms rotating at twice the electrical frequency. The fundamental circulation of the current at constant flux ($\boldsymbol{v}_s^s = 0$), $\Delta\boldsymbol{i}_{FM}^s$, is induced by the salient motor rotation. The high frequency circulating current $\Delta\boldsymbol{i}_{HF}^s$ results from applying the voltage $\boldsymbol{v}_L^s$ to an anisotropic inductance and is oriented by the rotor angle θ_e. Disregarding the saliency of the rotor ($\tilde{L}_d = \tilde{L}_q$) in (5.1.21) results in the current progression for an isotropic machine as in [26]

$$\Delta\hat{\boldsymbol{i}}_{s\Sigma}^s = Y_\Sigma\boldsymbol{v}_L^s\Delta t. \tag{5.1.25}$$

Figure 5.1 shows the current progression vector and the difference in current progression when disregarding the rotor saliency. The green high frequency vector rotates in the

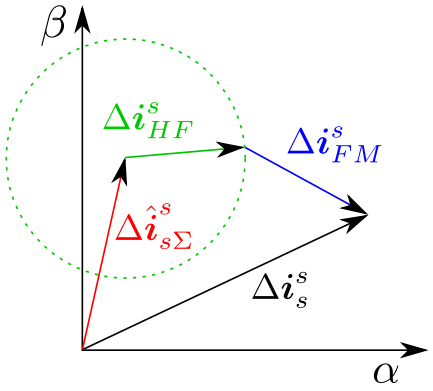

Figure 5.1: The current progression vector separated into its scaling and rotating components [26].

circle shown and the blue fundamental circulation of current vector rotates in a similar fashion from the end-point of the $\Delta \boldsymbol{i}^s_{HF}$ vector. Since both vectors rotate with the rotor either one can be used to determine the rotor angle. From [26] $\Delta \boldsymbol{i}^s_{FM}$ scales with rotor speed ω_e and current magnitude $|\boldsymbol{i}^s_s|$ whereas $\Delta \boldsymbol{i}^s_{HF}$ only scales with the inductance voltage $\boldsymbol{v}^s_L$ - which could be made available in all operating conditions by applying a high-frequency voltage additional to the current control reference voltage on the stator. With this knowledge $\Delta \boldsymbol{i}^s_{HF}$ will be used for estimation of the rotor position.

5.1.1 Predicted Progression

Using Euler's method from [54] for an approximation of (5.1.25) enables discrete prediction of the current progression for an isotropic machine after every switching step as [23]

$$\Delta \hat{\boldsymbol{i}}^s_{s\Sigma}[n] = Y_\Sigma \left(\boldsymbol{v}^s_s[n_1] - R_s \boldsymbol{i}^s_s[n_1] \right) \Delta t \tag{5.1.26}$$

where $[n_1] = [n-1]$ refers to the previous calculation interval (i.e. the value at the previous switching step). In contrast, the measured current progression of the salient pole machine is calculated as [23]

$$\Delta \boldsymbol{i}^s_s[n] = \boldsymbol{i}^s_s[n] - \boldsymbol{i}^s_s[n_1]. \tag{5.1.27}$$

It is now apparent from (5.1.23) that $\Delta \boldsymbol{i}^s_{HF}$ can be determined by subtracting $\Delta \boldsymbol{i}^s_{FM}$ from the current prediction error - which is the difference between the predicted isotropic current progression and the measured anisotropic current progression - so that

$$\Delta \boldsymbol{i}^s_{HF} = (\Delta \boldsymbol{i}^s_s - \Delta \hat{\boldsymbol{i}}^s_{s\Sigma}) - \Delta \boldsymbol{i}^s_{FM} \tag{5.1.28}$$

$$= \boldsymbol{i}^s_{\Delta err} - \Delta \boldsymbol{i}^s_{FM}. \tag{5.1.29}$$

5.2 Parameter Reduction and Identification

In order to calculate the high frequency current progression from (5.1.28) precise knowledge of the stator resistance R_s, mean inverse inductance Y_Σ (for $\Delta \hat{\boldsymbol{i}}^s_{s\Sigma}$) and stator inductance $\tilde{L}_{d/q}$ (for $\Delta \boldsymbol{i}^s_{FM}$) is required. This section describes steps that can be taken to eliminate all predetermined machine parameter dependencies in the arbitrary injection based position estimation scheme.

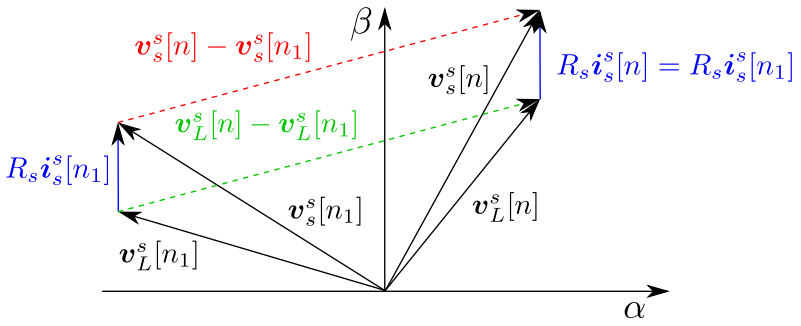

Figure 5.2: The variation in voltage between consecutive switching states.

5.2.1 Stator Resistance

Usually the term $R_s\boldsymbol{i}_s^s$ in (5.1.21) is small compared to $\boldsymbol{v}_s^s$ so that its difference between two consecutive switching states is certainly negligible. The variation in stator voltage between switching states would then be equal to the variation in inductance voltage, $\Delta\boldsymbol{v}_s^s = \Delta\boldsymbol{v}_L^s$, as shown in Figure 5.2, since $R_s\boldsymbol{i}_s^s$ is considered to be constant. The difference in predicted current progressions would then result in [23]

$$\Delta(\Delta\hat{\boldsymbol{i}}_{s\Sigma}^s) = Y_\Sigma(\Delta\boldsymbol{v}_s^s)\Delta t \tag{5.2.1}$$

where $\Delta\boldsymbol{v}_s^s = \boldsymbol{v}_s^s[n_1] - \boldsymbol{v}_s^s[n_2]$.

The difference in measured current progressions can be calculated as

$$\Delta(\Delta\boldsymbol{i}_s^s) = \boldsymbol{i}_s^s[n] - 2\boldsymbol{i}_s^s[n_1] + \boldsymbol{i}_s^s[n_2] \tag{5.2.2}$$

so that assuming the switching frequency is sufficiently larger than the electrical speed, $F_s >> \omega_e$, so that $\Delta\boldsymbol{i}_{FM}^s$ can still be considered, the current prediction error is calculated as

$$\boldsymbol{i}_{\Delta err}^s = \Delta(\Delta\boldsymbol{i}_s^s) - \Delta(\Delta\hat{\boldsymbol{i}}_{s\Sigma}^s) \tag{5.2.3}$$

and used to calculate $\Delta\boldsymbol{i}_{HF}^s$ without knowledge of the stator resistance, R_s [23]. This is possible, because as shown in [23] it makes no difference whether current progressions or difference between current progressions are regarded.

5.2.2 Mean Inverse Inductance

Since the mean inverse machine inductance is required to calculate the predicted current progression (or the difference thereof) it is a parameter that cannot be cancelled out in the arbitrary injection estimation scheme. In [27] a mean admittance estimation scheme is derived and it is applied to a specific injection sequence - similar to the one used for this project - in [23] allowing a fast update of the average inductance. According to [23] the current slope after applying a voltage vector represents the actual machine admittance for that excitation.

As described in [23] the mean admittance (mean inverse inductance Y_Σ) can be obtained by rotating the excitation voltage direction (injection direction) and integrating the current response in the injection frame for half a rotation as

$$Y_\Sigma = \frac{1}{\pi}\int_0^\pi \frac{\frac{d}{dt}i_\delta}{v_\delta}d\theta_e, \tag{5.2.4}$$

where δ is the injection direction component, when assuming the machine is not rotating. A 3-step rotating injection vector in each phase direction is implemented in this project so that according to [27] the inverse inductance at each switching step can be discretely estimated as

$$\hat{Y}_{tX} = \frac{\Delta \boldsymbol{i}_{HF}^{s\,T} \boldsymbol{v}_s^s}{\boldsymbol{v}_s^{sT} \boldsymbol{v}_s^s}, X = 1, 2, 3. \tag{5.2.5}$$

Since the injected voltages are symmetrically distributed the mean admittance estimation equals

$$\hat{Y}_\Sigma = \frac{\hat{Y}_{t1} + \hat{Y}_{t2} + \hat{Y}_{t3}}{3} \tag{5.2.6}$$

which is combined to result in a mean inverse inductance available at every switching step

$$\hat{Y}_\Sigma = \frac{1}{3} \sum_{k=1}^{3} \frac{\Delta \boldsymbol{i}_{HF}^{s\,T} \boldsymbol{v}_s^s}{\boldsymbol{v}_s^{sT} \boldsymbol{v}_s^s}. \tag{5.2.7}$$

5.2.3 Machine Inductances

The remaining parameter in the estimation scheme is the machine inductance $\tilde{L}_{d/q}$ which is used to calculate $\Delta \boldsymbol{i}_{FM}^s$. According to [26] the high frequency circulating current can be separated from the fundamental circulation of the current when considering their frequency content. $\Delta \boldsymbol{i}_{HF}^s$ reverses at every prediction time step while $\Delta \boldsymbol{i}_{FM}^s$ rotates at around the frequency of the rotor speed. Consequently in rotor reference frame $\Delta \boldsymbol{i}_{FM}^s$ is relatively constant [26]. Therefore $\Delta \boldsymbol{i}_{HF}^s$ can be determined by high-pass filtering (HPF) the current prediction error $\boldsymbol{i}_{\Delta err}^s$ - specifically in rotor reference frame - which eliminates the need to calculate $\Delta \boldsymbol{i}_{FM}^s$ with subsequent knowledge of the machine inductance. The high frequency circulating current is then calculated as

$$\Delta \boldsymbol{i}_{HF}^s = \mathbf{T}.HPF(\mathbf{T}^{-1} \boldsymbol{i}_{\Delta err}^s) \tag{5.2.8}$$

and from (5.2.3) results in

$$\Delta \boldsymbol{i}_{HF}^s = \mathbf{T}.HPF\left\{\mathbf{T}^{-1}\left[\Delta(\Delta \boldsymbol{i}_s^s) - \Delta(\Delta \hat{\boldsymbol{i}}_{s\Sigma}^s)\right]\right\}. \tag{5.2.9}$$

5.3 Position estimation

Since the rotation matrix $\mathbf{S}(\theta_e)$ in (5.1.23) is rotor angle dependent it is possible to forecast the high frequency current progression using the feedback angle of a PLL structure as [26]

$$\Delta \hat{\boldsymbol{i}}_{HF}^s = Y_\Delta \mathbf{S}(\theta_{PLL}) \boldsymbol{v}_L^s \Delta t \tag{5.3.1}$$

and considering subsection 5.2.1

$$\Delta \hat{\boldsymbol{i}}_{HF}^s = Y_\Delta \mathbf{S}(\theta_{PLL}) \Delta \boldsymbol{v}_s^s \Delta t. \tag{5.3.2}$$

Assuming that the PLL angle is correct the vectors $\Delta \boldsymbol{i}^s_{HF}$ and $\Delta \hat{\boldsymbol{i}}^s_{HF}$ will be oriented the same way. Therefore an error signal to close the PLL can be constructed by taking the vector product of these vectors as [26]

$$e_{PLL} = \Delta \boldsymbol{i}^s_{HF}{}^T \mathbf{J}\ \Delta \hat{\boldsymbol{i}}^s_{HF},$$

where

$$\mathbf{J} = \mathbf{T}(\frac{\pi}{2}) \tag{5.3.3}$$

$$= \begin{bmatrix} 0 & -1 \\ 1 & 0 \end{bmatrix} \tag{5.3.4}$$

so that the PLL error will be equal to zero when $\theta_{PLL} = \theta_e$. Then, since the vector lengths simply act as a gain in the PLL, only orientation is considered (disregarding Y_Δ) so that

$$e_{PLL} = \Delta \boldsymbol{i}^s_{HF}{}^T \mathbf{J}\ \mathbf{S}(\theta_{PLL}) \Delta \boldsymbol{v}^s_s. \tag{5.3.5}$$

This error is fed into a PLL observer scheme with the same structure as shown in Figure 4.2 to result in the estimated angle and angular frequency.

5.4 Injection Voltage

Since the AI estimation scheme requires the presence of a current time derivative (i.e. a change in current for every switching step) in the stator reference frame, a square wave spatially rotating 120° in the stator reference frame every switching cycle (T_s) (i.e. aligned with the 3 stator phase-axes) as shown in Figure 5.3 is injected. This allows online admittance calculation as in subsection 5.2.2 because it is symmetrically distributed as in [27] and the high frequency yields more frequent position information, larger separation from the current controller bandwidth and lower audible noise [23]. The reference stator voltages for control of the machine is calculated in the control algorithm which is then superimposed with the injection voltage.

The injected voltage vector, $\boldsymbol{v}_{inj}$, superimposed on the stator voltage vector is shown in Figure 5.4 with the outline of the hexagon being the maximum voltage that can be applied using SVPWM (see Appendix B). This figure also makes it apparent that the AI scheme has limited torque capabilities for a certain DC-bus voltage depending on the injection voltage magnitude.

5.5 Considerations for implementation

5.5.1 q-axis saturation

Since the AI scheme is reliant on the inductance saliency of the machine for rotor position estimation there must be a 'visible' difference in stator inductances $\tilde{L}_d$ and $\tilde{L}_q$. From Figure 2.8a it is evident that at zero current these values are very close to each other for the RSM investigated. This saliency can be quantified in the saliency ratio defined earlier as $(\tilde{L}_d - \tilde{L}_q)/2$. Consequently a minimum q-axis current value of at least $i_q = 0.2$ p.u. is maintained for AI estimation at no-load conditions which is just enough to saturate the q-axis as can be seen from Figure 2.7. It should be noted that for machines with very small

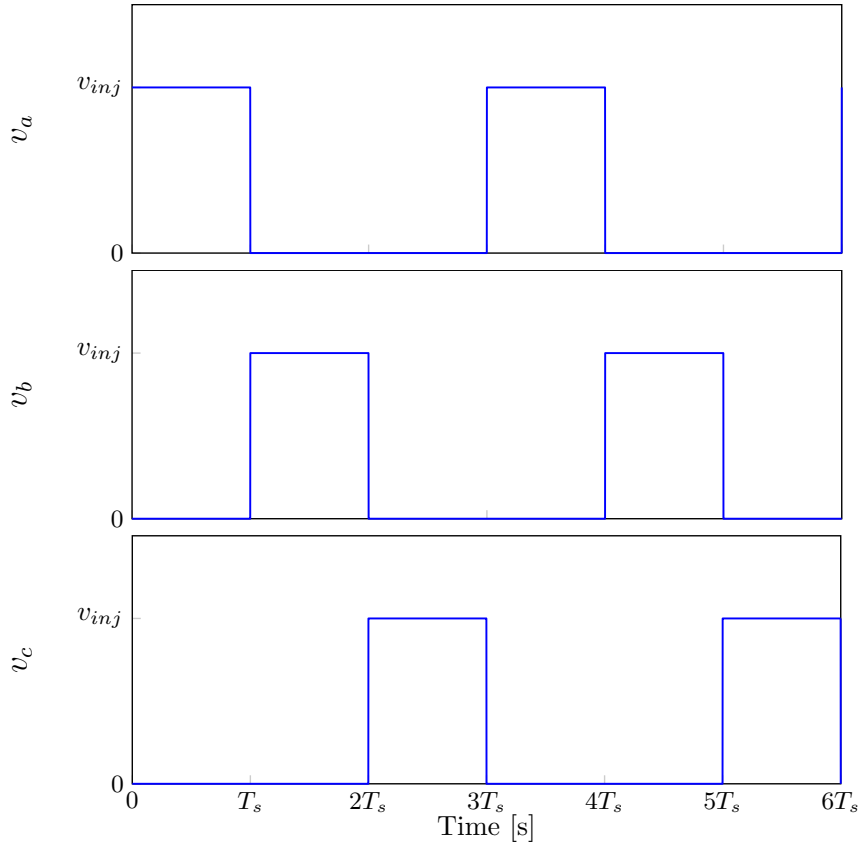

Figure 5.3: The AI voltage waveforms for two rotations of the injection voltage.

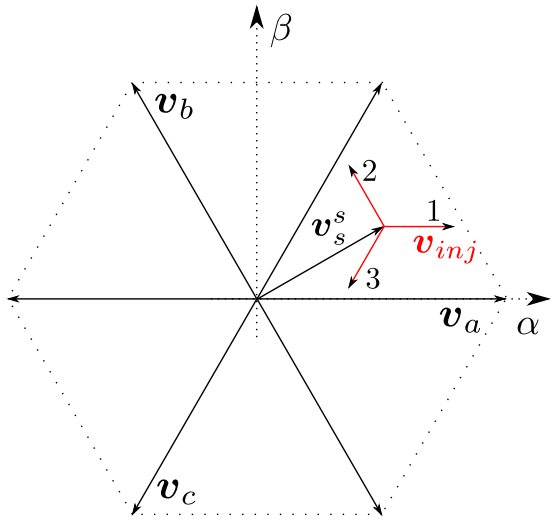

Figure 5.4: Injected voltage vector diagram inside the limits of SVPWM.

inductance saliency values it may seem that the saliency vanishes even though saliency based position sensorless control is still possible. This is because the identifiability has more to do with the difference in inductance than the saliency magnitude so that it can be redefined in terms of a saliency coefficient as in [55] to be

$$\frac{\Delta\tilde{L}}{\Sigma\tilde{L}} = \frac{\sqrt{(\tilde{L}_d - \tilde{L}_q)^2 + 4M}}{\tilde{L}_d + \tilde{L}_q}. \tag{5.5.1}$$

This coefficient is a fraction between 0 and 1 describing the identifiability of the magnetic-axis position and therefore seems an appropriate measure for valuing the suitability of a motor for sensorless control [55].

5.5.2 Injection voltage

A well known drawback of saliency based signal injection position estimation techniques is that a higher voltage injection leads to lower torque capabilities, because a limited excitation range for current control [23]. Higher voltage injection magnitude, $|\boldsymbol{v}_{inj}|$, clearly leads to a larger current progression used for AI - since it has a direct impact on $\boldsymbol{v}_L^s$ - which lowers the estimation error. Therefore, a trade-off has to be made which is done using the simulation model - to find a suitable starting point - and finally chosen using practical tests.

5.5.3 Saliency shift

Cross-saturation (mutual inductance) is also well known to have an effect on the accuracy of saliency based estimation techniques as mentioned earlier and shown in [49, 55, 56], because the magnetic-axis moves away from the rotor direct-axis under load. The estimated rotor position moving away from the actual rotor position in this manner is referred to as saliency shift [33]. If the saliency angle is used for current control (sensorless control) it takes less load for the saliency to vanish ($\tilde{L}_d \approx \tilde{L}_q$) due to saturation [26]. Consequently, as is common for saliency based techniques, a load-dependent angle compensation curve is derived by taking the AI observer estimated angle error under MTPA sensored control.

5.5.4 PLL gain selection

The AI PLL gains are chosen experimentally (first using the simulation model) with starting values relating to its approximate bandwidth. The PLL bandwidth has to be chosen slower than the current controller bandwidth, but fast enough to track the electrical angle up to at least rated speed with a speed controller bandwidth of ω_{BW}. The initial PLL gains are chosen as

$$K_{P_{PLL}} = 50, \tag{5.5.2}$$
$$K_{I_{PLL}} = 7500. \tag{5.5.3}$$

These values are used in simulation and are tuned when the AI method is implemented practically for ideal tracking.

The complete AI position estimation scheme in block diagram format is shown in Figure 5.5. The figure shows the implementation of the admittance calculation block and the PLL block with the same layout as in Figure 4.2.

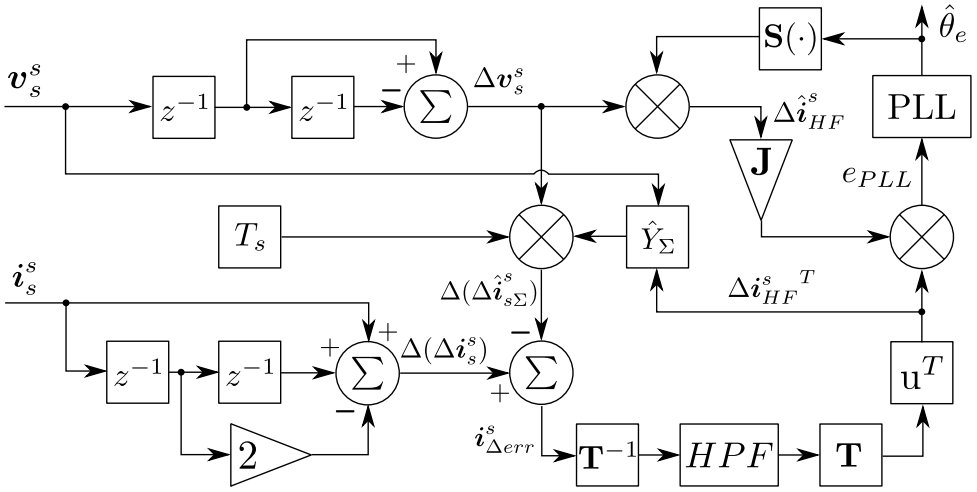

Figure 5.5: The AI position estimation scheme block digram.

5.6 Simulation Results

Before practical implementation the AI method is tested using the Simulink model derived in section 2.4 since it represents a very close match to the inductance characteristics of the machine. The simulation block diagram for the AI estimation scheme is shown in Figure 5.6 representing Figure 5.5. It contains the mean inverse inductance estimation block representing (5.2.7) as well as a PLL block with the same structure as in Figure 4.2. Figure 5.7 shows how the rotating injection voltage is added in simulation. It is important to set the simulation step time to the switching frequency of the drive system since it has a direct influence on the rotation frequency of the injected voltage as well as the AI estimation scheme itself.

The complete AI based PSC simulation block diagram for speed control of the RSM is shown in Appendix D in Figure D.5. It implements the AI estimation block in Figure 5.6 with its output error input to a PLL block with the layout given in Figure 4.2. The stator voltage vector, $\boldsymbol{v}_s^s$, is taken after the injection voltage before the voltage saturation block since that is the value available in the practical setup (as noted similarly in chapter 4).

The AI PLL gains were determined by experimental testing in the simulation environment as $K_P = 50, K_I = 7500$. The injection voltage magnitude was chosen as $v_{inj} = 160$ V, which resulted in a good estimation at standstill. This value can be made much lower with some optimisation of the PLL gains.

A simulated position sensorless locked-rotor rated-current control step in shown in Figure 5.8. It is evident that the current control is very fast, settling under 2 ms. Note the high-frequency component of the current response which is attributed to the high-frequency injected voltage rotating at every switching step. It can be shown that the current slope also changes at every switching step. This result highlights one of the drawbacks of high-frequency injection position sensorless control techniques in that they have an inherent torque ripple directly proportional to the injection voltage implemented. This simulation results shows that the AI method has a current-dependent estimation error as is explained later.

In Figure 5.9 a sensorless standstill to low-speed control step simulation under full load is shown for the AI method. Once again it can be seen that the estimation technique has a current-dependent error but also a speed-dependent estimation error attributed to saliency shift. Once again note the high frequency current ripple. The speed control

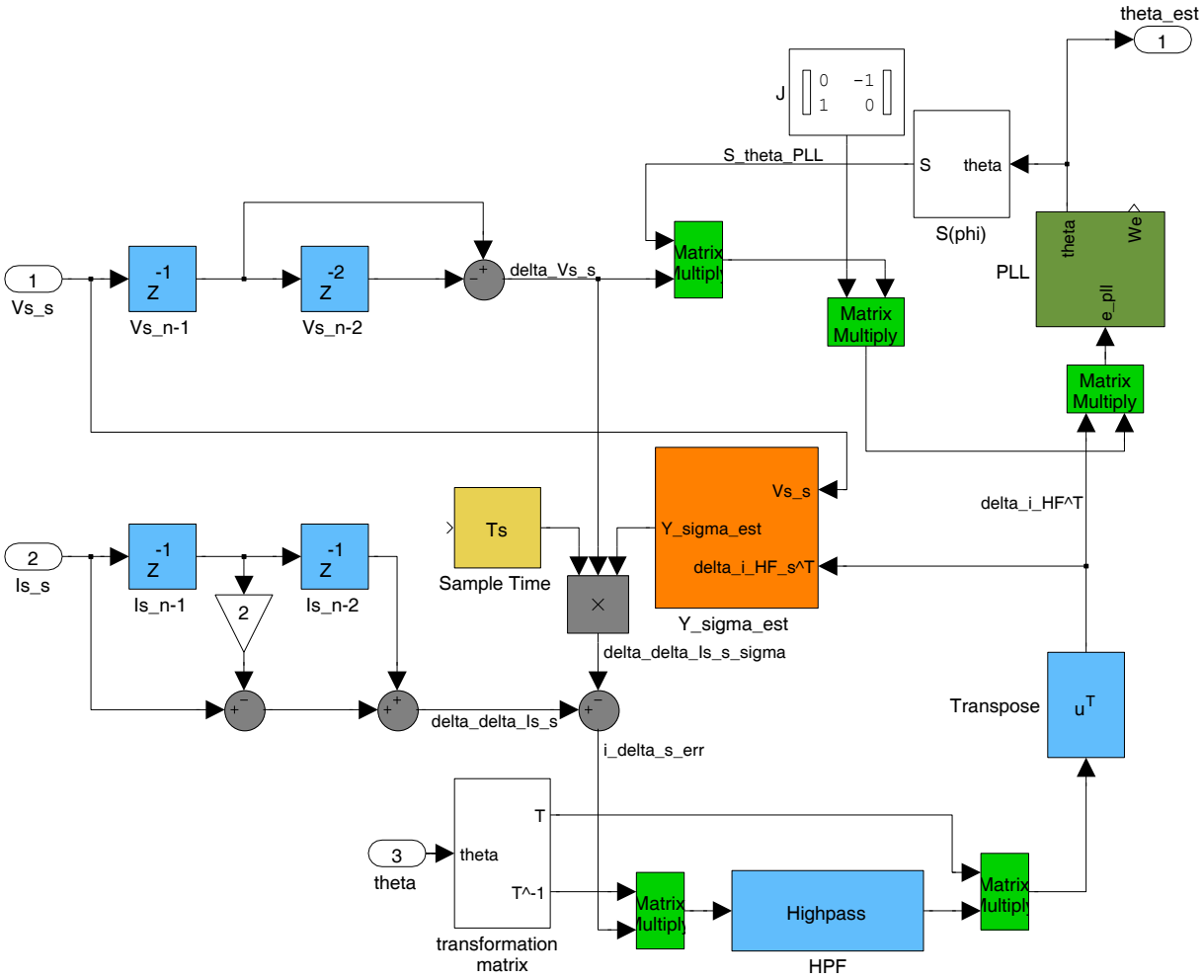

Figure 5.6: The AI estimation scheme simulation block diagram.

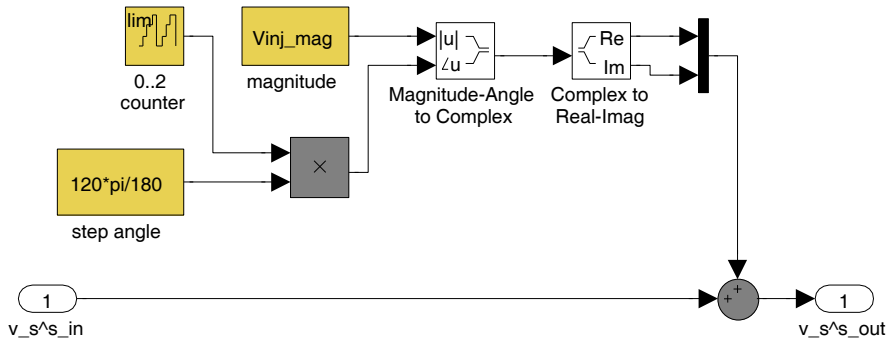

Figure 5.7: The AI injection voltage scheme simulation block diagram.

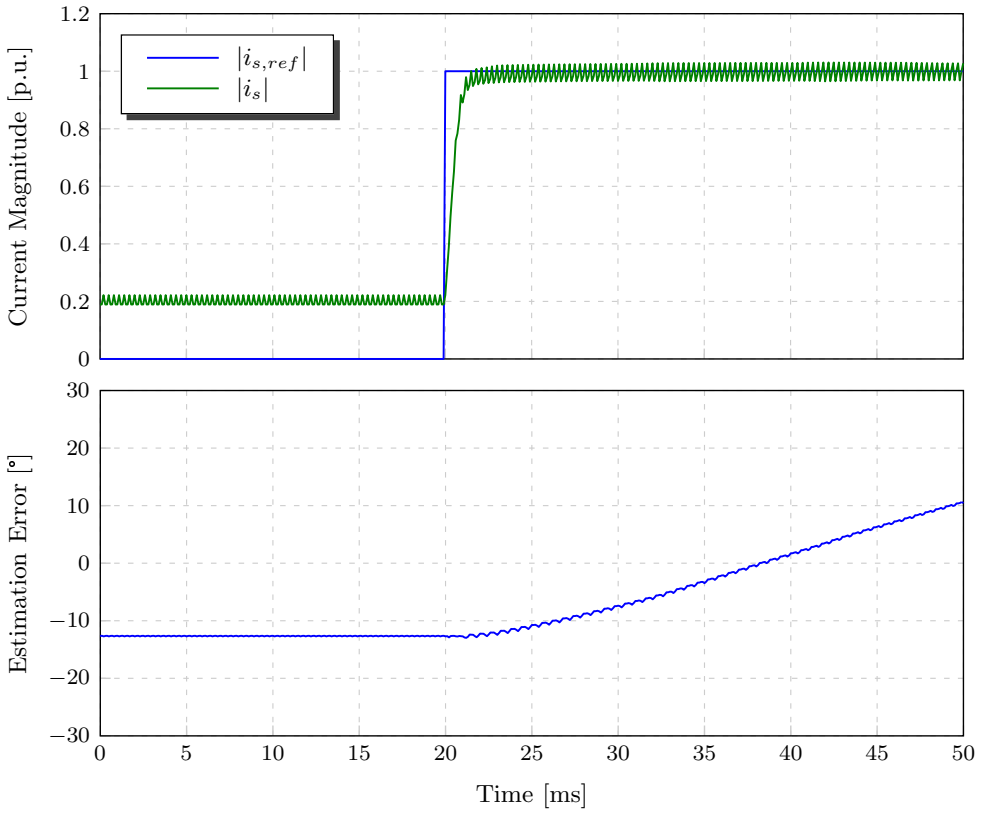

Figure 5.8: A sensorless rated-current control step simulation at standstill (locked-rotor) using the arbitrary injection method plotting stator current and electrical angle estimation error versus time.

dynamics is rather poor, but should be seen in context with the fact that no estimation error compensation is done in simulation - see the large angle estimation error ripple.

These simulation results are simply used to validate the estimation method works and closed-loop sensorless control is optimised in the practical system.

5.7 Practical Results

The AI method was implemented practically with the help of Dr. Wikus Villet during his final year of pursuing his PhD. The process was relatively straight forward after successfully implementing it under simulation.

5.7.1 Error Compensation

After implementing the AI method as an observer an estimation error as a function of machine current equation is derived. This estimation error is attributed to saliency shift [33].

The AI positive- and negative-current position estimation error and resulting compensation curves are shown in Figures 5.10 and 5.11 respectively. These curve fitted compensation curves are 2nd order polynomials.

The arbitrary injection method also exhibits strong speed dependent estimation errors, but it was deemed unnecessary to implement a speed compensation scheme since the method would be implemented at low speeds (or at least only low loads at higher speeds).

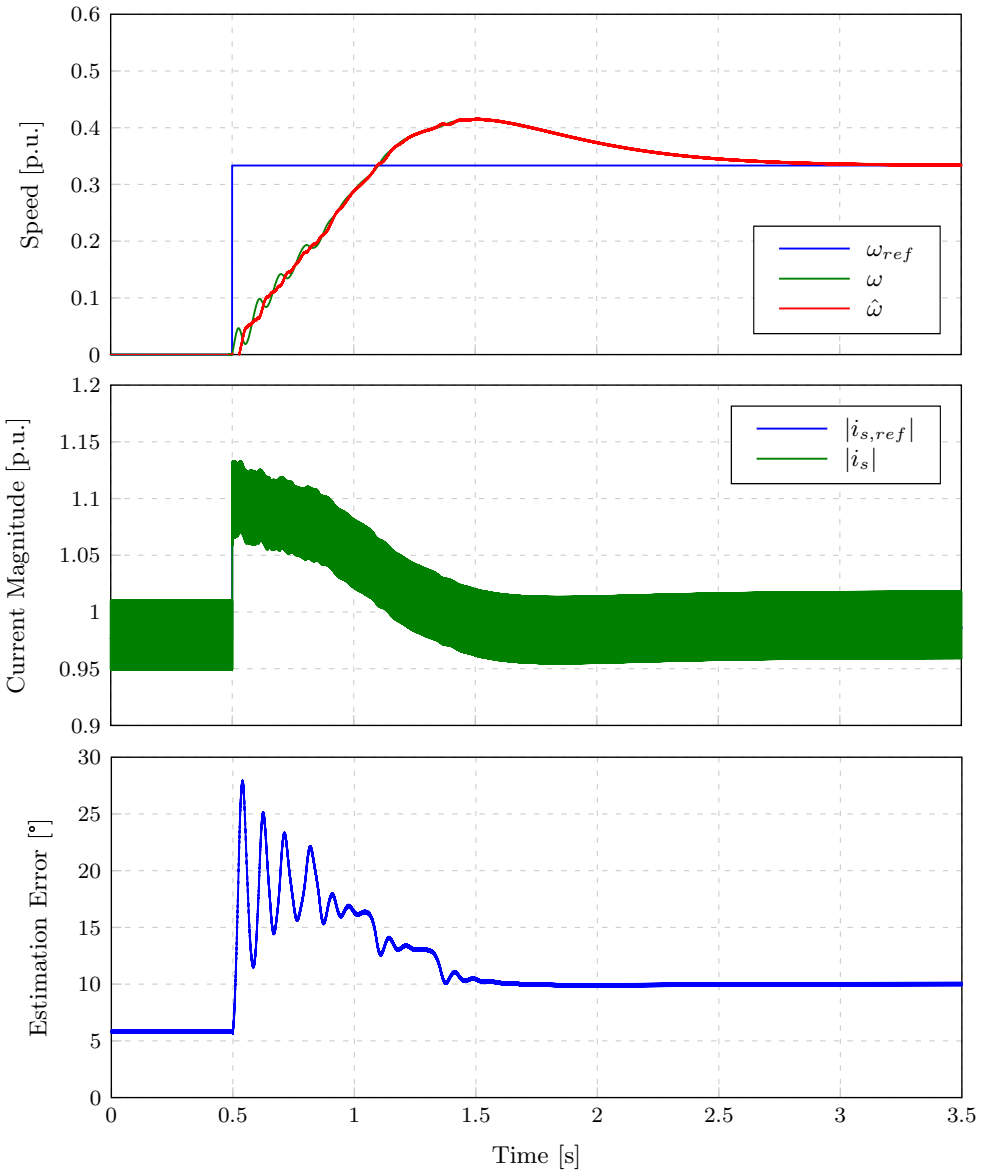

Figure 5.9: A rated-load sensorless speed control step simulation from standstill to low-speed using the arbitrary injection method plotting machine speed, stator current and estimation error versus time.

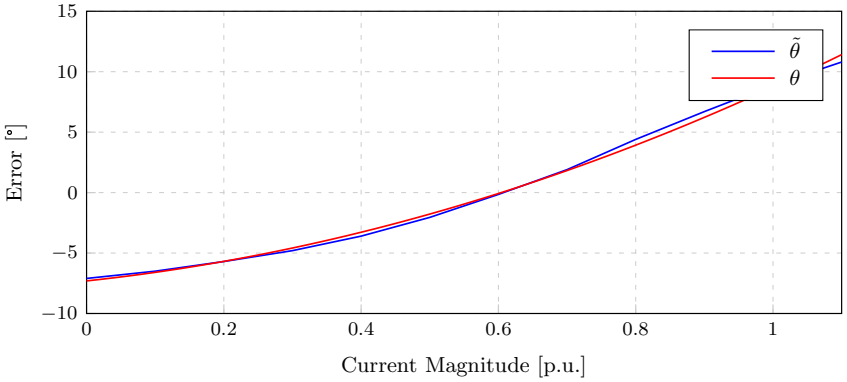

Figure 5.10: The positive current estimation error compensation curve for the arbitrary injection method.

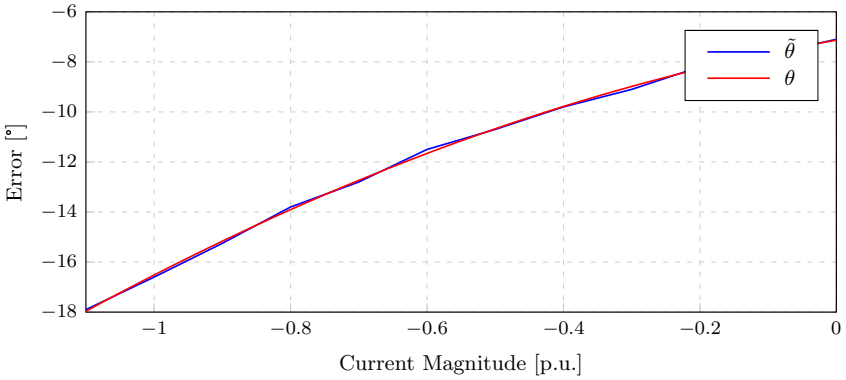

Figure 5.11: The negative current estimation error compensation curve for the arbitrary injection method.

Table 5.1: Arbitrary injection control variables

Variable	**Value**
K_P	110
K_I	16500
v_{inj}	200 V

5.7.2 Sensorless control

Stable sensorless control was achieved practically by slightly changing the AI PLL gains as well as increasing the injection voltage to those given in Table 5.1.

A sensorless AI locked-rotor rated-current control step measurement is shown in Figure 5.12. Note the close resemblance of the current response to that in the simulated result of Figure 5.8. Once again the high-frequency current component is visible. The current control is stable and fast, settling in about 2.5 ms. A relatively large estimation error jump is exhibited, but PLL remains synchronised and pulls the estimation back. Initially the current is at 0.3 p.u. resulting from the minimum amount of q-axis current in order to make the saliency 'visible'.

Measured sensorless speed control from standstill to low-speed at rated current is shown in Figure 5.13. It can be seen that the control is stable, although exhibiting some jittery behaviour. This can be attributed to unoptimised speed controller gains for this speed, as well as high-frequency oscillation in the estimated angle.

Figure 5.14 shows a sensorless no-load standstill to rated speed control step measurement. The speed control is stable with good position tracking. Evidently the speed response is much slower than the sensored result in chapter 3, but it was deemed sufficient for the purposes of this research. Note that initially the saturation current is negative, since a braking action was applied earlier. This is because the q-axis current changes sign for a change in stator current direction. A measurement error in the speed signal is also visible in die speed response.

In Figure 5.15 a sensorless standstill speed control measurement with a large load torque step applied is shown. It is evident that the sensorless speed controller has relatively good disturbance rejection and that even though a large error jump is created with the load step the control is stable and the PLL remains synchronised.

These results show the capability of the AI method for sensorless control of the RSM

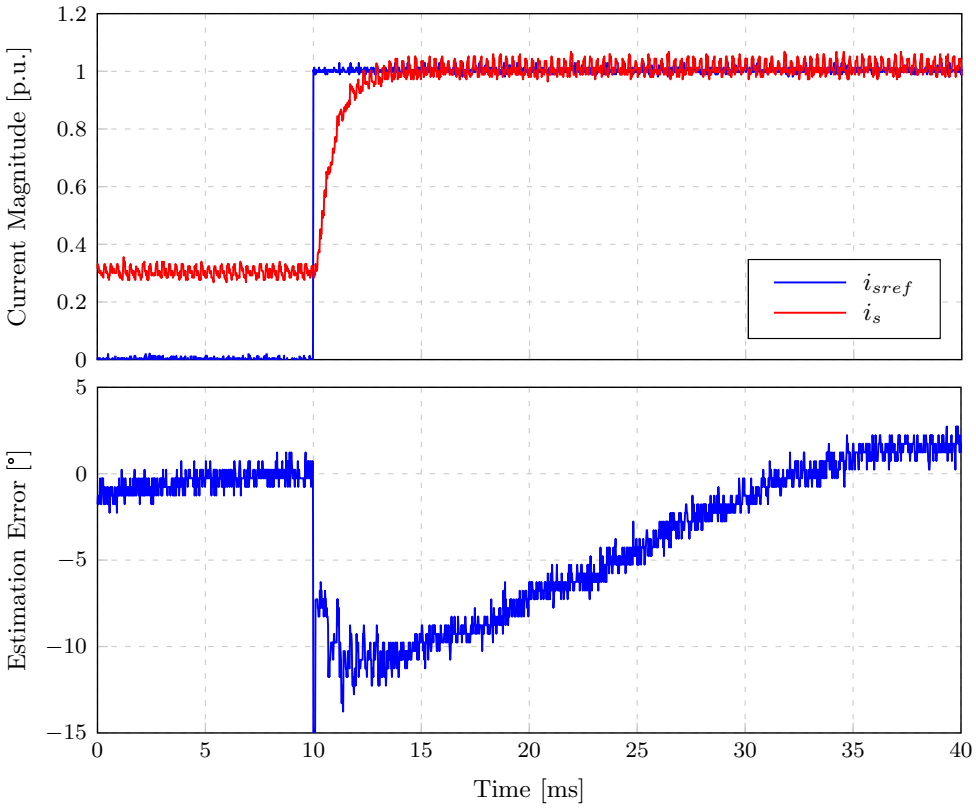

Figure 5.12: A measured sensorless rated-current control step measurement at standstill (locked rotor) using the arbitrary injection method plotting stator current and electrical angle estimation error versus time.

from standstill to low speeds. It will subsequently be implemented as part of a hybrid controller in chapter 6.

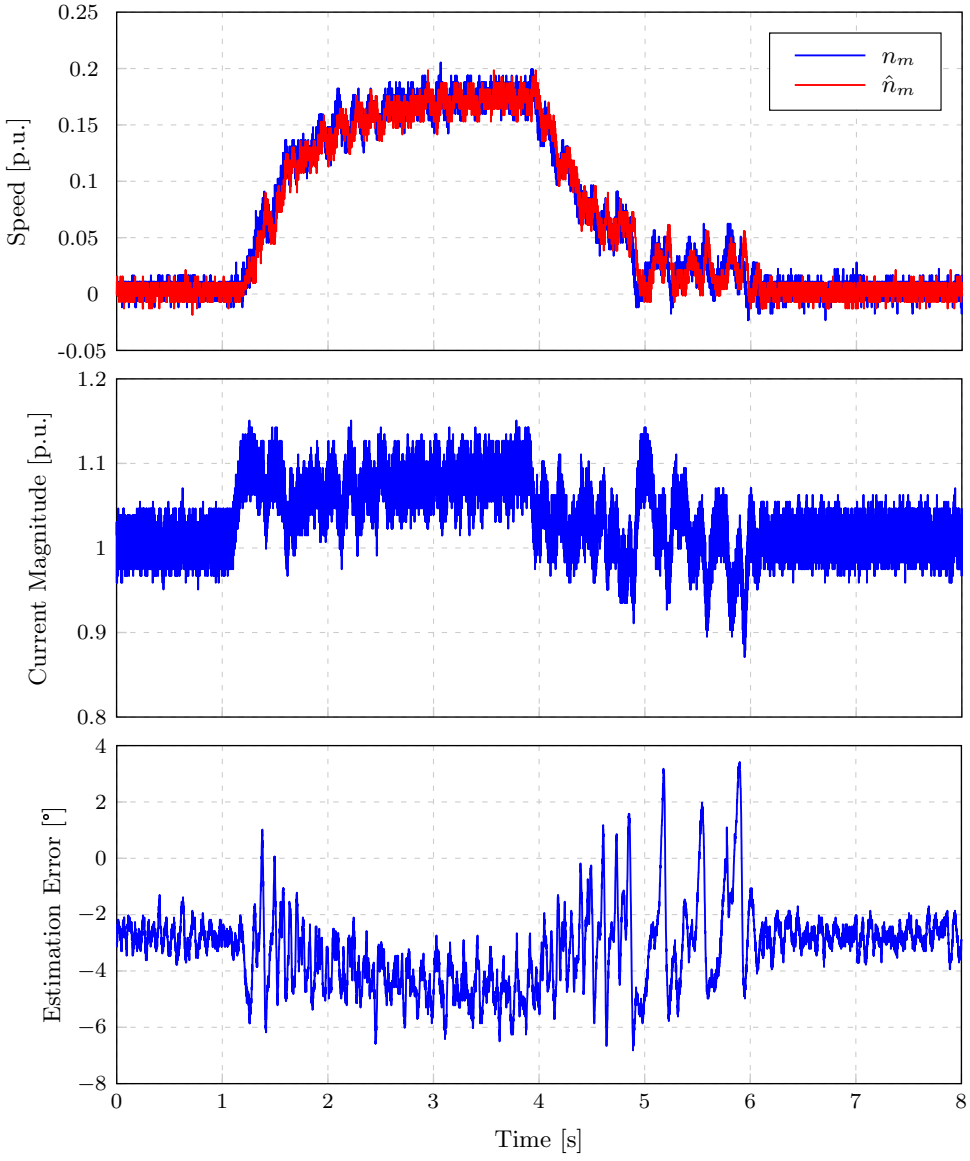

Figure 5.13: A measured rated load sensorless speed control step measurement from standstill to medium-speed using the arbitrary injection method plotting machine speed, stator current and estimation error versus time.

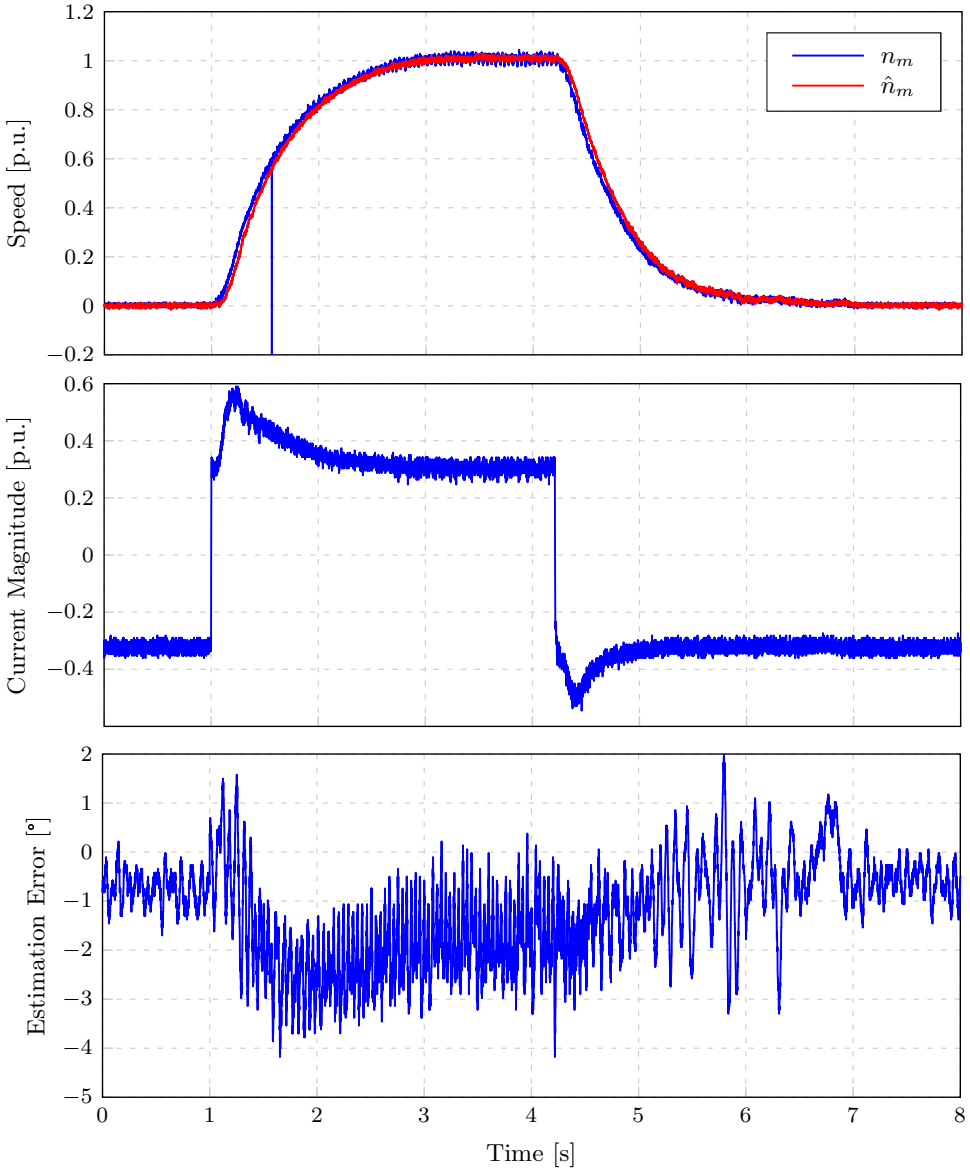

Figure 5.14: A measured sensorless speed control step measurement from standstill to rated-speed at no-load using the arbitrary injection method plotting machine speed, stator current and estimation error versus time.

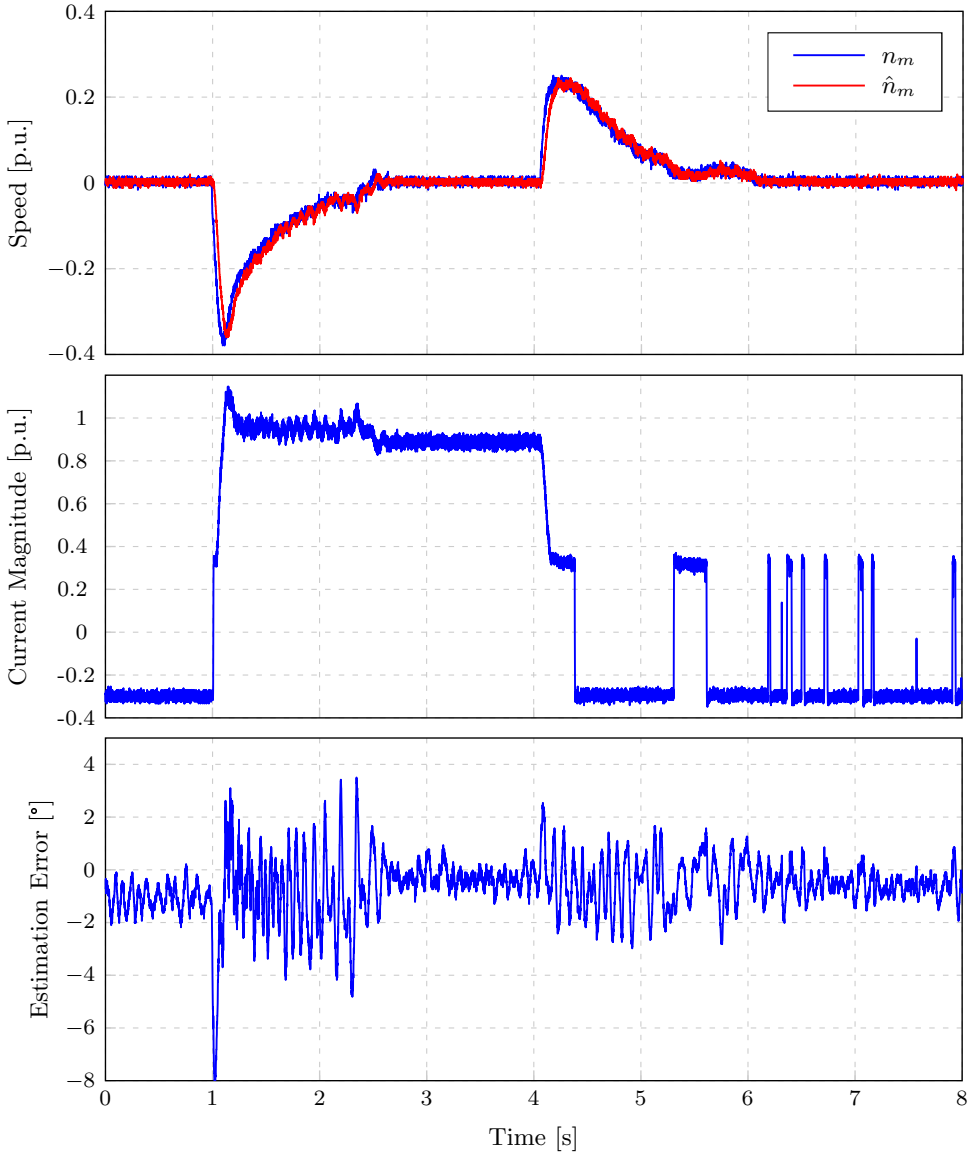

Figure 5.15: A measured sensorless load-step standstill speed control measurement using the arbitrary injection method plotting machine speed, stator current and estimation error versus time.

Chapter 6

Hybrid Position Sensorless Control

This chapter describes a hybrid active-flux (AF) and arbitrary injection (AI) position sensorless controller scheme derived to deliver stable control in the entire rated speed and load range of the RSM. The novel scheme derived is speed and load dependent owing to the requirements of the position estimation techniques implemented. It was presented at the symposium on power electronics, electrical drives and motion (SPEEDAM) 2014 in the Gulf of Naples, Italy in June of 2014 with paper title "*Hybrid Active-Flux and Arbitrary Injection Position Sensorless Control of Reluctance Synchronous Machines*" as published on IEEEXplore® (see [57]).

Considering the limitations of estimation experienced using the AF and AI methods in chapters 4 and 5 respectively it is clear that a combination of the methods could result in a position sensorless controller that is capable in the entire rated speed and load range. The AF method is capable of sensorless control from low speed up to rated speed (and beyond), requiring a minimum amount of d-axis current in the machine as in (4.3.1) in order for the machine flux-linkage to be present. The AI method is capable of sensorless control from standstill to rated speed, but fails above low speeds under load conditions. The AI method requires a minimum amount of q-axis current in order to make the inductance saliency visible as in (5.5.1). With these limitations in consideration a hybrid scheme is derived with efficiency, stability and reliability as main requirements.

The hybrid controller scheme is distinguished from the work presented in [30, 32, 51], since the axially laminated anisotropic RSM in [30] has inherent saliency without the presence of q-axis current (as opposed to the normal transverse laminated rotor RSM with punched rotor flux barriers used herein). The fundamental saliency technique used in [32] (for higher speeds) requires the presence of q-axis current - coinciding with the high-frequency injection technique used. Lastly, the control scheme in [51] is implemented on an interior permanent magnet synchronous machine - allowing constant d-axis current for active-flux.

6.1 Hybrid Scheme

In order to maintain close to maximum efficiency by implementing CCAC the AF method cannot be implemented at zero load in combination with the AI method. With the required minimum amount of d- and q-axis currents for AF and AI respectively, fulfilling both requirements simultaneously would constitute a torque producing current with d- and q-axis components. Therefore the hybrid scheme derived only switches to the AF estimator under load conditions (implementing CCAC) with a minimum amount d-axis

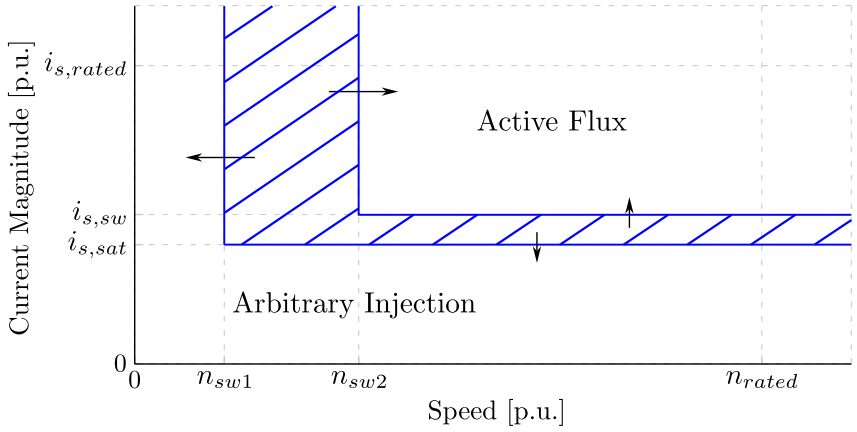

Figure 6.1: The hybrid controller scheme operating regions with the highlighted hysteresis region in blue.

current present in the machine.

Obviously the AF method is only functional above a certain operating speed and thus AI is implemented under all load conditions under the chosen operating speed. Since operating at a certain speed/load operating point is never perfectly constant (with no fluctuation) a hysteresis buffer is added in the load and speed ranges to eliminate repetitive back and forth switching between estimation algorithms. Switching from AI to AF requires a higher machine speed than what the AF method is capable at, because PLL synchronisation is slower at low speeds. Once the PLL is synchronised sensorless control implementing AF can be done at a much lower speed. This difference in speed-points creates a natural hysteresis band for speed switch-over.

Figure 6.1 shows the current load versus speed plot for the sensorless control scheme. The blue lines highlight the hysteresis region and switching between estimation techniques only occurs on the hysteresis region borders in the directions shown by the arrows. A state machine representation of the hybrid controller scheme is shown in Figure 6.2. It can be seen that switching occurs as specified earlier and that at switch-over the electrical angle is kept equal to the estimated angle of the previous state followed by a time delay of one switching cycle $\Delta t = T_s$ which allows for initial PLL synchronisation. It is also shown that the PLL estimated speed of the inactive estimator is kept equal to the active state's estimated speed in order to keep the inactive PLL close to synchronisation (see Figure 4.2). At switching from AF to AI the AI estimated angle is set equal to the AF angle ($\theta_{AI} = \theta_{AF}$) in order to further assist initial PLL synchronisation. It is assumed that control starts with the machine at standstill or at least $\omega < \omega_{sw1}$ for the purpose of the state machine representation.

6.2 Considerations for implementation

It was decided to not first test the hybrid scheme using the simulation model, because the individual controller schemes had both been practically tested and shown to be working. Initial testing was done by operating the hybrid estimator only as an observer and not using the estimated angle as part of the closed-loop controller. This allowed investigation into switching dynamics and PLL synchronisation characteristics. Subsequent practical testing showed that stable observer behaviour during switching did not necessarily relate to stable closed-loop sensorless control and further tuning and changes was needed to

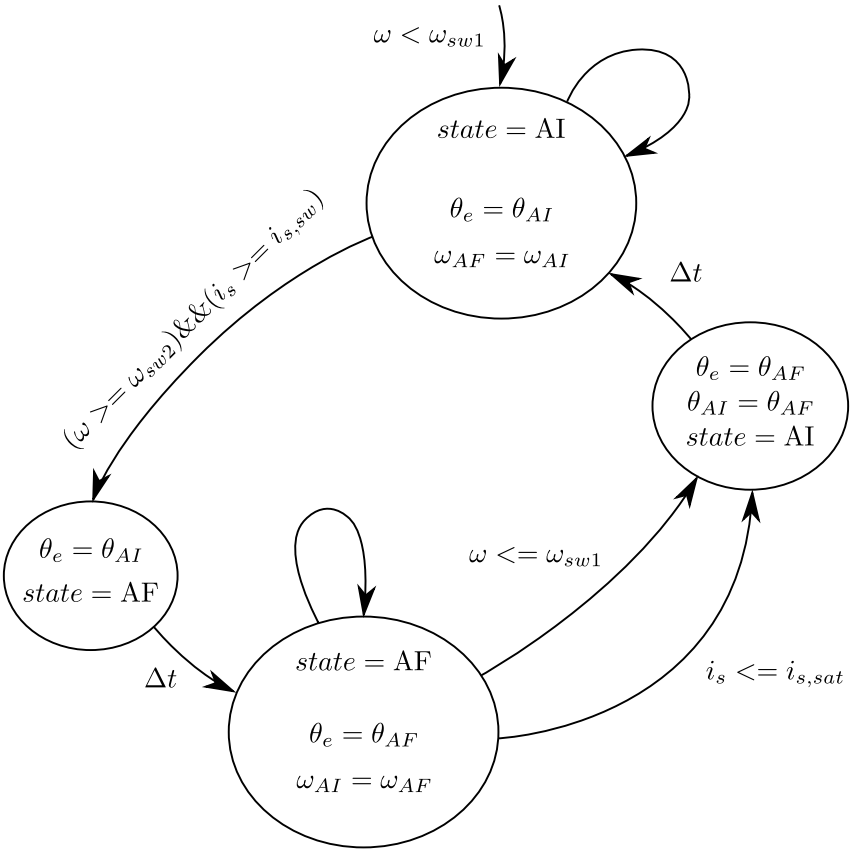

Figure 6.2: The state machine diagram of the hybrid controller scheme.

deliver the stable hybrid sensorless controller scheme.

Since a faster AF PLL would allow lower synchronisation speeds testing was done to increase the AF PLL gain in the positive current region. It was found that inherent instability in the AF estimation scheme inhibited an increase in PLL gain for positive current, because the higher the PLL gain is selected the higher the minimum stability speed, n_{sw1}, of the closed loop AF PSC becomes. In contrast the higher the PLL gains are the lower the AF PSC minimum entry speed, n_{sw2}, becomes. It was decided to choose the minimum stability speed as low as possible and increase the PLL gains as much as possible while maintaining stability at this speed. This choice is motivated by the idea that a typical industrial application for the RSM drive is fans and pumps - which would normally operate above a minimum speed at some load. Considering this PSC could mostly be done in the AF region once that has been entered if the minimum stability speed is low enough. This minimum stability speed was thus chosen as $n_{sw1} = 200$ r/min. It was found that the AF PLL integrator could be sped up a bit, without loss of stability, to result in a final gain of $K_{I,AF} = 6240$. This gain allowed a minimum AF synchronisation speed of $n_{sw2} = 500$ r/min. The AF estimator is preferred because of no additional voltage is applied to the machine so that audible noise and torque ripple is minimised. For better stability when switching back to the AI region, the AI PLL gains were also slightly changed. The final switching intervals and controller gains are listed in Table 6.1.

Table 6.1: Hybrid controller switching intervals and gains

Variable	Value	Per Unit
n_{sw1}	200 r/min	0.133 p.u.
n_{sw2}	500 r/min	0.333 p.u.
$i_{s,sat}$	2 A	0.4 p.u.
$i_{s,sw}$	2.5 A	0.5 p.u.
$K_{P,AF}$	240	
$K_{I,AF}$	6240	
$K_{P,AI}$	60	
$K_{I,AI}$	9600	

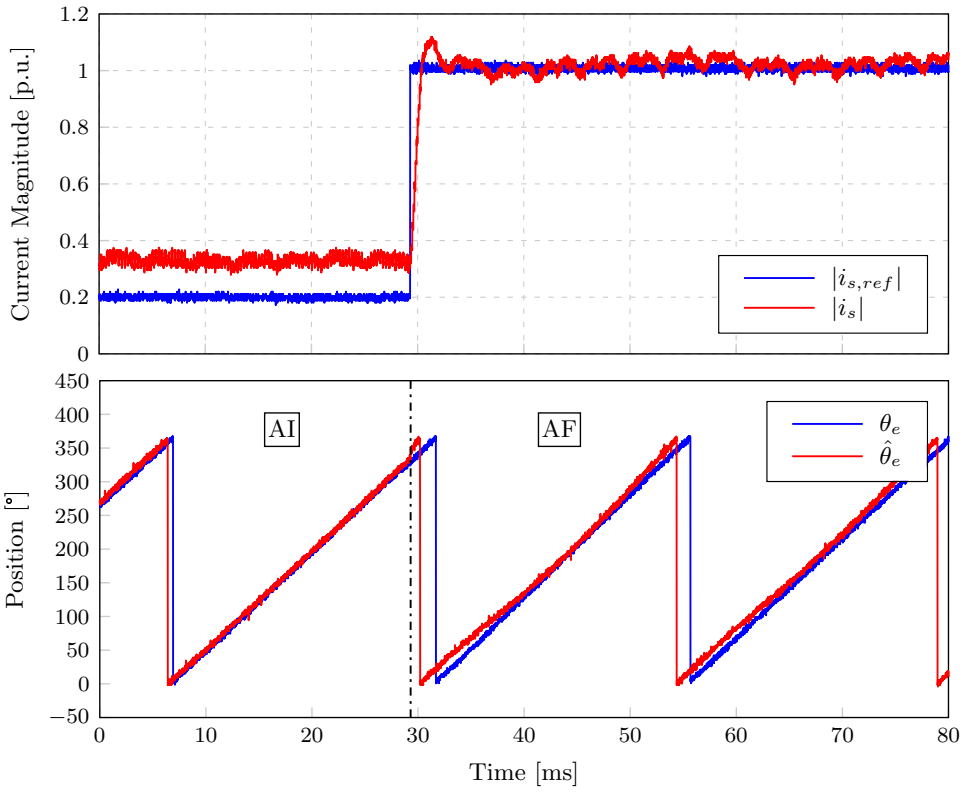

Figure 6.3: A measured sensorless rated-current control step at rated-speed using the hybrid scheme plotting stator current and electrical angle versus time.

6.3 Practical Results

Measured results in this section regularly refers to the active-flux (AF) and arbitrary injection (AI) position sensorless control schemes where they are being implemented in the hybrid controller.

Stable sensorless current control from 0.2 p.u. to rated current at rated-speed is shown in Figure 6.3. It is evident that the current control is very fast and stable. Note that the estimated electrical angle signal plotted is the uncompensated version, in order to show the difference with the actual angle. Once again the minimum q-axis saturation current is visible before the load step.

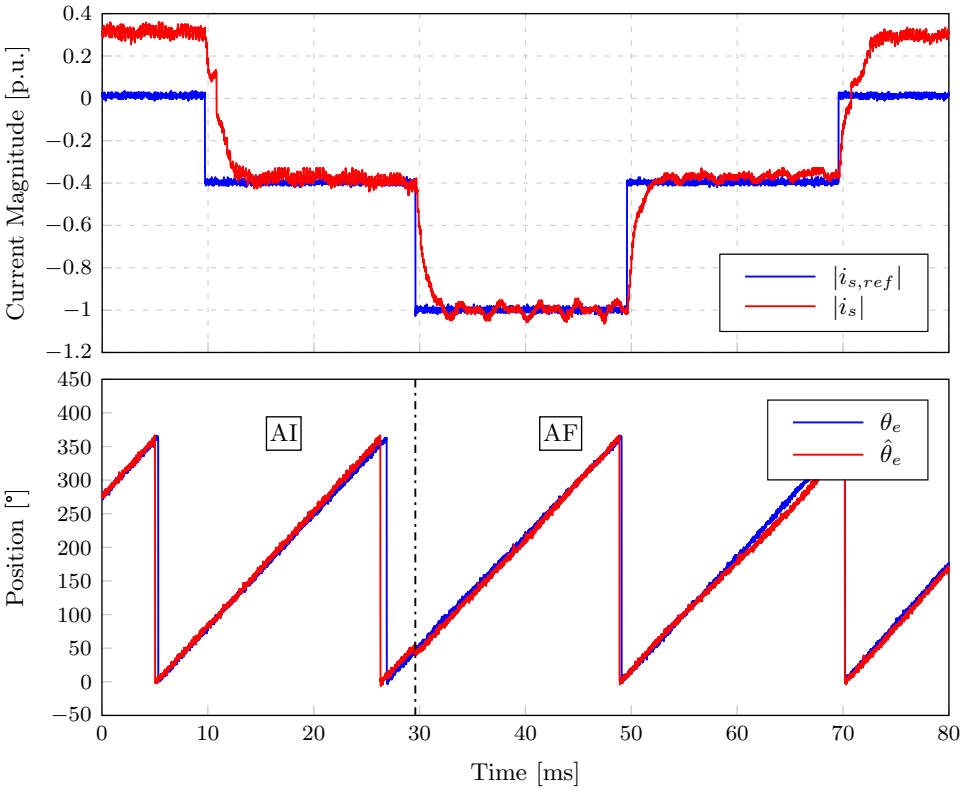

Figure 6.4: A sensorless generator rated-current control step measurement at rated-speed using the hybrid scheme plotting stator current and electrical angle versus time.

Sensorless current control in generator mode is shown in Figure 6.4. The current reference first steps into the hysteresis region, showing that the active PSC method stays in control. Then a large step up to rated negative current in applied followed by another step into the hysteresis region, once again remaining in the active controller scheme. It can be seen that the current control is stable and fast.

A sensorless current control measurement with various jumps across the hysteresis region is shown in Figure 6.5. Evidently the sensorless current controller remains stable and the hybrid scheme switches reliable between the two estimators.

A full-load sensorless standstill to rated-speed control step is shown in Figure 6.6. The PSC starts in the AI region and switches over to AF when crossing n_{sw1}. A load-step is applied around 9.5 s which is followed by speed control back to standstill. During deceleration the PSC switches back to AI when crossing n_{sw2}. The large speed and position estimation error oscillations is attributed to unoptimised speed controllers for low speed. Sensorless speed control above rated current is showcased in this result.

Measured generator sensorless speed control at rated-current is shown in Figure 6.7. Note that the control is stable and sensorless rated-speed control at rated negative-current is shown. The large estimation error in the AF region is deliberately made so in order to show the stability of the AF controller, as long as the estimation error is negative (estimated angle leads the actual angle). This is also the cause of the slight speed jump when switching from AI to AF.

A measured load-step across the hysteresis region under sensorless generator rated-speed control is shown in Figure 6.8. Evidently the PSC scheme switches reliably between the estimation schemes.

A sensorless speed control measurement showing the stability of the speed hysteresis

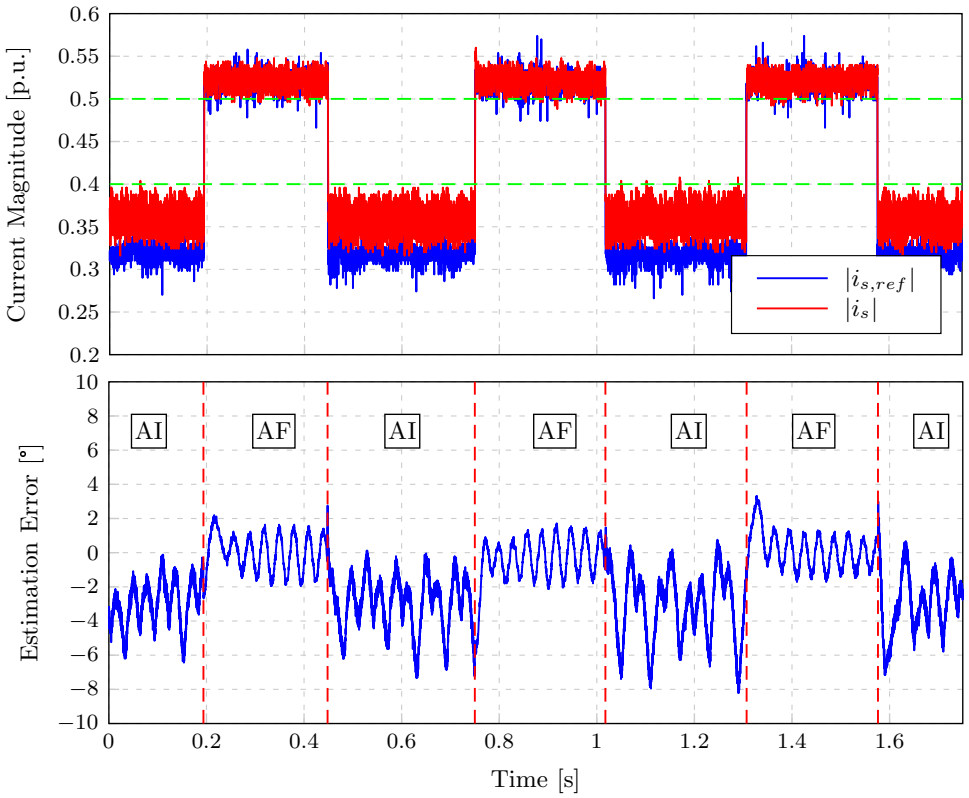

Figure 6.5: A sensorless current control measurement at rated-speed across the hysteresis region using the hybrid scheme plotting stator current and electrical angle estimation error versus time.

control is shown in Figure 6.9. PSC starts in the AI hysteresis region and switches to the AF region after a load step. This is followed by a few speed control steps across the hysteresis region to show the stability of the speed controller. Finally the load is removed at speed and AI is re-entered. The points marked on the figure can be matched with Figure 6.10.

With these measured results it can be concluded that the hybrid control scheme can deliver stable sensorless control of the RSM in the entire rated load and speed range, with some limitations of dynamics.

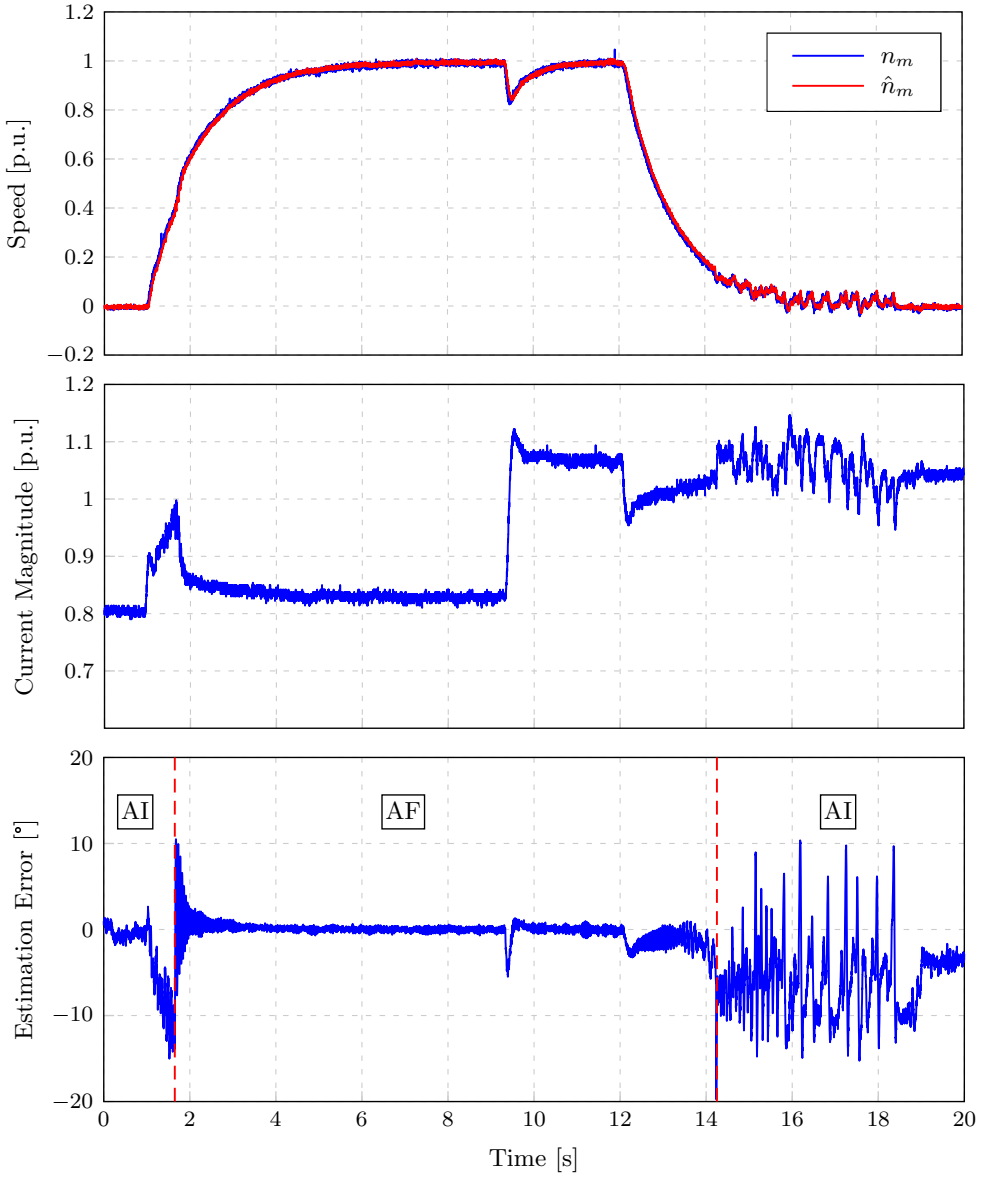

Figure 6.6: A measured rated load sensorless speed control step from standstill to rated-speed using the hybrid scheme plotting machine speed, stator current and estimation error versus time.

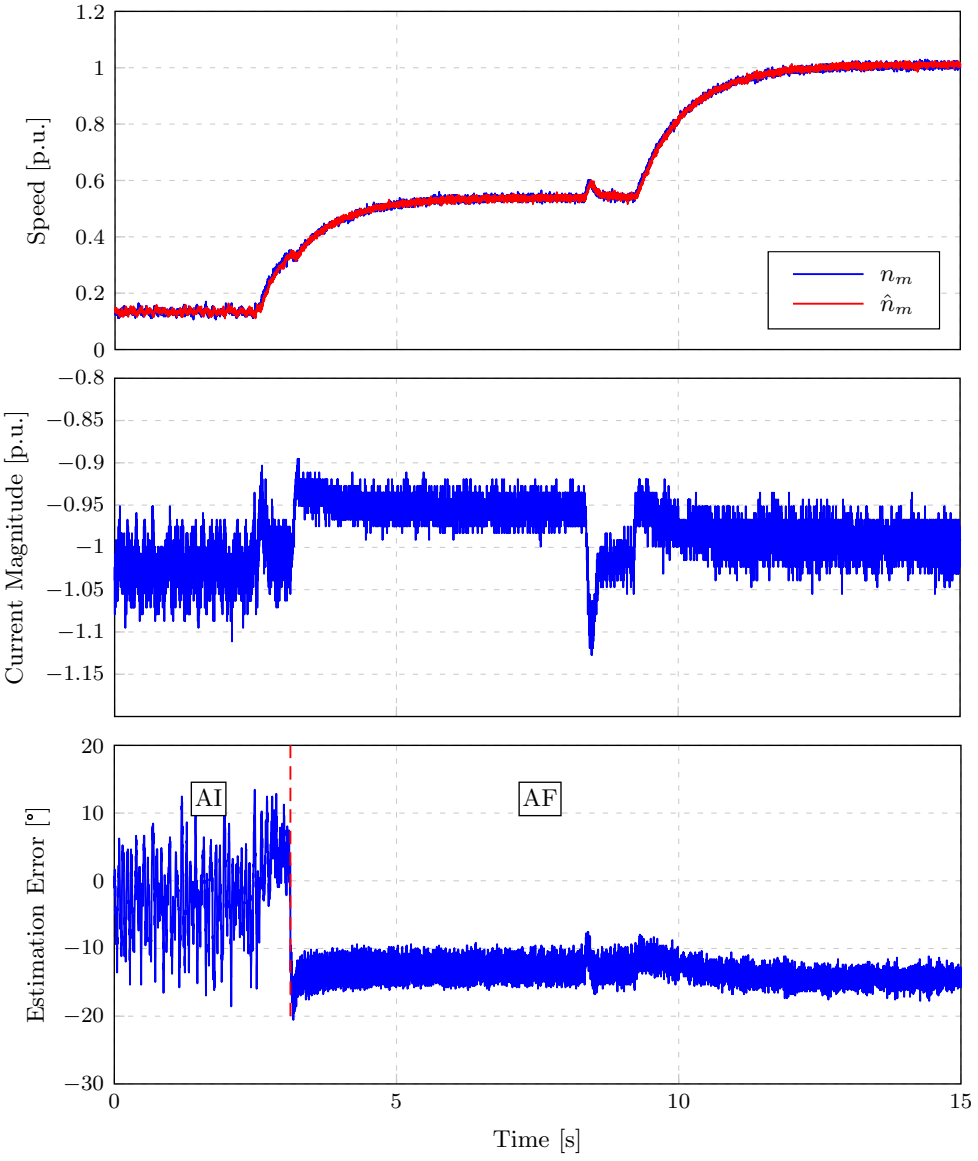

Figure 6.7: A measured sensorless generator speed control step from standstill to rated-speed using the hybrid scheme plotting machine speed, stator current and estimation error versus time.

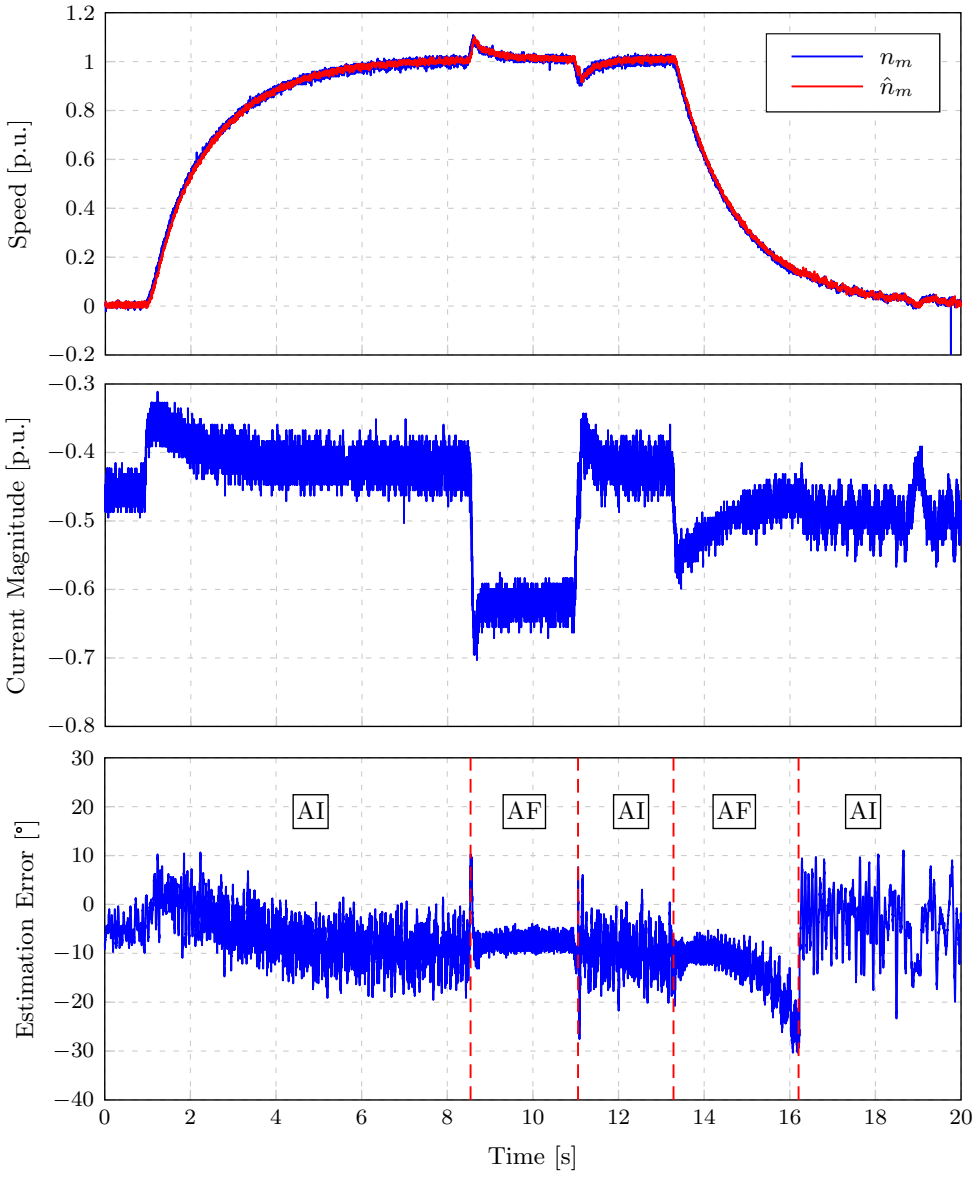

Figure 6.8: A measured sensorless generator speed control step from standstill to rated-speed with a load-step using the hybrid scheme plotting machine speed, stator current and estimation error versus time.

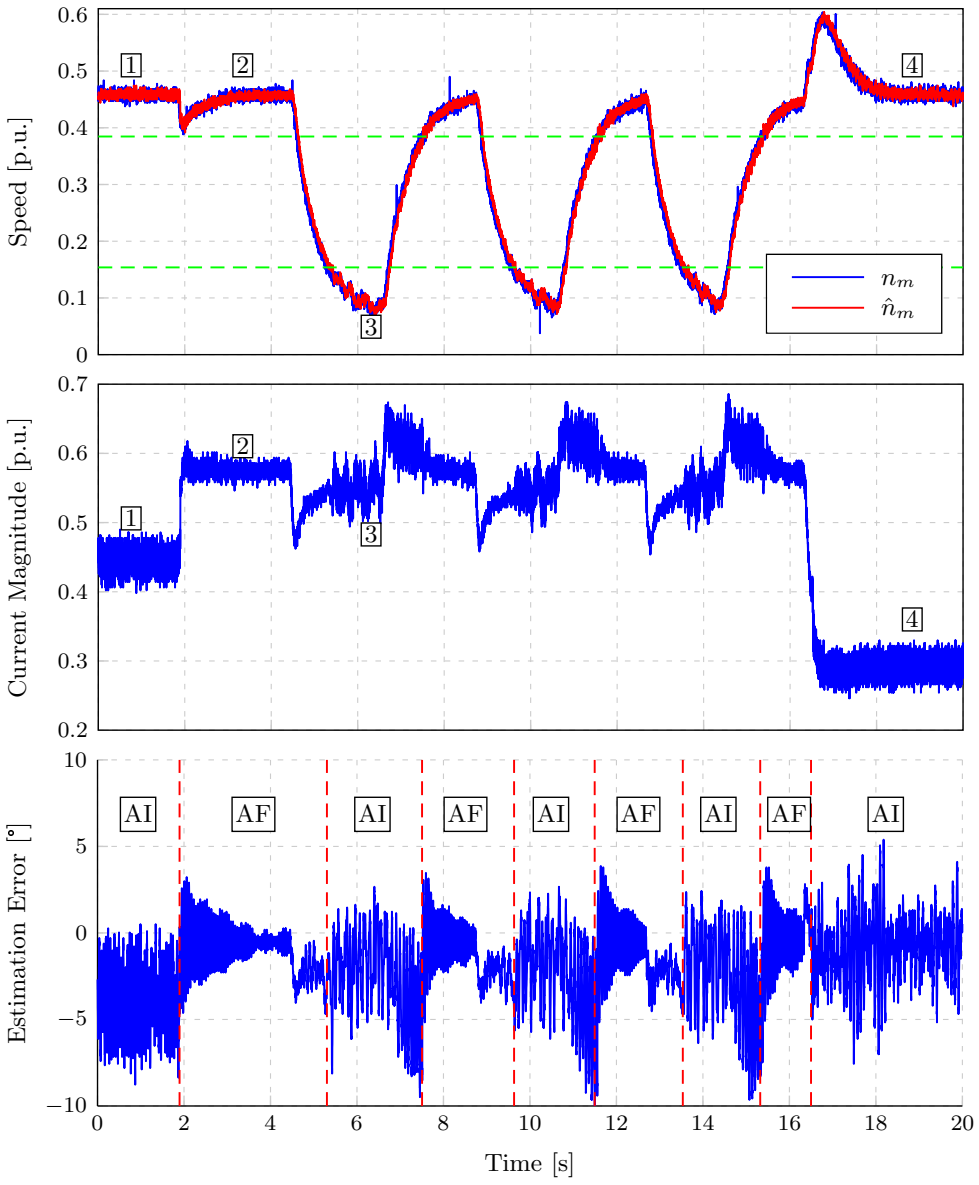

Figure 6.9: A sensorless speed control measurement across the hysteresis region using the hybrid scheme plotting machine speed, stator current and estimation error versus time.

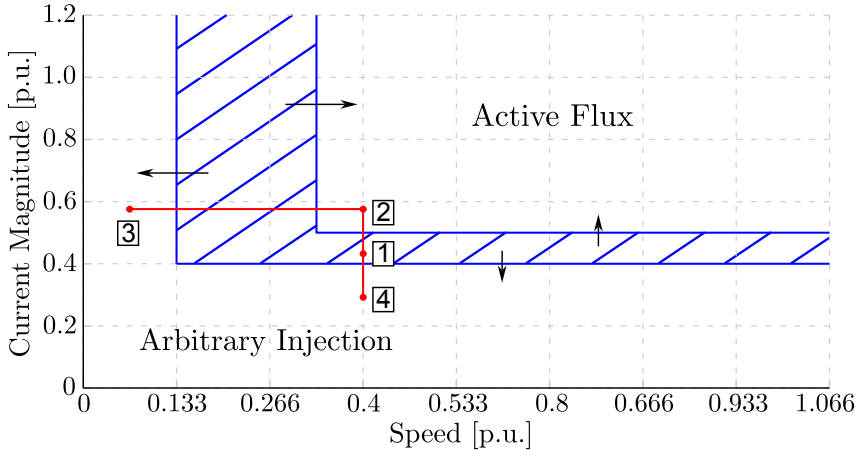

Figure 6.10: The noted hybrid speed control measurement operating points around the hysteresis region from the result in Figure 6.9.

Chapter 7

Assisted Fundamental Model Position Sensorless Control

This chapter contains a brief overview of the problems and limitations experienced with the hybrid controller scheme and motivates the research of assisted fundamental model position estimation. The ideas, problems, methodologies and results found in terms of this type of hybrid scheme are given and discussed.

As found in chapter 6 the hybrid controller scheme has some drawbacks in terms of stability. This revolves around the switch-over between two estimation schemes. It can be seen from the results in section 6.3 that the largest estimation error oscillations occur when switching specifically from the saliency based method to the fundamental model based method with a large initial estimation error and subsequent time for stabilizing the fundamental model controller. After this stabilization it is evident that the fundamental model technique has a much lower error oscillation than the saliency based technique and behaves in a very stable manner. Considering that it would be beneficial to have the fundamental model technique in control at all times and correct its estimation error in the lower speed range in some way.

In [58] and [59] among others adaptive fundamental model techniques combined with a high-frequency injection technique for PMSM drives are proposed. These fundamental model techniques are based in the rotor reference frame and thus contain the speed voltage term in the voltage equations as in (2.1.9). This speed voltage is assisted at low speed and standstill using the estimated speed term from a saliency based technique to result in a fundamental model technique that is capable of control in the entire rated speed range. With careful consideration it is found that both estimation schemes are active in the low speed region but that the assisted fundamental model scheme is always in control which eliminates the hybrid controller switch-over problem as highlighted earlier. Since both estimation techniques are active at a certain stage they should both be capable of estimation while the other method is in control (at least in that region) - which especially has implications for an injection voltage dependent scheme. Considering the methods explained in chapters 4 and 5 we find that these schemes are not suited for such a combined observer. Evident from the load-dependent scheme derived in chapter 6 the AF method does not function down to zero load, because it requires the minimum amount of d-axis saturation current (see section 4.3.1). Therefore the AF estimator cannot even be assisted using a saliency based technique, because its PLL is out of sync with a very low-magnitude vector. Also, the AI method requires q-axis current in the machine in order to make the saliency visible, so that combining that with the d-axis current required by the AF method would result in a torque producing current vector, even though the reference current may

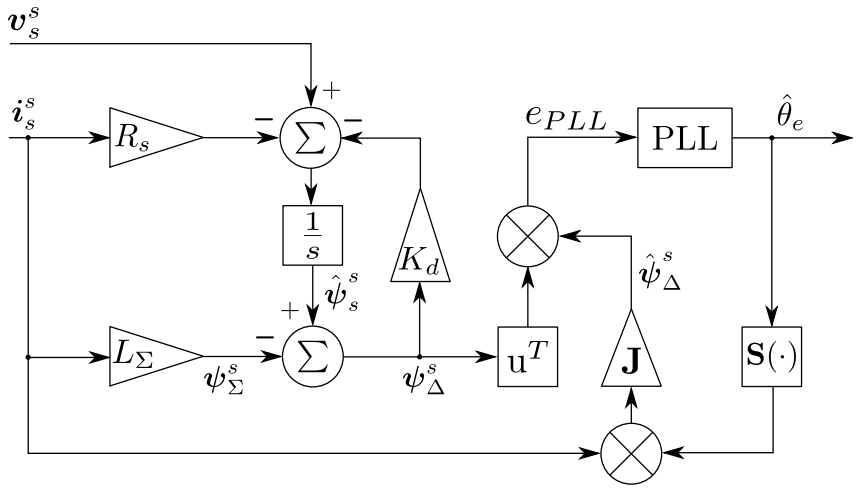

Figure 7.1: The FS position estimation scheme block diagram.

be zero. This motivates the use of a different fundamental model technique that requires the same q-axis current (or no current for that matter) to be present as required by the AI method. Note that the research presented in [30] is applied to an ALA RSM that exhibits visible saliency in the machine without the presence of any current. Therefore the methods are capable of accurate concurrent estimation.

The fundamental saliency based position estimation scheme for a RSM as presented in [20] and discussed in detail in [33] requires q-axis current to be present in order to make the machine saliency visible and is investigated for use as part of an assisted fundamental model (AFM) PSC scheme.

7.1 Assisted Fundamental Saliency based Estimator

Using the fundamental saliency (FS) based estimation scheme one finds once again that at lower speed the estimated error angle increases up to instability. It is then motivated to implement the AI method at lower speeds and standstill in order to assist the fundamental model scheme which is in control. As discussed earlier the AFM schemes are augmented using the speed term from a saliency based technique in order to correct the speed voltage term as part of the machine voltage model. A block digram representation of the FS scheme is shown in Figure 7.1. The integration feedback gain K_d is required for integration drift compensation similar to the AF method. The FS scheme is based in the stator reference frame and therefore has voltage equations that do not contain the speed voltage terms as in (2.1.2).

The PLL error of the FS based estimation scheme is

$$e_{PLL} = {\boldsymbol{\psi}_\Delta^s}^T \mathbf{J} . \hat{\boldsymbol{\psi}}_\Delta^s \tag{7.1.1}$$

$$= \left(\int (\boldsymbol{v}_s^s - R_s \boldsymbol{i}_s^s).dt - \boldsymbol{\psi}_\Sigma^s \right)^T \mathbf{J} . \mathbf{S}(\theta_e) \boldsymbol{i}_s^s \tag{7.1.2}$$

as taken from [20]. Of note is the fundamental salient component of stator flux, $\boldsymbol{\psi}_\Delta^s$, and the rotating matrix $\mathbf{S}(\theta_e)$ as defined in (5.1.11). As mentioned the equation is in stator reference frame and contains no speed term that can be assisted. One might be motivated to use the rotation matrix for assistance by substituting the feedback estimated electrical angle from the FS PLL (as seen in Figure 7.1) with the estimated angle from the AI

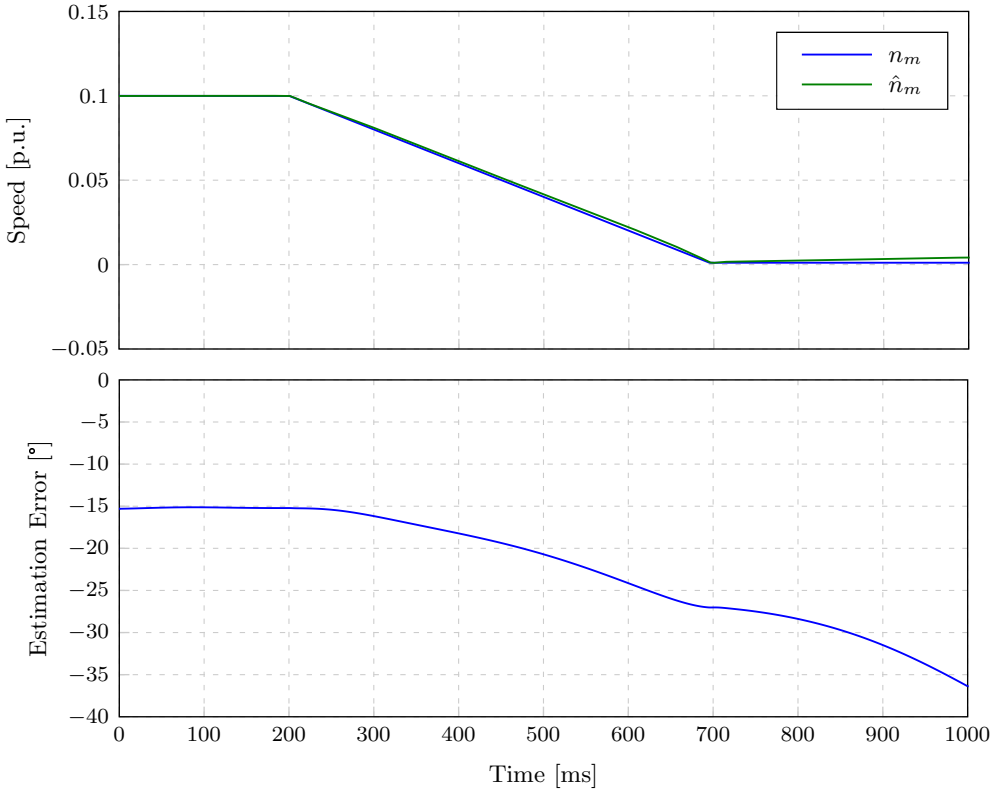

Figure 7.2: A rated-current control simulation from low speed to standstill implementing the FS method as observer plotting machine speed and electrical angle estimation error versus time.

method, but it was found that this does not work since it breaks the PLL of the FS method causing instability. The idea of the assisted scheme is to re-align the estimated flux vector with the actual stator flux vector by normally adding speed information the fundamental model. Without the speed voltage term it is decided to assist the FS model by transforming the FS flux vector, $\hat{\boldsymbol{\psi}}_s^s$, to the rotor reference (d/q) frame using the estimated angle of the FS scheme and then to transform it back to the stator reference (α/β) frame using the estimated angle of the AI scheme. This has the effect of rotating the estimated flux vector to the position estimated by the AI method.

7.2 Simulation Results

It was found that by assisting the FS method in the way mentioned by aligning the estimated flux vector using the estimated AI angle resulted in an improved FS estimation error at lower speeds, but it was still unstable at zero and very low speeds.

A comparison of the observer estimation error simulation results in Figures 7.2 and 7.3 shows how the assisted FS scheme is improved. The unassisted FS observer scheme makes a 15° estimation error at low speed (0.1 p.u.) which increases to about 27° at zero speed as seen in Figure 7.2. At standstill the estimation error does not stabilise at a specific point and the observer loses position tracking, also evident from the speed estimation, $\hat{n}_m$, which moves away from the actual speed at standstill.

The assisted FS observer scheme simulation result at the same speeds shown in Figure 7.3 has a much smaller estimation error of about 5.5° to 14°. This result proves that

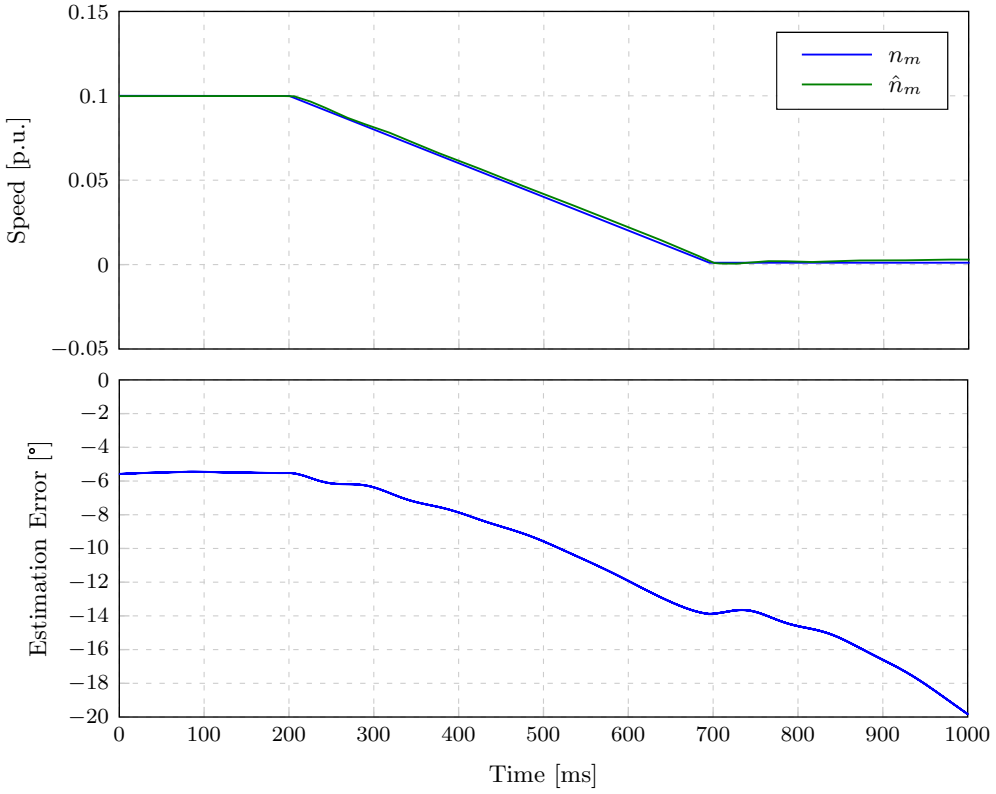

Figure 7.3: A rated-current control simulation from low speed to standstill implementing the AI assisted FS method as observer plotting machine speed and electrical angle estimation error versus time.

the AI assistance does indeed improve the FS scheme estimation error, but the observer is still incapable at zero speed since the error does not stabilise.

From these results it is evident that further work is required to stabilise the AI assisted FS estimation scheme in order to allow closed-loop sensorless control in the entire rated speed range.

Chapter 8

Conclusions and Recommendations

The transverse-laminated rotor reluctance synchronous machine with punched rotor flux barriers was investigated for position sensorless control. This machine is very robust and simple to manufacture, with multiple application possibilities in industry. Reluctance synchronous machine variable speed drives are shown to have 10-15% better efficiency than their induction machine counterparts. Efficient closed-loop control of the machine requires position information normally supplied by a hardware sensor. These sensors are usually unreliable, justifying the use of position estimation for control.

Practical testing of the control techniques was done using a rapid prototyping system that was completed before testing. This system is found to be very beneficial for rapid machine control system research since it is very modular. The control algorithms are implemented easily in C-code and any control variables can be viewed on the fly for investigation into the controller state and behaviour.

Position estimation of AC machines is identified as a mature field of research with ample publication outputs in this field since the mainstream commercialisation of powerful digital computation systems in recent years. Position sensorless techniques for the RSM are identified as mainly fundamental model and saliency based techniques. Fundamental model techniques are capable of stable position sensorless control from low- to rated-speeds while saliency based signal injection techniques allow position sensorless control from standstill to medium speeds. Considering the strengths and drawbacks of these techniques it is noted that the combination of these techniques in hybrid controllers could result in sensorless control capabilities in the entire rated (and extended) speed range.

The active-flux (AF) method is investigated as a fundamental model position sensorless control scheme of, the transverse laminated reluctance synchronous machine in this research for the first time to the authors knowledge. In addition to that the control scheme is implemented using constant current angle control to achieve close to maximum efficiency, which is one of the main motivations for considering the reluctance synchronous machine, other than the published applications of this method. It is found that implementing the AF method on a transverse laminated reluctance synchronous machine with multiple flux barriers has a few distinct implications, also considering generator mode control of the machine. The estimation scheme is adapted to function correctly for the investigated machine, and stable position sensorless control from low- to rated speed in the entire rated load range is shown. An additional motivation for considering the AF-method is eventually delivering a unified sensorless controller scheme for any synchronous machine, but it was found that with the extensive amount of intrinsic tuning required to get the closed-loop active-flux sensorless controller working, this would not be a natural follow-up.

For position estimation below low speed the arbitrary injection (AI) method is investigated again. This saliency based signal injection method is shown to be completely parameter independent, requiring only the presence of a current progression at every calculation step. A minimum amount of quadrature-axis current is required to make the saliency visible for the investigated machine. The estimation scheme is shown to be capable of position sensorless control of the investigated machine in the entire rated speed range, with torque capability limitations at higher speeds caused by saliency shift.

A hybrid controller scheme is derived with a new speed- and load-dependent approach in order to enable combination of the active-flux (AF) and arbitrary injection (AI) methods. The requirements for this hybrid controller are distinguished from other investigated hybrid control schemes in a number of ways. It was determined that under maximum torque per ampere control the AF method could only be implemented in the low- to high-speed range at load. The AI method maintains control in all other operating conditions. A speed- and current-hysteresis region is implemented in order to eliminate constant switching between estimation schemes at a specific working point. It is shown that the derived hybrid scheme allows position sensorless control of the investigated machine in the entire rated speed- and load-range (with some limitation on dynamics compared to sensored control), including negative i_q currents for generator action.

Because of the limitations of the hybrid controller scheme implemented, an assisted fundamental model scheme is investigated. This is motivated by implementing a fundamental model estimation technique in the entire operating region, but assisted by a saliency based technique (capable of sensorless control at standstill) in low speed and standstill operating conditions. This would eliminate discrete switching between estimation schemes, allowing completely smooth sensorless control in the entire rated speed range. The fundamental saliency (FS) technique was investigated for combination with the arbitrary injection (AI) method. This method is considered more applicable to an assisted scheme combined with the AI method since it has similar current requirements for estimation. It was found however that using the assisting angle as part of the estimation scheme was unstable and subsequent simulations aligning the FS flux vector with the estimated AI angle only allowed estimation improvements, but was not capable of sensorless control at standstill.

8.1 Contributions

- The active-flux (AF) method was implemented on a transverse-laminated RSM for the first time in this study and research.
- It is found that with maximum torque per ampere control (constant current angle) the AF position estimation scheme cannot be used at zero or low loads, since it requires direct-axis flux-linkage to be present in the machine. This distinguishes the AF method from the fundamental saliency (FS) method that requires a minimum amount of quadrature-axis current in the machine (which becomes very small with good machine saliency).
- It is found that the AF compensation voltage behaves drastically different for generator mode and requires extensive gain compensation.
- It is found that the AF method has less than ideal dynamics when implementing a standard PI-based PLL.

- It is found that the arbitrary injection (AI) method is capable of position estimation up to rated speed, but with torque limitations above low speeds caused by saliency shift.
- A novel speed and load dependent scheme is derived to enable the first combination of the AI and AF methods in a hybrid sensorless controller scheme.
- The rapid prototyping system (RPS) was completed and is used in the Stellenbosch University Electrical Machines lab for machine testing.

8.2 Recommendations

In consideration of the results found and conclusions drawn in this thesis the author makes the following recommendations:

- It is the opinion of the author that for dynamic and stable position sensorless control of the transverse laminated reluctance synchronous machine implementing maximum torque per ampere control the hybrid high-frequency injection (HFI) and fundamental saliency (FS) based scheme published in [33] should be used.
- Stator resistance adaptation could be implemented as in [25] to improve the estimation error resulting from fundamental model schemes. Even though the active-flux (AF) compensation voltage allows for changes in the actual machine stator resistance, an estimated value closer to the actual value would improve the AF estimation.
- To improve errors at high speed under extended loads (saturation) for the AF method the limited SVPWM voltage magnitudes could be exported from the SVPWM algorithm and implemented in the AF estimation algorithm. See the vector limit block in Figure D.4 as well as the explanation in subsection 4.3.3.
- Further research on the AF method should include the investigation of discrepancies between simulation results and measured results for AF, considering implementation of the compensation voltage.
- To improve estimator dynamics during speed transients a mechanical model based PLL could be implemented for the AF scheme as in [30].
- Further research into an assisted fundamental model scheme should focus on techniques based in the d/q-reference frame as explained in chapter 7. This would allow assisting the fundamental model technique with an estimated speed term from a saliency based estimation technique at standstill and low speeds.
- The rapid prototyping system (RPS) state machine behaviour could be made less tedious by returning to the PC_EN state instead of the IDLE state on receipt of the CTRL_EN_marker when in the CTRL_EN state. See Figure 3.5 and the explanation in subsection 3.2.2.

Appendix A

Reference Frame Transformations

In order to simplify the analysis and control of some machines, the mathematical quantities are transformed to different reference frames. The $dq0$-reference frame used in this thesis is a two-axis reference frame rotating at synchronous angular velocity. This reference frame greatly simplifies equations which are functions of angular frequency, since the reference frame rotates at exactly this frequency. In this thesis the $dq0$-reference frame is also referred to as the rotor fixed reference frame, since it rotates with the rotor. The d-axis is defined to be aligned with the a-phase axis with zero angle θ whereas the q-axis is defined to be $\frac{\pi}{2}$ radians in front of the d-axis. The $\alpha\beta\gamma$-reference frame is a two-axis stationary reference frame employed to simplify the analysis of three-phase circuits also referred to in this thesis as the stator fixed reference frame. The α-axis is defined to be aligned with the a-phase axis and the β-axis $\frac{\pi}{2}$ radians in front of the α-axis. For comparison and clarity the $dq0$- and $\alpha\beta0$-reference frames are shown in Figure A.1.

Transforming instantaneous quantities from the stator phase axis abc to the stator

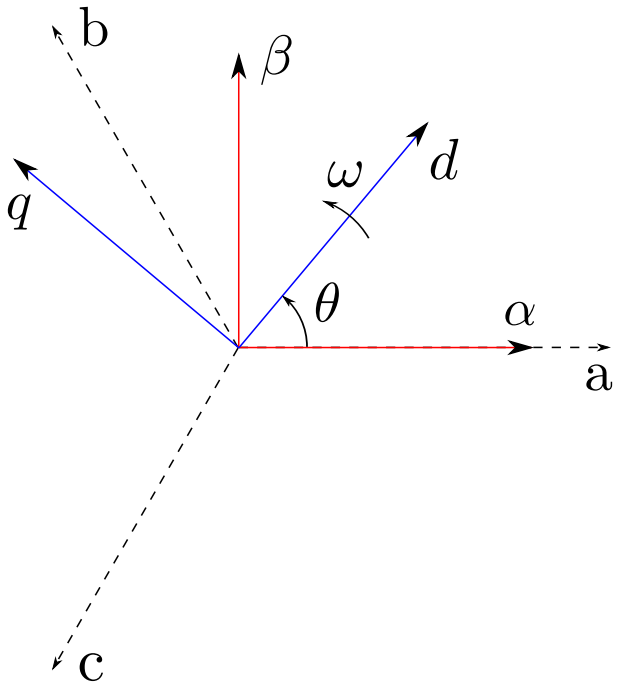

Figure A.1: The two-axis $dq0$- and $\alpha\beta\gamma$-reference frames.

fixed axis $\alpha\beta\gamma$ is done using the Clarke transform defined as in [60]

$$\boldsymbol{x}_{\alpha\beta\gamma} = \mathbf{K}_s \boldsymbol{x}_{abc} \tag{A.0.1}$$

$$\begin{bmatrix} x_\alpha \\ x_\beta \\ x_\gamma \end{bmatrix} = \frac{2}{3} \begin{bmatrix} 1 & -\frac{1}{2} & -\frac{1}{2} \\ 0 & \frac{\sqrt{3}}{2} & -\frac{\sqrt{3}}{2} \\ \frac{1}{2} & \frac{1}{2} & \frac{1}{2} \end{bmatrix} \begin{bmatrix} x_a \\ x_b \\ x_c \end{bmatrix}. \tag{A.0.2}$$

Comparatively, transformation from abc to the rotor fixed axis $dq0$ is done using the $dq0$-transform defined as

$$\boldsymbol{x}_{dq0} = \mathbf{K}_r \boldsymbol{x}_{abc} \tag{A.0.3}$$

$$\begin{bmatrix} x_d \\ x_q \\ x_0 \end{bmatrix} = \frac{2}{3} \begin{bmatrix} \cos(\theta) & \cos(\theta - \frac{2\pi}{3}) & \cos(\theta + \frac{2\pi}{3}) \\ -\sin(\theta) & -\sin(\theta - \frac{2\pi}{3}) & -\sin(\theta + \frac{2\pi}{3}) \\ \frac{1}{2} & \frac{1}{2} & \frac{1}{2} \end{bmatrix} \begin{bmatrix} x_a \\ x_b \\ x_c \end{bmatrix}. \tag{A.0.4}$$

For balanced three-phase quantities it holds true that $x_a + x_b + x_c = 0$ and the 0- and γ-terms of the $dq0$- and $\alpha\beta\gamma$-transforms respectively fall away. This brings to light the simplification of using $dq/\alpha\beta$ reference frames as opposed to the abc phase axis for analysis.

The well known Park transformation defined in [61] is very similar to the $dq0$-transform, but differs in its positioning of the d- and q-axis in relation to the a-phase axis for zero angle θ. The Park transform defines the q-axis to be aligned with the a-phase axis at zero angle, while the $dq0$-transform defines the q-axis to be $\frac{\pi}{2}$ radians in front of the a-phase axis at zero angle.

For direct transformation between the stator fixed and rotor fixed reference frames, the transformation matrix $\mathbf{T}$ is used. It is defined as

$$\mathbf{T} = \begin{bmatrix} \cos\theta_e & -\sin\theta_e \\ \sin\theta_e & \cos\theta_e \end{bmatrix} \tag{A.0.5}$$

$$\begin{aligned} \mathbf{T}^{-1} &= \mathbf{T}^T \\ &= \begin{bmatrix} \cos\theta_e & \sin\theta_e \\ -\sin\theta_e & \cos\theta_e \end{bmatrix}. \end{aligned} \tag{A.0.6}$$

Transformation from rotor fixed to stator fixed ($dq0$ to $\alpha\beta\gamma$) is done using $\mathbf{T}$ and the inverse using $\mathbf{T}^{-1}$ like

$$\boldsymbol{x}_s^s = \mathbf{T}\boldsymbol{x}_s^r \tag{A.0.7}$$

$$\boldsymbol{x}_s^r = \mathbf{T}^{-1}\boldsymbol{x}_s^s. \tag{A.0.8}$$

An orthogonal rotation of a vector in a two axis reference frame is done using $\mathbf{J}$ as

$$\begin{aligned} \mathbf{J} &= \mathbf{T}(\frac{\pi}{2}) \\ &= \begin{bmatrix} 0 & -1 \\ 1 & 0 \end{bmatrix}. \end{aligned} \tag{A.0.9}$$

Appendix B

Space Vector Pulse Width Modulation

Space vector pulse width modulation allows a 15% increase in output voltage amplitude in the linear modulation region compared to conventional PWM [44, 62]. It is based on the eight possible combinations of switching states for a three-phase two-level inverter. These switching states represent eight voltage vectors $\boldsymbol{V}_{0-7}$ listed in Table B.1, where vectors $\boldsymbol{V}_0, 7$ have zero length and $|\boldsymbol{V}_{1-6}| = V_{DC}$. The switch states are shown in Figure B.1 where it is evident that only one set of switches has to change state to go from one switching vector to the next. This results in a very efficient method of sinusoidal voltage supply, since a rotating space vector constitutes this.

The vector representation of the various switching states is shown in Figure B.2. The dotted lines connecting the vectors indicate the maximum vector lengths that can be achieved by a combination of the eight voltage vectors $\boldsymbol{V}_{0-7}$. Subsequently, the dashed circle represents the maximum length of a constant amplitude sinusoidal voltage produced using SVPWM. Using this circle as guideline, we can calculate the maximum amplitude of a sinusoidal SVPWM voltage as

$$\boldsymbol{v}_{max} = |\boldsymbol{V}_{1-6}| \sin(\frac{\pi}{3}) \tag{B.0.1}$$

$$= V_{DC} * \frac{\sqrt{3}}{2} \tag{B.0.2}$$

$$= 0.866 V_{DC}. \tag{B.0.3}$$

With the reference voltages in α/β-reference frame the switching duty cycles are calculated for the most efficient switching pattern. This is done by determining in which sector (between what two vectors) the reference vector is situated. In example, if $v_\beta > 0$ and $0 < v_\alpha < \frac{v_\beta}{\tan(\frac{\pi}{3})}$ the reference voltage vector is in sector I. With this knowledge the duty cycles for the two adjacent switching states are calculated by taking the reference voltage as the vector sum of a combination of the adjacent and zero-state vectors.

Figure B.3 shows how a reference voltage in sector I, $\boldsymbol{v}_s^s$, is constructed using vectors $\boldsymbol{V}_1$ and $\boldsymbol{V}_2$. The quantities can be calculated from the figure as:

$$D_1 V_1 = v_\alpha - \frac{v_\beta}{\tan(\frac{\pi}{3})} \tag{B.0.4}$$

$$D_2 V_2 = \frac{v_\beta}{\sin(\frac{\pi}{3})}. \tag{B.0.5}$$

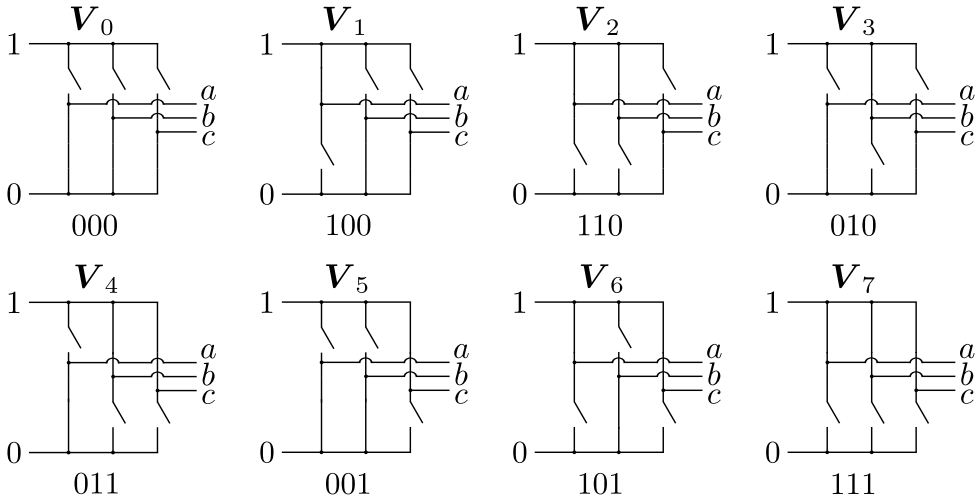

Figure B.1: The voltage vector switching states.

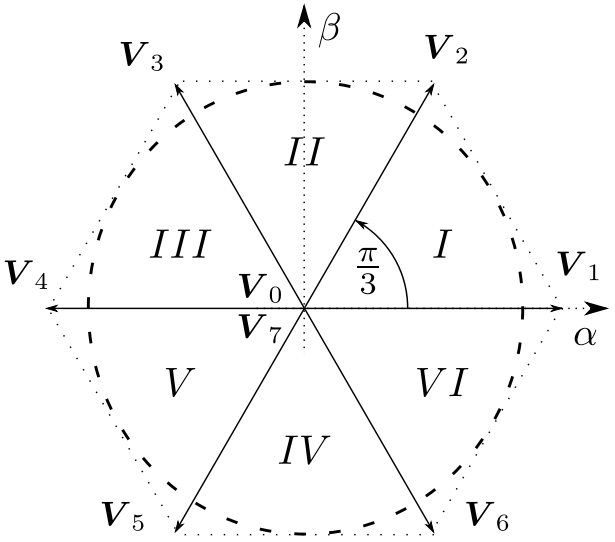

Figure B.2: The vector representation of the various switching states.

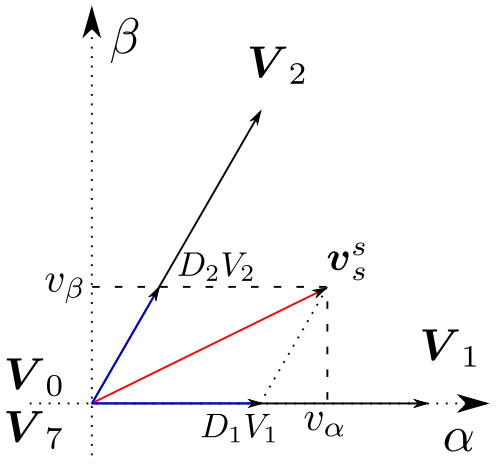

Figure B.3: The duty cycle calculation for sector I.

Since $|\mathbf{V}_{1,2}| = V_{DC}$

$$D_1 = \frac{v_\alpha - \frac{v_\beta}{\tan(\frac{\pi}{3})}}{V_{DC}} \tag{B.0.6}$$

$$D_2 = \frac{v_\beta}{V_{DC}\sin(\frac{\pi}{3})}. \tag{B.0.7}$$

If $D_1 + D_2 > 1$ the values have to be scaled proportionally as

$$D_1^{new} = \frac{D_1}{D_1 + D_2} \tag{B.0.8}$$

$$D_2^{new} = \frac{D_2}{D_1 + D_2}. \tag{B.0.9}$$

Now to calculate the duty cycles, the following equation must hold true

$$D_1 + D_2 + D_0 = 1. \tag{B.0.10}$$

And subsequently the three-phase duty cycles, d_{abc} are calculated

$$d_a = D_1 + D_2 + \frac{D_0}{2} \tag{B.0.11}$$

$$d_b = D_2 + \frac{D_0}{2} \tag{B.0.12}$$

$$d_c = \frac{D_0}{2}. \tag{B.0.13}$$

The duty cycle calculations for the other sectors follow the same steps as described above to result in a complete algorithm that first determines which sector the reference voltage is situated in and then calculates the phase arm duty cycles.

The calculation of duty cycles use quantities such as $\tan(\frac{\pi}{3})$ which are calculated and stored as constants beforehand. This makes the algorithm very computationally efficient.

Table B.1: Space Vector Voltages

Voltage Vector	**Switch states**
$\boldsymbol{V}_0$	000
$\boldsymbol{V}_1$	100
$\boldsymbol{V}_2$	110
$\boldsymbol{V}_3$	010
$\boldsymbol{V}_4$	011
$\boldsymbol{V}_5$	001
$\boldsymbol{V}_6$	101
$\boldsymbol{V}_7$	111

Appendix C

Phase Locked Loop application

A general algorithm for speed and position estimation of AC machines is presented in [14] describing a mathematical derivation for the PLL gains that guarantees stability at constant speed. For a general estimation error in the form of (C.0.1) a PLL scheme such as Figure C.1 can be implemented to drive the speed and position estimates to their true values by taking

$$\varepsilon = K \sin[m(\theta - \hat{\theta})] \tag{C.0.1}$$

as the error signal [14]. θ is the actual rotor position, $\hat{\theta}$ the estimated rotor position, K the application specific gain, and K_I and K_P are the PLL gain parameters. m is dependent on the estimation scheme used where $m = 2$ when the polarity of the rotor cannot be detected - as is the case with saliency based methods - and $m = 1$ otherwise. The block diagram in Figure C.1 is similar to the baseband equivalent model of a PLL where the voltage-controlled oscillator (VCO) corresponds to an integrator and the phase detector (PD) corresponds to (C.0.1) [14].

C.1 Gain Selection

Now, assuming that $\theta \approx \hat{\theta}$, the PLL differential equations from Figure C.1 can be linearised as

$$\dot{\hat{\omega}} = mK.K_I(\theta - \hat{\theta}) \tag{C.1.1}$$

$$\dot{\hat{\theta}} = \hat{\omega} + mK.K_P(\theta - \hat{\theta}) \tag{C.1.2}$$

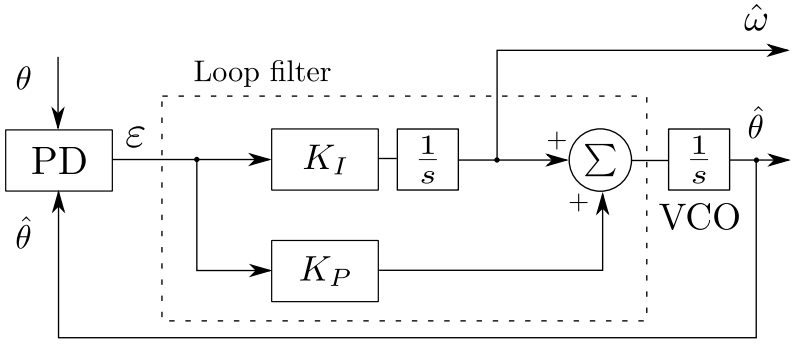

Figure C.1: The PLL observer scheme with error signal input and estimation output.

which have the characteristic polynomial $s^2 + (mK.K_P)s + mK.K_I$ [14]. Therefore the poles of the linearised estimator can be arbitrarily placed by choosing gains K_P and K_I. In [14] it is proposed that the poles both be placed at $s = -\rho$ ($\rho > 0$), since K may not be exactly known and to gain robustness and avoid oscillations. That results in a characteristic polynomial of $s^2 + 2\rho s + \rho^2$ so that the gains should be chosen as [14]

$$K_I = \frac{\rho^2}{mK} \tag{C.1.3}$$

$$K_P = \frac{2\rho}{mK}. \tag{C.1.4}$$

C.2 Pole Placement

In [14] it is derived and shown that for a rampwise change in speed as constant a, $\dot{\omega} = a$, with $mK.K_I = \rho^2$ and $mK.K_P = 2\rho$ the estimation errors $\tilde{\theta} = \theta - \hat{\theta}$ and $\tilde{\omega} = \omega - \hat{\omega}$ can be solved for and the asymptotic ramp tracking errors obtained as

$$\tilde{\theta}^* = \frac{1}{m} \arcsin \frac{a}{\rho^2} \tag{C.2.1}$$

$$\tilde{\omega}^* = \frac{2a}{\rho}. \tag{C.2.2}$$

Evidently, the larger ρ is chosen the smaller the estimation errors become. A rule can be derived from (C.2.1) and (C.2.2) for placing the closed loop poles by assuming the reference speed changes in steps, $\Delta\omega_{ref}$, which results in [14]

$$\rho = \sqrt{\frac{\omega_{BW}\Delta\omega_{ref}}{\sin\tilde{\theta}_{max}}}. \tag{C.2.3}$$

ω_{BW} is the closed loop speed controller bandwidth and $\tilde{\theta}_{max}$ is the maximum allowed speed transient position estimation error. Selecting $\tilde{\theta}_{max}$ as a relatively small value such as 10° should eliminate the estimator being pulled out of phase locking. Therefore the closed loop poles can be placed according to known or designed drive parameters to result in the PLL gains [14].

Noise analysis in [14] shows that for larger values of ρ any white noise components increase more than linearly so that it is vital to not choose ρ larger than necessary and stick to the design equation in (C.2.3).

Appendix D

Simulation Block Diagrams

This appendix contains the simulation block diagrams implemented in Matlab® Simulink®.

Figure D.1 is the anti-integration wind-up block diagram implemented that disables the integrator when the output of the controller is higher than the voltage limit imposed by SVPWM - which is $0.866V_{DC}$. Figure D.2 is the current control loop that implements constant current-angle control on the RSM with speed voltage compensation. The saw-tooth block modulates the angle term to the limits of $0 <= \theta <= 360°$. Figure D.3 is the cascaded PI speed control block diagram that contains the current control loop. The complete AF PSC scheme is given in Figure D.4.

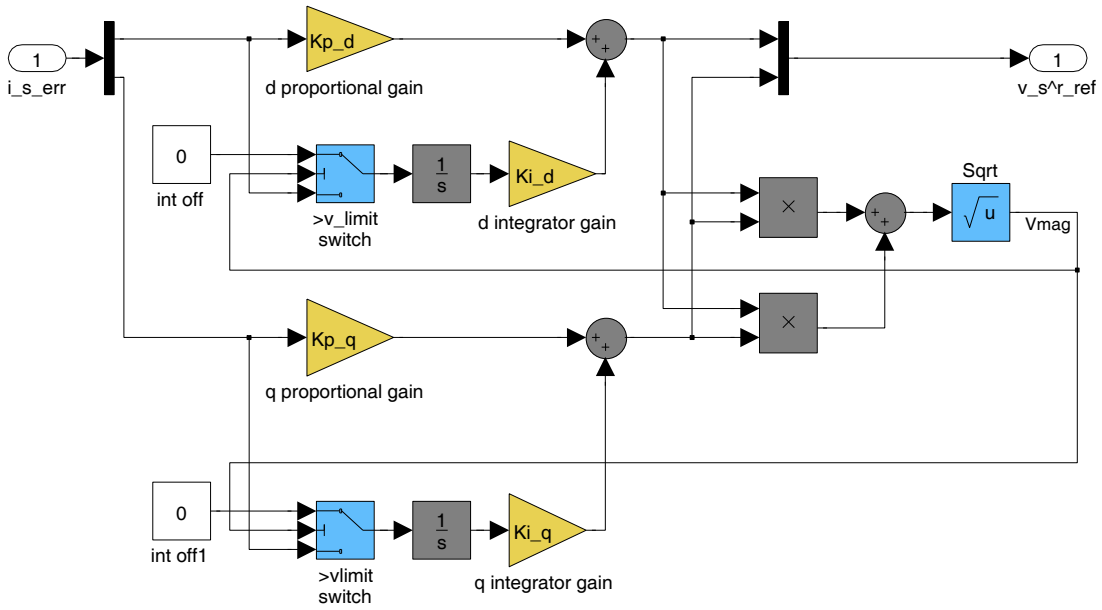

Figure D.1: The simulation block diagram of the PI current controller with anti-integration wind-up.

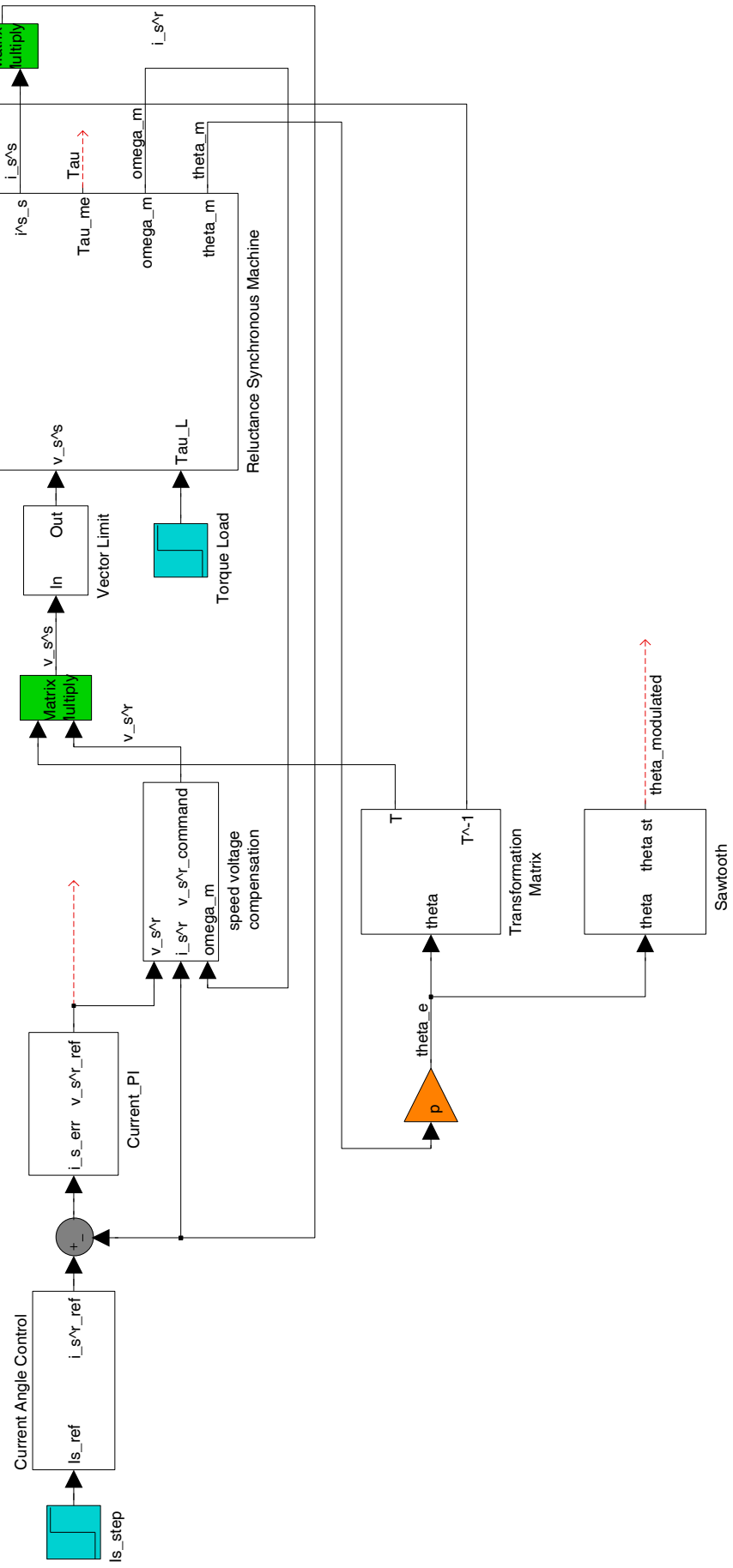

Figure D.2: The closed loop simulation block diagram for current control.

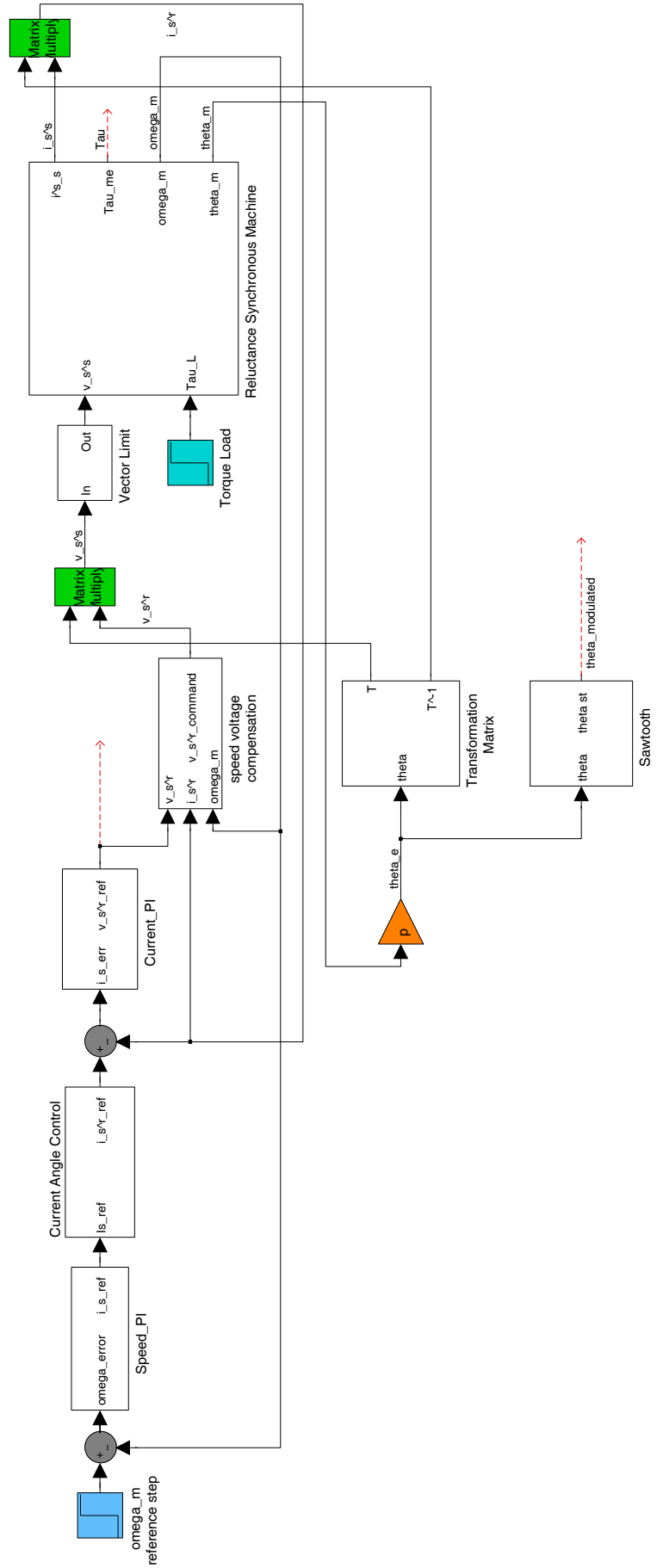

Figure D.3: The closed loop simulation block diagram for speed control.

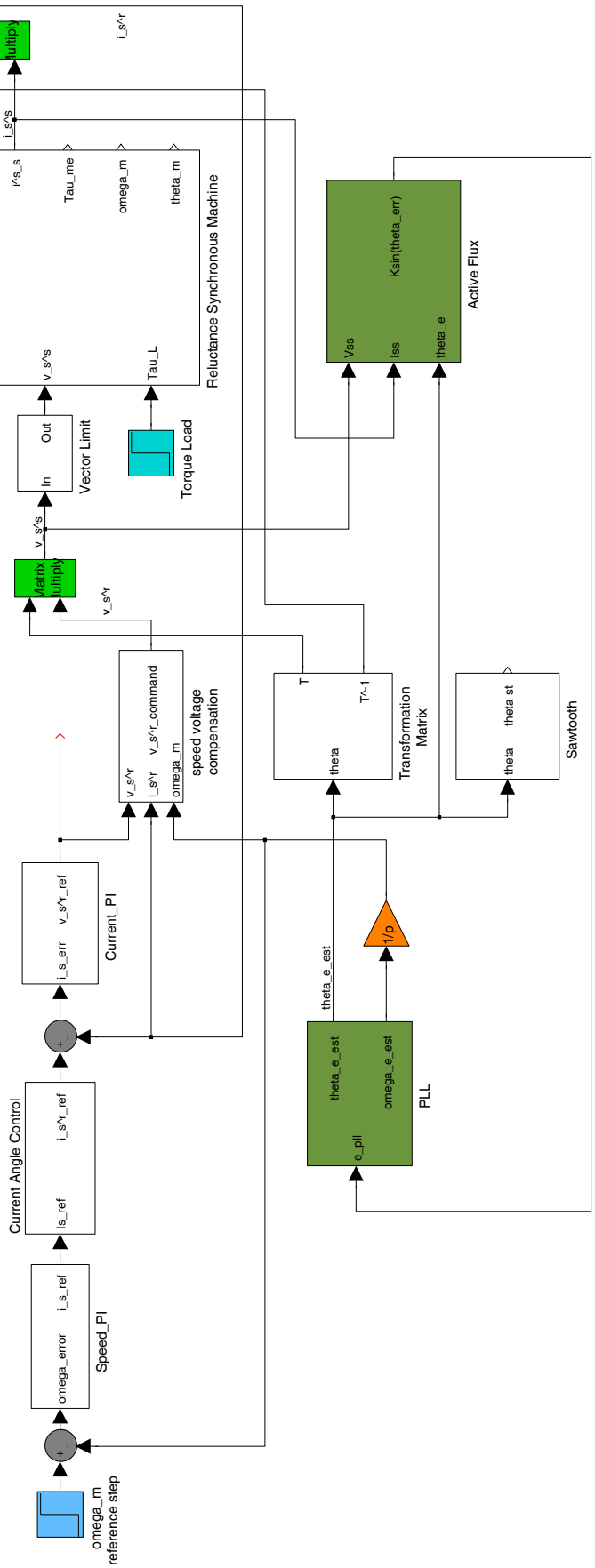

Figure D.4: The closed loop active-flux based position sensorless speed controller simulation block diagram.

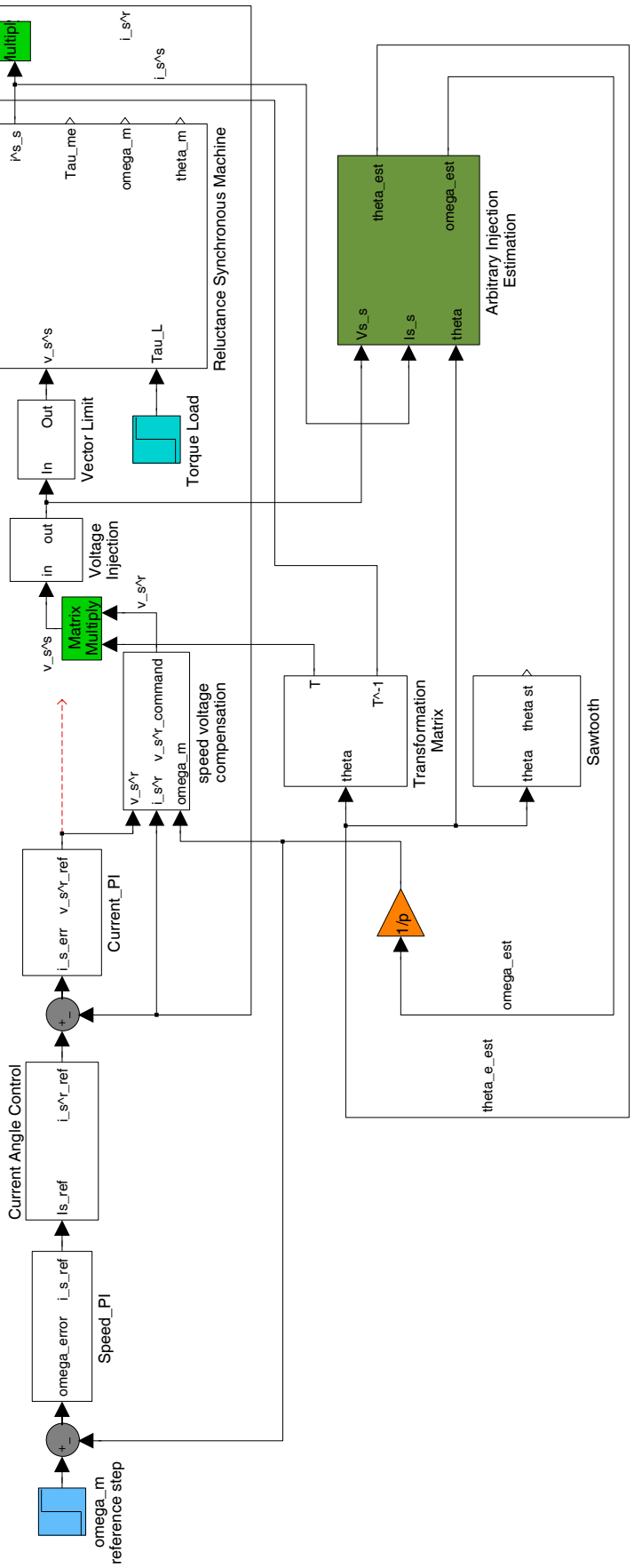

Figure D.5: The closed loop arbitrary injection based position sensorless speed controller simulation block diagram.

Appendix E

Photographs

This appendix contains photographs of the drive system used to validate controllers. It contains the drive test bench, the shaft connected machines used, the back-to-back connected inverters, and some elements of the rapid prototyping system.

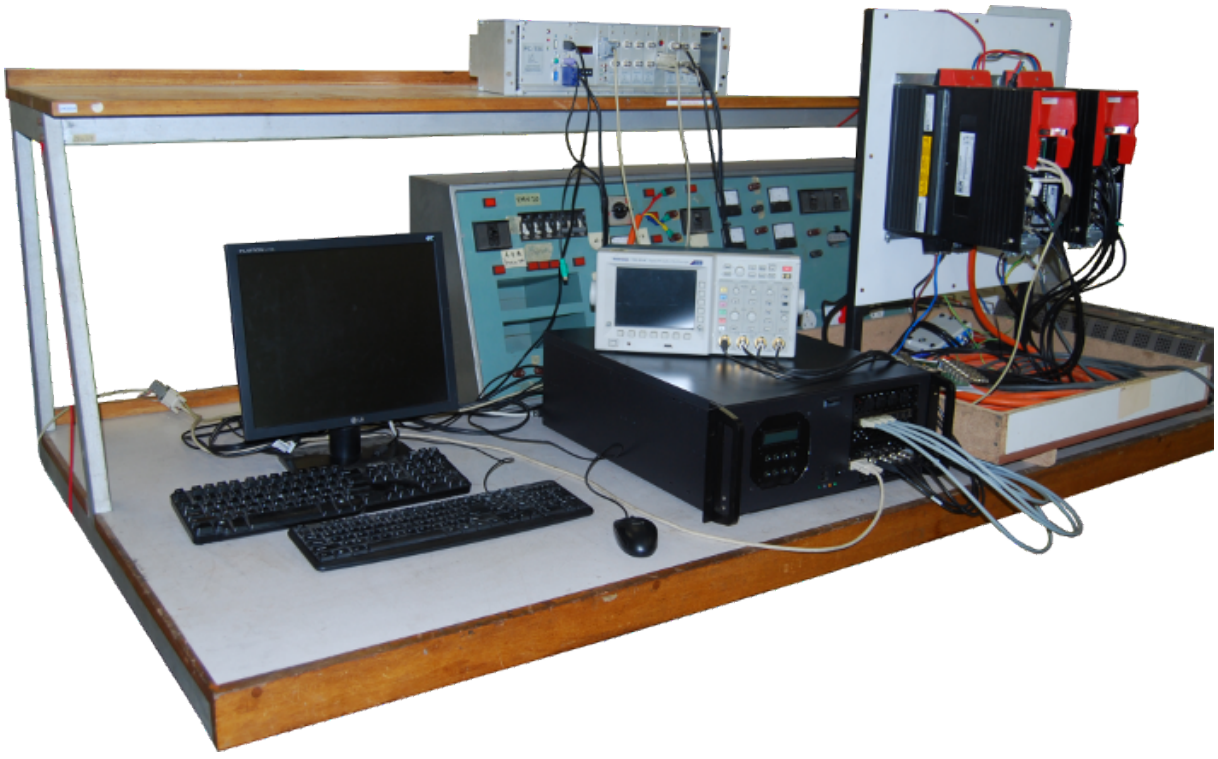

Figure E.1: The drive system test bench used to validate the controllers. The photograph shows the old (top - grey) and new (middle - black) rapid prototyping systems used to control the machines using the two back-to-back connected inverters on the right.

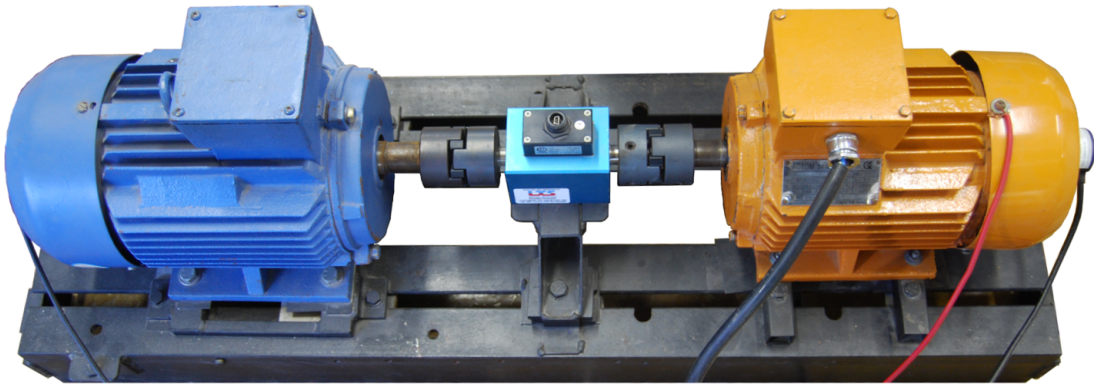

Figure E.2: The shaft connected machines used during practical tests. Blue induction machine on the left and orange RSM on the right.

Figure E.3: The RSM transverse-laminated rotor used for practical testing. Evidently there are no slip-rings (no windings) and the rotor is simply a stack of steel laminations.

Figure E.4: A position resolver connected on the test bench RSM. This is the typical piece of hardware that position sensorless control research aims to mitigate.

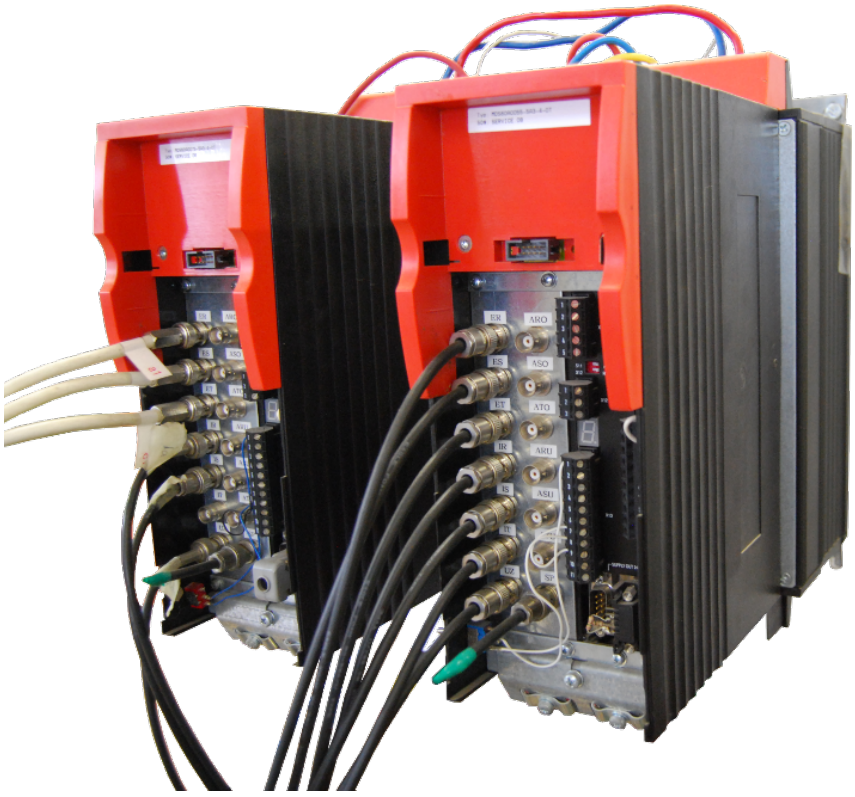

Figure E.5: The DC-link connected voltage source inverters used to apply voltage on the machines. These custom inverters directly receive switching signals and output 3-ϕ current- and DC-bus voltage-measurements.

Figure E.6: The rapid prototyping system front panel showing the 8 A/D-input ports, the 4 D/A-output connectors, the position resolver input port, the 4 state machine control buttons, the 8 hex value control buttons, and the LCD display.

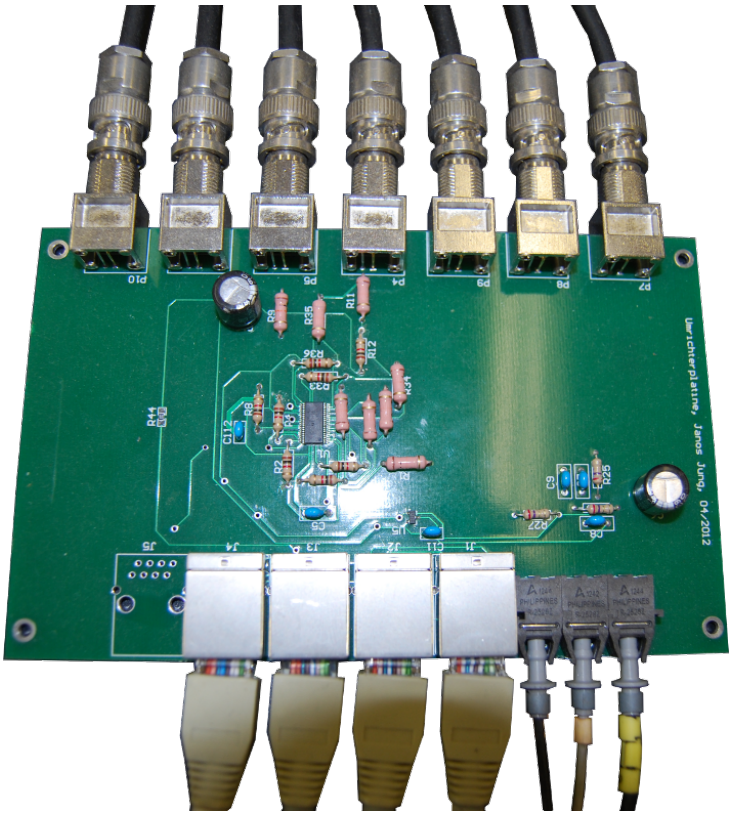

Figure E.7: The inverter board used to convert optical switching signals from the RPS and transmit measurements received from the inverter via RJ45 cables.

Figure E.8: The bar added in order to support the PC motherboard that is mounted on its side (connected to the CPLD-board via an ISA connector).

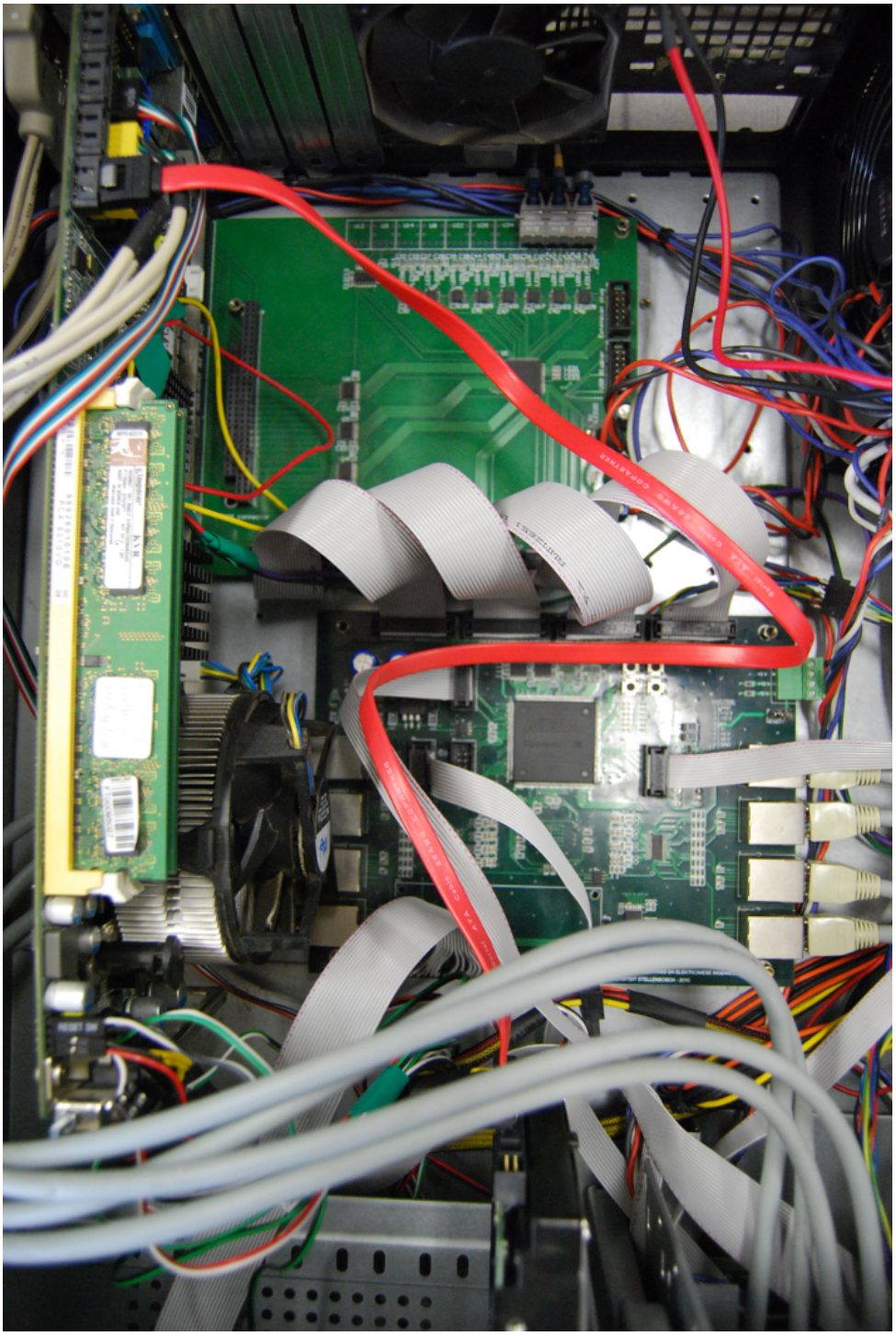

Figure E.9: The RPS board layout showing the PC motherboard on the left, the CPLD board on the top, and the FPGA-board in the middle.

Bibliography

[1] S. Chapman, *Electric Machinery Fundamentals*, ser. McGraw-Hill Series in Electrical and Computer Engineering. McGraw-Hill Companies,Incorporated, 2005.

[2] I. Boldea, *Reluctance Synchronous Machines and Drives*, ser. Monographs in electrical and electronic engineering. Clarendon Press, 1996.

[3] J. Kostko, "Polyphase reaction synchronous motors," *American Institute of Electrical Engineers, Journal of the*, vol. 42, no. 11, pp. 1162–1168, 1923.

[4] A. Vagati, A. Fratta, G. Franceschini, and P. Rosso, "Ac motors for high-performance drives: a design-based comparison," *Industry Applications, IEEE Transactions on*, vol. 32, no. 5, pp. 1211–1219, 1996.

[5] T. A. Lipo, "Synchronous reluctance machines-a viable alternative for ac drives?" *Electric Machines & Power Systems*, vol. 19, no. 6, pp. 659–671, 1991.

[6] A. Vagati, "The synchronous reluctance solution: a new alternative in ac drives," in *Industrial Electronics, Control and Instrumentation, 1994. IECON '94., 20th International Conference on*, vol. 1, 1994, pp. 1–13 vol.1.

[7] A. Boglietti and M. Pastorelli, "Induction and synchronous reluctance motors comparison," in *Industrial Electronics, 2008. IECON 2008. 34th Annual Conference of IEEE*, 2008, pp. 2041–2044.

[8] R. Betz, "Control of synchronous reluctance machines," in *Industry Applications Society Annual Meeting, 1991., Conference Record of the 1991 IEEE*, 1991, pp. 456–462 vol.1.

[9] M. Prins, C. Vorster, and M. Kamper, "Reluctance synchronous and field intensified-pm motors for variable-gear electric vehicle drives," in *Energy Conversion Congress and Exposition (ECCE), 2013 IEEE*, 2013, pp. 657–664.

[10] W. Villet and M. Kamper, "Variable-gear ev reluctance synchronous motor drives - an evaluation of rotor structures for position sensorless control," *Industrial Electronics, IEEE Transactions on*, vol. PP, no. 99, pp. 1–1, 2013.

[11] S. Tokunaga and K. Kesamaru, "Fem simulation of novel small wind turbine generation system with synchronous reluctance generator," in *Electrical Machines and Systems (ICEMS), 2011 International Conference on*, 2011, pp. 1–6.

[12] P. Roshanfekr, S. Lundmark, T. Thiringer, and M. Alatalo, "A synchronous reluctance generator for a wind application-compared with an interior mounted permanent magnet synchronous generator," in *Power Electronics, Machines and Drives (PEMD 2014), 7th IET International Conference on*, April 2014, pp. 1–5.

[13] T. Matsuo and T. Lipo, "Field oriented control of synchronous reluctance machine," in *Power Electronics Specialists Conference, 1993. PESC '93 Record., 24th Annual IEEE*, 1993, pp. 425–431.

[14] L. Harnefors and H.-P. Nee, "A general algorithm for speed and position estimation of ac motors," *Industrial Electronics, IEEE Transactions on*, vol. 47, no. 1, pp. 77–83, 2000.

[15] S. Ichikawa, M. Tomita, S. Doki, and S. Okuma, "Sensorless control of synchronous reluctance motors based on an extended emf model and initial position estimation," in *Industrial Electronics Society, 2003. IECON '03. The 29th Annual Conference of the IEEE*, vol. 3, 2003, pp. 2150–2155 Vol.3.

[16] C.-G. Chen, T.-H. Liu, M.-T. Lin, and C.-A. Tai, "Position control of a sensorless synchronous reluctance motor," *Industrial Electronics, IEEE Transactions on*, vol. 51, no. 1, pp. 15–25, 2004.

[17] T. Kosaka, F. Tanahashi, N. Matsui, and M. Fujitsuna, "Current zero cross detection-based position sensorless control of synchronous reluctance motors," in *Industry Applications Conference, 2002. 37th IAS Annual Meeting. Conference Record of the*, vol. 3, 2002, pp. 1610–1616 vol.3.

[18] M. Hinkkanen, T. Tuovinen, L. Harnefors, and J. Luomi, "A combined position and stator-resistance observer for salient pmsm drives: Design and stability analysis," *Power Electronics, IEEE Transactions on*, vol. 27, no. 2, pp. 601–609, Feb 2012.

[19] I. Boldea and S. Agarlita, "The active flux concept for motion-sensorless unified ac drives: A review," in *Electrical Machines and Power Electronics and 2011 Electromotion Joint Conference (ACEMP), 2011 International Aegean Conference on*, 2011, pp. 1–16.

[20] P. Landsmann, R. Kennel, H. de Kock, and M. Kamper, "Fundamental saliency based encoderless control for reluctance synchronous machines," in *Electrical Machines (ICEM), 2010 XIX International Conference on*, 2010, pp. 1–7.

[21] D. Raca, P. Garcia, D. Reigosa, F. Briz, and R. Lorenz, "A comparative analysis of pulsating vs. rotating vector carrier signal injection-based sensorless control," in *Applied Power Electronics Conference and Exposition, 2008. APEC 2008. Twenty-Third Annual IEEE*, 2008, pp. 879–885.

[22] A. Ravikumar Setty, S. Wekhande, and K. Chatterjee, "Comparison of high frequency signal injection techniques for rotor position estimation at low speed to standstill of pmsm," in *Power Electronics (IICPE), 2012 IEEE 5th India International Conference on*, 2012, pp. 1–6.

[23] D. Paulus, P. Landsmann, and R. Kennel, "Sensorless field- oriented control for permanent magnet synchronous machines with an arbitrary injection scheme and direct angle calculation," in *Sensorless Control for Electrical Drives (SLED), 2011 Symposium on*, 2011, pp. 41–46.

[24] W. Villet, M. Kamper, P. Landsmann, and R. Kennel, "Evaluation of a simplified high frequency injection position sensorless control method for reluctance synchronous machine drives," in *Power Electronics, Machines and Drives (PEMD 2012), 6th IET International Conference on*, 2012, pp. 1–6.

[25] T. Tuovinen, M. Hinkkanen, and J. Luomi, "Analysis and design of a position observer with resistance adaptation for synchronous reluctance motor drives," *Industry Applications, IEEE Transactions on*, vol. 49, no. 1, pp. 66–73, Jan 2013.

[26] P. Landsmann, D. Paulus, P. Stolze, and R. Kennel, "Saliency based encoderless predictive torque control without signal injection for a reluctance synchronous machine," in *Power Electronics and Motion Control Conference (EPE/PEMC), 2010 14th International*, 2010, pp. S1–10–S1–17.

[27] P. Landsmann, C. Hackl, and R. Kennel, "Eliminating all machine parameters in encoderless predictive torque control without signal injection," in *Electric Machines Drives Conference (IEMDC), 2011 IEEE International*, 2011, pp. 1259–1264.

[28] H. Zhu, X. Xiao, and Y. Li, "A simplified high frequency injection method for pmsm sensorless control," in *Power Electronics and Motion Control Conference, 2009. IPEMC '09. IEEE 6th International*, May 2009, pp. 401–405.

[29] C. Silva, G. Asher, and M. Sumner, "Hybrid rotor position observer for wide speed-range sensorless pm motor drives including zero speed," *Industrial Electronics, IEEE Transactions on*, vol. 53, no. 2, pp. 373–378, 2006.

[30] S.-C. Agarlita, I. Boldea, and F. Blaabjerg, "High-frequency-injection-assisted "active-flux"-based sensorless vector control of reluctance synchronous motors, with experiments from zero speed," *Industry Applications, IEEE Transactions on*, vol. 48, no. 6, pp. 1931–1939, 2012.

[31] E. Capecchi, P. Guglielmi, M. Pastorelli, and A. Vagati, "Position-sensorless control of the transverse-laminated synchronous reluctance motor," *Industry Applications, IEEE Transactions on*, vol. 37, no. 6, pp. 1768–1776, 2001.

[32] W. Villet, M. Kamper, P. Landsmann, and R. Kennel, "Hybrid position sensorless vector control of a reluctance synchronous machine through the entire speed range," in *Power Electronics and Motion Control Conference (EPE/PEMC), 2012 15th International*, 2012, pp. LS4b–1.1–1–LS4b–1.1–7.

[33] W. Villet, "Critical evaluation and application of position sensorless control techniques for reluctance synchronous machines," PhD dissertation, Department of Electrical & Electronic Engineering, Stellenbosch, South Africa, 2013.

[34] P. C. Krause, *Analysis of Electric Machinery*, ser. McGraw-Hill Series in Electrical Engineering. McGraw Hill Higher Education, 1986.

[35] H. De Kock, "Position sensorless and optimal torque control of reluctance and permanent magnet synchronous machines," PhD dissertation, Department of Electrical & Electronic Engineering, Stellenbosch, South Africa, 2009.

[36] P. Fick, "Evaluation of the constant current angle reluctance synchronous machine drive," Master's thesis, Department of Electrical & Electronic Engineering, Stellenbosch, South Africa, 2002.

[37] X. Bomela and M. Kamper, "Effect of stator chording and rotor skewing on average torque and torque ripple of reluctance synchronous machine," in *Africon, 1999 IEEE*, vol. 2, 1999, pp. 687–690 vol.2.

[38] R. Trübenbach, "Vector control of a reluctance synchronous machine," Master's thesis, Department of Electrical & Electronic Engineering, Stellenbosch, South Africa, 1993.

[39] P. Vas, *Sensorless vector and direct torque control*, ser. Monographs in electrical and electronic engineering. Oxford University Press, 1998.

[40] K. Rajashekara, A. Kawamura, and K. Matsuse, *Sensorless Control of Ac Motor Drives: Speed and Position Sensorless Operation*, ser. A selected reprint series. IEEE Press, 1996.

[41] A. El-Serafi, X. Liang, and S. Faried, "Factors affecting the accuracy of determining the saturated synchronous machines cross-magnetizing parameters by the finite element method," in *Electrical Machines, 2008. ICEM 2008. 18th International Conference on*, 2008, pp. 1–6.

[42] J. Meriam and L. Kraige, *Engineering Mechanics Dynamics*. John Wiley & Sons, Inc., 2008.

[43] M. Kamper, "Design optimisation of cageless flux barrier rotor reluctance synchronous machines," PhD dissertation, Department of Electrical & Electronic Engineering, Stellenbosch, South Africa, 1996.

[44] H. Van der Broeck, H.-C. Skudelny, and G. Stanke, "Analysis and realization of a pulsewidth modulator based on voltage space vectors," *Industry Applications, IEEE Transactions on*, vol. 24, no. 1, pp. 142–150, 1988.

[45] S.-G. Jeong and M.-H. Park, "The analysis and compensation of dead-time effects in pwm inverters," *Industrial Electronics, IEEE Transactions on*, vol. 38, no. 2, pp. 108–114, Apr 1991.

[46] G. Franklin, G. Franklin, and J. Powell, *Feedback Control of Dynamic Systems: International Version Plus MATLAB and Simulink Student Version 2011a*. Pearson Education, Limited, 2011.

[47] M. Gopal, *Digital Control and State Variable Methods: Conventional and Intelligent Control Systems*. McGraw-Hill Education, 2010.

[48] H. Yamaura and M. Tomizuka, "A new design method for discrete equivalents of analog controllers," in *American Control Conference, 2000. Proceedings of the 2000*, vol. 3, 2000, pp. 1986–1992 vol.3.

[49] P. Guglielmi, M. Pastorelli, and A. Vagati, "Cross-saturation effects in ipm motors and related impact on sensorless control," *Industry Applications, IEEE Transactions on*, vol. 42, no. 6, pp. 1516–1522, Nov 2006.

[50] P. Guglielmi, M. Pastorelli, G. Pellegrino, and A. Vagati, "Position-sensorless control of permanent-magnet-assisted synchronous reluctance motor," *Industry Applications, IEEE Transactions on*, vol. 40, no. 2, pp. 615–622, March 2004.

[51] A. Ejlali, S. Taravat, and J. Soleimani, "Comparative study on control strategy of dtfc based on active flux concept and dtc for ipmsm applied to traction motor," in *Power Electronics, Electrical Drives, Automation and Motion (SPEEDAM), 2012 International Symposium on*, 2012, pp. 200–206.

[52] J. Holtz and J. Quan, "Sensorless vector control of induction motors at very low speed using a nonlinear inverter model and parameter identification," *Industry Applications, IEEE Transactions on*, vol. 38, no. 4, pp. 1087–1095, 2002.

[53] C. Lascu, I. Boldea, and F. Blaabjerg, "A modified direct torque control for induction motor sensorless drive," *Industry Applications, IEEE Transactions on*, vol. 36, no. 1, pp. 122–130, Jan 2000.

[54] D. G. Zill and M. R. Cullen, *Advanced Engineering Mathematics*. Jones and Bartlett Publishers, 2006.

[55] T. Frenzke, "Impacts of cross-saturation on sensorless control of surface permanent magnet synchronous motors," in *Power Electronics and Applications, 2005 European Conference on*, 2005, pp. 10 pp.–P.10.

[56] M. Kamper and A. Volsdhenk, "Effect of rotor dimensions and cross magnetisation on ld and lq inductances of reluctance synchronous machine with cageless flux barrier rotor," *Electric Power Applications, IEE Proceedings* -, vol. 141, no. 4, pp. 213–220, Jul 1994.

[57] F. J. Barnard, W. T. Villet, and M. J. Kamper, "Hybrid active-flux and arbitrary injection position sensorless control of reluctance synchronous machines," in *Power Electronics, Electrical Drives, Automation and Motion (SPEEDAM), 2014 International Symposium on*, June 2014, pp. 1146–1151.

[58] A. Piippo, M. Hinkkanen, and J. Luomi, "Sensorless control of pmsm drives using a combination of voltage model and hf signal injection," in *Industry Applications Conference, 2004. 39th IAS Annual Meeting. Conference Record of the 2004 IEEE*, vol. 2, Oct 2004, pp. 964–970 vol.2.

[59] A. Piippo and J. Luomi, "Adaptive observer combined with hf signal injection for sensorless control of pmsm drives," in *Electric Machines and Drives, 2005 IEEE International Conference on*, May 2005, pp. 674–681.

[60] E. Clarke, *Circuit Analysis of A-C Power Systems...*, ser. General Electric series. Wiley, 1950.

[61] R. Park, "Two-reaction theory of synchronous machines generalized method of analysis-part i," *American Institute of Electrical Engineers, Transactions of the*, vol. 48, no. 3, pp. 716–727, July 1929.

[62] J.-H. Youm and B.-H. Kwon, "An effective software implementation of the space-vector modulation," *Industrial Electronics, IEEE Transactions on*, vol. 46, no. 4, pp. 866–868, Aug 1999.